

School of Mechanical, Materials and Manufacturing Engineering



The University of  
**Nottingham**

LASER PROCESS OPTIMISATION FOR IN-SITU REPAIR OF  
AERO-ENGINE COMPONENTS

By

David Jonathan Gilbert

Thesis submitted to the University of Nottingham for the degree of

Doctor of Engineering (EngD), February 2017

# Table of Contents

<b>CHAPTER 1. PROJECT INTRODUCTION</b>	<b>1</b>
1.1 COMPONENT OPERATION AND IN-SERVICE DAMAGE	1
1.2 DAMAGE DETECTION AND INSPECTION	1
1.3 REPAIR AND OVERHAUL IMPLICATIONS, LIMITATIONS AND COSTS	1
1.3.1 <i>Costs of grounded aircraft</i>	2
1.3.2 <i>Delivering tooling and technical capability to the engine</i>	2
1.4 IN-SITU COMPONENT REPAIR	2
1.4.1 <i>Mechanical boreblending</i>	3
1.4.2 <i>Laser boreblending</i>	4
1.5 PROJECT OBJECTIVES	4
1.6 THESIS STRUCTURE	6
1.7 HIGHLIGHTS OF SCIENTIFIC CONTRIBUTIONS FROM THESIS CHAPTERS	8
<b>CHAPTER 2. LITERATURE REVIEW</b>	<b>9</b>
2.1 NICKEL USAGE IN AEROSPACE ENGINES	9
2.1.1 <i>Nickel alloy Metallurgy</i>	9
2.2 FATIGUE AND FAILURE MODES OF COMPRESSOR COMPONENTS	11
2.2.1 <i>Common damage and failure modes of Ni-Alloy components</i>	11
2.3 COMPONENT REPAIR	12
2.3.1 <i>Background to laser operation</i>	12
2.3.2 <i>Laser beam characteristics</i>	13
2.3.3 <i>Laser pulsing</i>	15
2.3.3.1 Pulsed Pumping	16
2.3.3.2 Q-Switching	16
2.3.3.3 Mode-Locking	16
2.3.4 <i>Directing Laser Energy</i>	17
2.4 LASER MACHINING OF NICKEL SUPERALLOYS	17
2.4.1 <i>Laser-alloy interaction</i>	17
2.4.2 <i>Modes of material removal</i>	18
2.4.3 <i>Secondary Effects of laser machining</i>	20
2.4.3.1 Residual Stresses	20
2.4.3.2 Material recast Layer	20
2.4.3.3 Micro-cracking surface and internal cracks	21
2.4.3.4 Surface Roughness	22
2.4.3.5 Material oxidation	22
2.4.3.6 Heat affected zone	22
2.4.4 <i>Modelling of laser machining</i>	23

2.5	NICKEL ALLOY INSPECTION AND ANALYSIS	25
2.5.1	<i>Nickel sample preparation</i>	25
2.5.2	<i>Scanning Electron Microscope Analysis</i>	26
2.5.3	<i>X-Ray Diffraction (XRD) measurements</i>	26
2.5.3.1	Bragg's Law	27
2.5.3.2	Residual Stresses	27
<b>CHAPTER 3.</b>	<b>EXPERIMENTAL METHODOLOGY AND EQUIPMENT</b>	<b>29</b>
3.1	PULSE LASER ABLATION (PLA)	29
3.2	SAMPLE CUTTING, MOUNTING, POLISHING AND ETCHING	30
3.2.1	<i>Sample Cutting</i>	30
3.2.2	<i>Resin Mounting</i>	30
3.2.3	<i>Abrasive Polishing</i>	31
3.2.4	<i>Chemical Etching</i>	31
3.3	TOPOGRAPHICAL SURFACE MEASUREMENT	31
3.4	SCANNING ELECTRON MICROSCOPY	32
<b>CHAPTER 4.</b>	<b>METALLURGICAL CHANGES IN LASER MACHINED INCONEL® 718</b>	<b>33</b>
4.1	METALLURGICAL REQUIREMENTS FROM ROLLS-ROYCE	33
4.1.1	<i>Chemical and microstructural analysis techniques</i>	33
4.2	METHODOLOGY FOR ASSESSING METALLURGICAL IMPACT OF LASER MACHINING	33
4.2.1	<i>Sample Preparation for machining and inspection</i>	33
4.2.1.1	Laser Ablation sample preparation	34
4.2.2	<i>Measurement of samples using XRD (X-Ray Diffraction) for residual stresses and chemical constituents</i>	36
4.2.2.1	Residual Stress Measurement	36
4.2.2.2	Material Phase Analysis	38
4.2.3	<i>Surface Roughness Evaluation</i>	38
4.2.4	<i>Scanning Electron Microscopy (SEM) Analysis</i>	39
4.2.4.1	Microstructural Analysis using SEM	39
4.2.4.2	Chemical Analysis using SEM	39
4.3	RESULTS AND DISCUSSION	40
4.3.1	<i>Results for Surface Roughness Evaluation</i>	40
4.3.1.1	Residual Stress Measurement	42
4.3.1.2	Chemical Analysis of XRD data	46
4.3.2	<i>SEM measurement results</i>	48
4.3.2.1	Qualitative Analysis	48
4.3.2.2	Recast thicknesses	50
4.3.3	<i>Statistical Analysis of impact of KPV values on metallurgical changes</i>	55
4.3.3.1	Statistical main effects	56

4.3.3.2	Key process variable significance	57
4.4	OBSERVATIONS FROM SAMPLE ANALYSIS	57
4.5	SUMMARY	58
<b>CHAPTER 5. LASER BEAM – WORK PIECE INTERACTION AT MICRO-GEOMETRICAL LEVEL</b>		<b>59</b>
5.1	INTRODUCTION TO MATHEMATICAL MODELLING APPROACH	60
5.1.1	<i>Scope of the mathematical model</i>	60
5.1.2	<i>Approach in modelling of surface roughness in PLA</i>	60
5.1.3	<i>Geometrical modelling of pulsed laser ablated surfaces</i>	62
5.1.4	<i>Generic relationship between laser fluence and depth of ablation</i>	62
5.1.4.1	Fluence definition and calculation when considering a freeform target surface	64
5.1.4.2	Kinematics of the beam	64
5.1.5	<i>Time modulation of laser input signal</i>	65
5.1.6	<i>Instantaneous spatial energy distribution of the beam</i>	66
5.1.7	<i>Laser divergence and depth of field</i>	67
5.1.8	<i>Variability in irradiated surface area per pulse</i>	68
5.2	COMPOUNDED MATERIAL REMOVAL FUNCTION	68
5.2.1	<i>Surface prediction in the presence of material redeposition</i>	70
5.3	METHODOLOGY AND EXPERIMENTAL DESIGN FOR MODEL CALIBRATION AND VALIDATION	71
5.4	MATHEMATICAL MODEL VALIDATION AND DISCUSSION ON NS AND PS LASER SYSTEMS	76
5.4.1	<i>Experimental data for calibration of material response</i>	76
5.4.1.1	Material response equation	76
5.4.1.2	Experimental characterisation of material redeposition	77
5.4.1.3	Selection of craters and tracks for model validation for 200 nanosecond pulses	78
5.5	MATLAB GUI FOR SIMULATION OF SURFACE TEXTURE UNDER PLA	80
5.6	OPTIMISED PARAMETERS SELECTION	82
5.7	SUMMARY	83
<b>CHAPTER 6. MICRO AND MACRO SCALE VALIDATION FOR MATHEMATICAL MODELLING</b>		<b>85</b>
6.1	VALIDATION OF MATHEMATICAL MODEL	85
6.2	VALIDATION REQUIREMENTS FOR CHAPTER 5 MODEL	86
6.3	METHODOLOGY FOR MICRO-SCALE FEATURE VALIDATION ON CVD DIAMOND TARGETS	87
6.3.1	<i>Ablation Trial 1 - Mathematical Model Calibration</i>	87
6.3.2	<i>Ablation Trials 2 &amp; 3 – Mathematical Model Validation</i>	88
6.3.3	<i>Measurement of ablated samples</i>	89
6.3.4	<i>Data import and handling</i>	89
a)	Experimental / Simulation data Import	89
b)	Experimental data graphs	90
c)	Simulated data graphs	93
d)	Validation of simulated surface data against measured surface data	93

6.4	METHODOLOGY FOR MACRO-SCALE FEATURE VALIDATION ON INCONEL® 718 TARGETS	96
6.5	RESULTS AND DISCUSSION	99
6.5.1	<i>Results from micro-scale picosecond ablation of CVD Diamond targets</i>	99
6.5.2	<i>Results from macro-scale nanosecond ablation of INCONEL® 718 targets</i>	101
6.5.3	<i>Observations from results on Picosecond – CVD Diamond target ablation</i>	101
6.5.4	<i>Observations from results on Nanosecond – INCONEL® 718 target ablation</i>	103
6.6	SUMMARY	103
<b>CHAPTER 7. BLEND GENERATION AND HIGH CYCLE FATIGUE TESTING</b>		<b>104</b>
7.1	INTRODUCTION	104
7.2	BLENDING PROCESSES AND THEIR IMPLICATIONS	104
7.2.1	<i>Mechanical Boreblending</i>	105
7.2.2	<i>Laser Boreblending</i>	105
7.3	REPAIR LOCATION AND GEOMETRY	105
7.4	OPTICAL HEAD CONSIDERATIONS	106
7.5	SCAN PATH ADAPTATION FROM LABORATORY TO OPTICAL MINIATURE HEAD LASER.	109
7.6	METHODOLOGY	111
7.6.1	<i>Blend Generation</i>	111
7.6.2	<i>Mechanical Boreblending</i>	112
7.6.3	<i>Laser Boreblending</i>	113
7.6.4	<i>High Cycle Fatigue testing</i>	115
7.6.5	<i>Fracture surface inspection</i>	117
7.7	RESULTS	118
7.7.1	<i>High Cycle Fatigue Results</i>	118
7.7.2	<i>Fracture surface inspection</i>	123
7.8	DISCUSSION	125
7.8.1	<i>First set of HCF tests</i>	125
7.8.2	<i>Second set of HCF tests</i>	126
7.9	FRACTURE MECHANICS	126
7.10	SUMMARY OF HCF TESTING ON REPAIRED COMPONENTS	127
<b>CHAPTER 8. SAMPLE BLENDING WITH IN-SITU PROTOTYPE EQUIPMENT</b>		<b>128</b>
8.1	INTRODUCTION	128
8.2	SPATIAL RESTRICTIONS ON REPAIR EQUIPMENT	128
8.3	REPAIR GEOMETRY	129
8.4	SIDE EFFECTS OF REPAIR	129
8.5	METHODOLOGY	130
8.5.1	<i>Component Alignment</i>	130
8.5.2	<i>Scan path generation</i>	131

8.5.3	<i>Bulk material removal</i>	131
8.5.4	<i>Blend surface polishing</i>	132
8.5.5	<i>Capture of ejected materials</i>	132
8.6	RESULTS	133
8.6.1	<i>Repair quality, performance and repeatability</i>	133
8.6.2	<i>Analysis of ejected materials</i>	134
8.7	DISCUSSION	137
8.7.1	<i>Blend Surface Quality</i>	137
8.7.2	<i>Ejected materials</i>	138
<b>CHAPTER 9.</b>	<b>OVERALL DISCUSSION</b>	<b>139</b>
9.1	DISCUSSION OF PROJECT OBJECTIVES	139
9.1.1	<i>Achieving material removal with the proposed laser system</i>	139
9.1.2	<i>Minimise material damage caused by laser machining</i>	139
9.1.3	<i>Mathematical modelling of ablated features and surfaces</i>	140
9.1.4	<i>Maximising material removal rate for repair geometries</i>	141
9.1.5	<i>Mathematical model validation on diamond and nickel targets</i>	141
9.1.6	<i>Quantify repair-induced fatigue changes</i>	142
9.1.7	<i>Operation and failure mode investigation of OpTek optical head</i>	142
9.2	FUTURE RECOMMENDATIONS	143
9.2.1	<i>Laser system options for reduced material recast</i>	143
9.2.2	<i>Mathematical modelling improvements for material recast characterisation</i>	144
9.2.3	<i>Reducing loss of fracture surface detail during testing and preparation for analysis</i>	144
9.2.4	<i>Increasing the range of data available from high cycle fatigue testing</i>	145
9.2.5	<i>Improving inspection and analysis methods for high cycle fatigue specimens</i>	145
<b>CHAPTER 10.</b>	<b>CONCLUSIONS</b>	<b>146</b>
	<b>REFERENCES</b>	<b>148</b>

## Abstract

Repairs on stress raising features (SRFs) generated on internal aero engine components such as compressor blades are sometimes necessary, dependent on size, to avoid further damage, such as crack propagation. Where possible, repairs are carried out whilst the engine remains on the wing (in-situ) to avoid costs incurred by engine removal/transportation, and fines from non-operation of the engine. A system comprising an SPI pulsed laser, a Surgical Innovations deployment probe, and OpTek beam guidance components, proposes to adapt the current method of SRF blending which uses a rigid grinding tool, inserted into the engine through the external inspection ports. The need for this update to the system arises from components in the new Trent XWB engine which are not compatible with the previous rigid grinding tool. Delivery is planned through a deployment probe with a set of laser beam guidance optics at the head.

Material removal was achieved using a nanosecond ( $1 \leq \tau \leq 999 \times 10^{-9}$ s) pulsed Yb:YAG infra-red (1064nm) laser, which was used to ablate material in multiple small volumes (craters). Metallurgical studies were conducted to quantify the effect of the three key process variables (laser power, pulse frequency, scan speed) on secondary effects such as material recast layer thickness and oxidation. Through these experiments some optimal machining parameters were defined, which could produce repair geometries with a good compromise between minimising machining time and reducing component metallurgical damage. These parameters were defined as 13W of measured power output (input and output powers may vary dependent upon a number of atmospheric conditions such as ambient temperature and air pressure), 25-35kHz pulse frequency (dependant on laser system attenuation frequencies), and 400-500mm/s scan speed. Using these parameters repairs were generated with full ablation through the blade edge in 15 minutes.

A predictive model was made to simulate surface topography evolution throughout a laser ablation process with any given parameters, using some initial laser-material calibration experimentation. This model showed good predictive powers, where initial validation of the model showed errors under 9.39% for ablation on CVD diamond and under 1.3% for ablation in INCONEL<sup>®</sup> 718 alloy. The model had limited predictive capability for simulating material redeposition and as such further validation was carried out for more complex geometries. Micro-scale validation was carried out on diamond for complex features generated using varied laser scan track overlaps. Macro-scale validation was carried out on INCONEL<sup>®</sup> 718 for large features where a desired mass was to be removed through prediction of volume of

machined material using the model. Both further validation experiments had errors as low as -0.14% and 1.38% for diamond and INCONEL<sup>®</sup> 718 targets respectively.

High cycle fatigue testing was carried out on engine run compressor components from an XWB test engine. These components were machined using best-practice boreblending techniques employed in the field today, as well as laser machining developed throughout this project. Optimised machining parameters as discussed previously were used to generate laser repairs with minimal material damage. These laser repairs were performed using both laboratory laser equipment, and prototypes for tooling which is intended for use on in-situ repairs in the field. All of these machined samples were put under high cycle fatigue testing to simulate component fatigue life changes induced from each machining method, whilst all repair methods presented fatigue strengths that would surpass the fatigue performance of components which had sustained foreign object damage and had not been repaired. Repair geometries and locations were determined through finite element analysis performed by Rolls-Royce Compressor Stress teams, where a worst-case scenario for component loading could be simulated with these repairs. Each of the repair types demonstrated fatigue life above the minimum required as defined by Rolls-Royce for project advancement. Material microstructure remains largely unchanged when laser processing is used, when compared to mechanically repaired components. The only easily observable change is material recast, and this falls within acceptable limits as defined in Rolls-Royce laser machining standards in every case [1]. Fracture surface inspection confirms results seen in the metallurgical study. Average fatigue strength after  $10^7$  cycles was calculated for components repaired with each method, showing similar performance between laser and mechanical blending.

As the prototype tooling was in continuous development, the approach angle of the tool against the blade and hence the repair geometry changed, and as such repeated tests were carried out to validate fatigue performance on different repair geometries.

A number of figures and technical details have been redacted from this version of the project thesis to protect the intellectual property and commercial interests of Rolls-Royce PLC.

## Acknowledgements

I would like to thank my academic supervisor Professor Dragos Axinte for his invaluable advice and input into the four years of work involved in my EngD. From the project planning stages, right through to the completion of this thesis, his experience and insight has contributed greatly to the successful completion of project objectives. I am grateful for his generosity with his time, be it spending many hours with me discussing project direction and solving problems, or taking time out of his evenings and weekends to read through my work and give his feedback.

I would like to acknowledge the input from everyone involved in the project from both technical and industrial sides. I would like to thank the On-Wing-Care team at Rolls Royce, especially Dr. James Kell as my primary industrial supervisor for his willingness to take time out of his schedule to assist with my understanding of the industrial and business backgrounds and requirements of my work. Dr. Andy Norton has also been a great help throughout the latter stages of my project in both a practical capacity, giving assistance in the laboratory, and in a project managerial role by helping me prioritise and organise project tasks.

I would like to thank technical staff at the University of Nottingham, OpTek Systems and Rolls-Royce. With their guidance and expertise I was better able to carry out experimental tasks within my project, and confidently present the results with a stronger understanding of the technical processes involved.

Lastly, I would like to thank my friends, family and my girlfriend for their unwavering support and encouragement throughout the last 4 years. From providing welcome distractions such as games evenings and weekend trips, to taking a real interest in the work I have been doing by lending an ear for me to discuss project ideas and problems.

Without the help of the people mentioned above, this project would have been much harder, if not impossible to complete and for that I am extremely grateful. They have all made the last 4 years much easier and more enjoyable and for this they are acknowledged.

## Publications

The research in this thesis has contributed in part or full for the following publications:

D. Gilbert, M. Stoesslein, D. Axinte, P. Butler-Smith, and J. Kell, "A time based method for predicting the workpiece surface micro-topography under pulsed laser ablation," *J. Mater. Process. Technol.*, vol. 214, no. 12, pp. 3077–3088, 2014.

M. Stoesslein, D. Axinte, and D. Gilbert, "On-The-Fly Laser Machining: A Case Study for In Situ Balancing of Rotative Parts," *J. Manuf. Sci. Eng.*, vol. 139, no. 3, p. 31002, Oct. 2016.

## Nomenclature

<b>Symbol</b>	<b>Definition</b>	<b>Unit</b>
<b><math>f_0</math></b>	Attenuating pulse repetition frequency	Hz
<b>P</b>	Average beam power	W
<b><math>\varphi_0</math></b>	Beam diameter at focus	$\mu\text{m}$
<b><math>\varphi_z</math></b>	Beam diameter at height z	$\mu\text{m}$
<b><math>\theta</math></b>	Beam path scan angle	$^\circ$
<b><math>M^2</math></b>	Beam quality factor	
<b><math>v_f</math></b>	Beam scan speed	mm/s
<b>A</b>	Beam spot area	$\mu\text{m}^2$
<b>z</b>	Focal offset height	$\mu\text{m}$
<b><math>S_1</math></b>	Isotropic X-Ray Elastic Constant	$\text{TPa}^{-1}$
<b><math>\frac{1}{2}S_2</math></b>	Isotropic X-Ray Elastic Constant	$\text{TPa}^{-1}$
<b><math>\lambda</math></b>	Laser beam wavelength	$\mu\text{m}$
<b><math>\tau</math></b>	Laser pulse duration	ns
<b><math>E_{\text{pulse}}</math></b>	Laser pulse energy	J
<b><math>D_{x,y}</math></b>	Machined geometry dimensions	mm
<b><math>P_{\text{max}}</math></b>	Maximum average beam power	W
<b><math>\Phi_{\text{max}}</math></b>	Maximum fluence	$\text{J}/\text{cm}^2$
<b>I</b>	Normalised beam intensity	%
<b><math>\sigma</math></b>	Normal stress	MPa
<b><math>n_z</math></b>	Number of laser scan passes (layers)	
<b><math>\sigma_{\text{ac}}</math></b>	Peak modal alternating stress	MPa/mHz
<b><math>\nu</math></b>	Poisson's Ratio	
<b><math>d_{x,y}</math></b>	Pulse offset	$\mu\text{m}$
<b>f</b>	Pulse repetition frequency	Hz
<b><math>z_R</math></b>	Raleigh length	$\mu\text{m}$
<b><math>\Phi_0</math></b>	Reference fluence	$\text{J}/\text{cm}^2$
<b>c</b>	Rim radius	$\mu\text{m}$
<b>n</b>	Rim shaping factor	
<b><math>\omega</math></b>	Rotational speed	RPM
<b>K</b>	Shear Stress	MPa
<b>h</b>	Surface height	$\mu\text{m}$
<b>Ra</b>	Surface roughness	$\mu\text{m}$
<b>t</b>	Time	s
<b><math>\delta_{\text{track}}</math></b>	Track offset	$\mu\text{m}$
<b>E</b>	Young's Modulus	
<b>AF</b>	$10^7$ cycle fatigue failure strength	mHz

## Acronyms

<b>Acronym</b>	<b>Definition</b>
<b>BSE</b>	Back-scattered Electron
<b>CVD</b>	Chemical Vapour Deposition
<b>CAM</b>	Computer Aided Manufacture
<b>DOE</b>	Design of Experiments
<b>EDX</b>	Energy Dispersive X-Ray
<b>FEG</b>	Field Emission Gun
<b>FEA</b>	Finite Element Analysis
<b>FEM</b>	Finite Element Modelling
<b>GUI</b>	Graphical User Interface
<b>HAZ</b>	Heat Affected Zone
<b>HCF</b>	High Cycle Fatigue
<b>HPC</b>	High Pressure Compressor
<b>IN718</b>	INCONEL® 718
<b>KPV</b>	Key Process Variable
<b>MCF</b>	Material Confidence Factor
<b>N105</b>	NIMONIC® 105
<b>PLA</b>	Pulsed Laser Ablation
<b>RR</b>	Rolls-Royce
<b>SEM</b>	Scanning Electron Microscope
<b>SE</b>	Secondary Electron
<b>SRF</b>	Stress Raising Feature
<b>TEM</b>	Transverse Electromagnetic Mode
<b>XRD</b>	X-Ray Diffraction
<b>Yb:YAG</b>	Ytterbium doped Yttrium Aluminium Garnet

# Chapter 1. Project Introduction

## 1.1 Component operation and in-service damage

Components within turbofan engines used in civil aerospace applications undergo a range of demanding operating conditions and stress cycles. High temperatures, pressures and both high and low cyclical loading stresses lead to strict geometry design and material selection requirements to maximise component life. Any damage caused to the component, either geometric (physical deformation or tearing) or metallurgical (changes in material properties due to chemical corrosion or thermal degradation) can greatly reduce component life.

High gas velocities within the engine compressor modules leads to very high impact forces on components from foreign objects ingested through the engine fan. These foreign objects are most commonly dust or ice particles present in the surrounding atmosphere, or larger particles from less frequent events such as bird strikes. As these objects strike engine components, they may dent, tear or crack them creating stress concentrating features within load bearing parts of the component. This in turn will create localised areas of exaggerated stress within the component, and if these highly stressed areas are structurally critical the component may fail.

## 1.2 Damage detection and inspection

Aircraft engines must undergo routine inspection to check for damage accumulated in service [2], [3]. As some of the components which undergo the most demanding operation are within the engine core, accessing these components for inspection can be difficult. Without almost completely disassembling the engine, these components are hard to access and view to properly assess for damage. As such, inspection ports are placed radially around the engine at various stages along the gas stream to allow external access to the engine core [3]. Through these inspection ports, endoscopic equipment can be used to examine component surfaces for damage. Visual inspection can be used to identify damage.

## 1.3 Repair and overhaul implications, limitations and costs

When damage components are detected, dependent on the extent and location of the damage, they must be repaired, or replaced either immediately or at the next planned engine service. In the case where a component must be repaired, it must be done so in the most time and cost-efficient manner.

### 1.3.1 Costs of grounded aircraft

Power provision is a large and growing part of the Rolls-Royce business model. Customers will buy “power” provided by Rolls-Royce, rather than simply purchasing an engine and that being the extent of the interaction. The engine is then maintained and monitored by Rolls-Royce as part of their TotalCare® service.

### 1.3.2 Delivering tooling and technical capability to the engine

The Repair Technology Team within Engineering and Technology at Rolls-Royce have developed methods and technologies to repair damaged components whilst the engine remains on the aircraft wing (In-Situ). These repair tools require skilled operators, and as such they must be flown out to grounded aircraft to carry out these repairs wherever they may be around the world. In certain engines there may be areas and components which are inaccessible with previously established repair technologies, and as such research and development is necessary to continually improve the repair and servicing capabilities for these engines.

## 1.4 In-Situ component repair

Repairs performed on components in-situ must follow strict guidelines as described in the engine manual written by Rolls-Royce. These describe repair geometries (both size and shape) and location, and are held in Repair Scheme FRSB551. Certain zones of components are too structurally important to allow repairs and components with damage in these zones must be immediately replaced. Damage in other zones is repairable up to certain geometric limits dependent on the size of the component being repaired [4].

Further repair geometry requirements are described in the engine manual, features such as rounded blend corners and aerofoil edge recreation. Repairs must have a major-to-minor axis rotation sufficiently large as to not cause a new, or exacerbate an existing stress concentrating feature.

#### 1.4.1 Mechanical boreblending

In-situ repairs are an important part of Rolls-Royce's engine maintenance, and this process has been carried out using mechanical boreblending equipment since 2003. Boreblending involves mechanical material removal via grinding and polishing tools which are inserted into the engine through inspection ports. Mechanical grinding is performed manually, with skilled operators performing one repair per working shift. The bulk of repair time is spent on polishing the repair geometry. Figure 1 shows some blade edge damage, and a mechanical repair performed by boreblending.

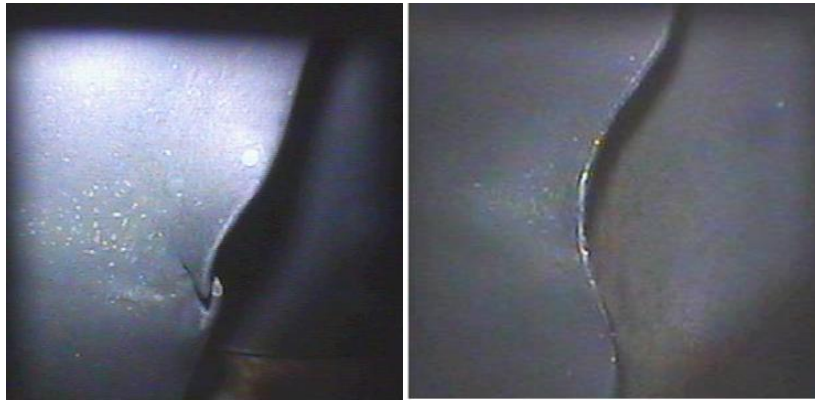


**Figure 1 - Blade edge SRF a) before and b) after mechanical boreblending**

### 1.4.2 Laser boreblending

Laser systems generate monochromatic light, i.e. light photons of a single, or within a very narrow bandwidth, wavelength. The wavelength and bandwidth depend on the gain medium material used in the laser system, and the purity/combination of materials within the gain medium. Using a pulsed laser enables repair technicians to remove material in a highly accurate, fast, and easily automated manner. Pulsed lasers generate pulses of monochromatic (much like non-pulsed laser systems) light which, when directed onto a material surface, imparts energy over a very short time. This results in a high peak power input to the material surface which will rapidly heat it. This heating will melt or, if the photon energy exceeds the bond energy between atoms in the material surface, ablate some material. By directing the laser through optics and mirror systems, accurate material removal can be achieved. By automation of this process, pre-defined laser scan paths, along with process parameters (power and pulse frequency) can be used to machine features such as blend repairs carried out by conventional boreblending tools. Visible red laser light can also be directed through the same equipment as that which is used for the machining operations to visually trace repair geometries on the workpiece before performing material removal, as shown in Figure 2.

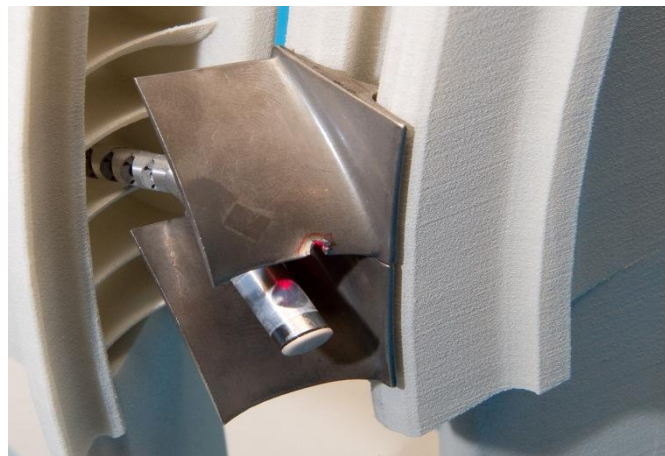


**Figure 2 – Mock-up scenario with red pointer laser directed onto SRF on compressor component using prototype laser boreblending deployment hardware**

## 1.5 Project objectives

The objectives of the project documented in this thesis are addressed individually in each chapter, and are summarised here;

**Material Removal** – Component material must be removed by use of a nanosecond ( $1 \leq \tau \leq 999 \times 10^{-9}\text{s}$ ) pulsed Yb:YAG laser. This will be used to ablate material in multiple small volumes (craters) to achieve the desired three-dimensional blend profile. A Yb:YAG laser was chosen for its output wavelength,

being able to effectively machine nickel alloy components, as absorption of infra-red photons generates thermal effects in the material allowing ablation and melting of the component surface, facilitating material removal. Additionally, Yb:YAG lasers are known for their ability to produce high peak output powers without damage to the laser system itself.

**Minimise Material Damage** – Through selection of optimal parameters (which will also give maximised MRR), thermal morphological damage to the component will be minimised.

**Ablated Feature Modelling** – Through experimental calibration between the chosen nanosecond laser system and target component material, a predictive model will be developed to allow a user to estimate volumes of material removed through a set of laser processing parameters. It will also allow for the modelling of complex micro-features and characterisation of surface topography.

**Maximise Material Removal Rate** – To minimize process times, material removal rate (MRR) will be maximised to achieve the desired blend profile. This will be achieved by using optimal laser parameters allowing for large volumes of material ablation per pulse, with minimal volumes of melted (non-ablated) material, reducing the effect of material re-deposition and other negative secondary effects.

**Model Validation on Diamond and Nickel targets** – The mathematical model developed will be validated on both diamond and nickel alloy targets to demonstrate its usefulness in predicting both macro and micro scale features produced by pulsed laser ablation.

**Quantify Repair-Induced Fatigue Performance Change** – Components repaired by optimised laser repair processes will be put through High-Cycle-Fatigue (HCF) testing to quantify any reduction in fatigue life brought about by the repair process, and the laser parameters themselves. These component repairs will also be compared to best-practice mechanical blending and un-repaired components. This will give confidence in the structural integrity of laser repaired components and qualify the use of laser ablation as a processing option for in-situ repairs. Fractographical work will be carried out on components that have gone through HCF testing to identify and characterise any fracture mechanics and behaviours that may occur as a result of the different repair methods.

**Optical Head Operation** – Repairs will be generated using a prototype deployment probe and optical head assembly, representative of the equipment intended for in-situ repairs. These components will also be submitted for HCF

testing and validation. Limitations of the equipment, and side effects of its proximity to the workpiece will be addressed.

## 1.6 Thesis structure

This thesis has chapters on the following topics, with each contributing either practical or scientific findings towards the projects objectives as a whole.

**Chapter 2** presents a review of both published academic literature and industrial documentation relevant to the aims and objectives of this project. It investigates various laser machining technologies and the major concerns most commonly associated with pulsed laser ablation on aerospace materials and components. Methods for measurements and analysis are discussed, and how these can affect component performance and life expectancy.

**Chapter 3** lists the equipment and experimental procedures which were used to generate the bulk of experimental data in this project. Where one-off or infrequent procedures and/or equipment usage occurred, their details are given at the appropriate place in the relevant chapter.

**Chapter 4** documents a metallurgical study investigating the negative effects of pulsed laser ablation on Nickel alloy components. Effects such as material recast, oxidation and cracking are considered as well as material phase changes and their implications on component mechanical properties. It will show which of the key process variables involved in pulse laser ablation have the highest impact on these secondary effects.

**Chapter 5** describes a mathematical model, derived from simple concepts surrounding pulsed laser ablation of solid targets. Taking a range of effects such as laser beam divergence, beam kinematics and laser-material interaction the model is able to predict surface topography evolution throughout a pre-defined laser ablation process. It presents validation of the surface prediction on both diamond and Nickel alloy targets, where the modelling of material redeposition is included into validation on Nickel alloys. By using results from Chapter 3, this model can also provide process optimisation relevant to the objectives of this project.

**Chapter 6** presents further validation on the model presented in Chapter 5, where its limitations are addressed. Both the model and validation techniques are adapted to extend the usefulness of the model to predicting more complex micro-scale geometries, and larger macro-scale geometries. In doing this, this chapter shows that the model can be used for both micro-machining applications where complex

geometries are generated, and larger scale processes where target mass removal and net-shape feature generation is the aim.

**Chapter 7** presents two High-Cycle Fatigue (HCF) experiments performed on components machined using optimised laser operating parameters defined in the previous chapters. These tests assess the performance of repair geometries, and the metallurgical integrity of the repaired components in line with the optimised laser operating parameters and the repair geometry limitations as brought about by the repair equipment which these repairs will be performed with.

**Chapter 8** documents the process of repair generation using the prototype equipment produced by OpTek Systems, with which Rolls-Royce intend to perform these repairs in the field. It will show an optical bench set up with this prototype equipment, and describe the limitations of its operation due to its mechanical and optical properties. It will also look at how some of the material ejected from the ablation process impacts and settles upon solid surfaces surrounding the component, and what these ejected particles are made from.

**Chapter 9** presents a summary of the findings and observations made throughout this thesis, giving an overall reflection on the progress made towards the initial goals of the project. It also offers suggestions for further work and research that could build upon findings made in this project.

Figure 3 shows how findings from each of the thesis chapters will link to the following chapters.

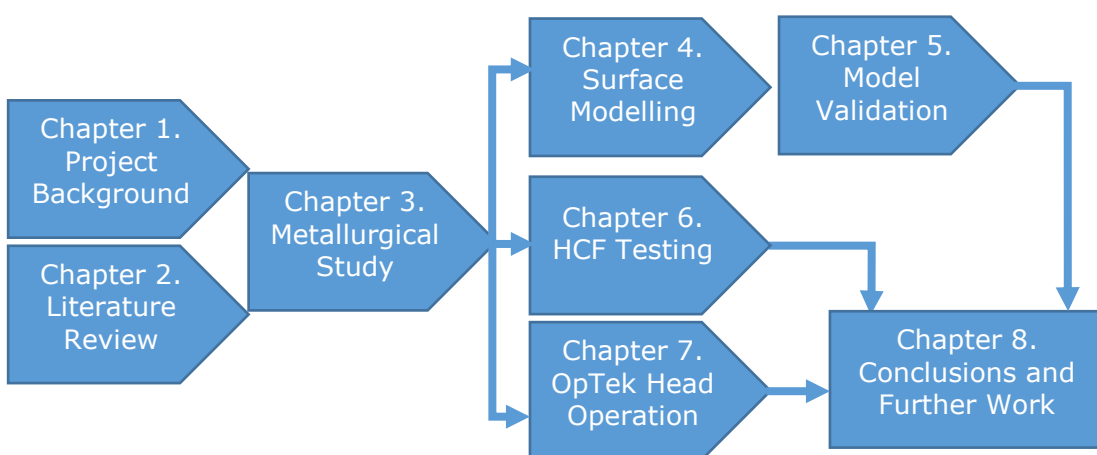


**Figure 3 - Flowchart for thesis chapters**

## 1.7 Highlights of scientific contributions from thesis chapters

Work carried out in this thesis has contributed to scientific advancement in academic and industrial contexts. The following points describe these contributions.

- 1) Development of a predictive mathematical model capable of surface topography simulation for a calibrated laser system and target material. In taking effects such as laser beam divergence and material redeposition this model advances beyond previously developed modelling methods found in literature. This model allows for the prediction of material removal rates and qualitative analysis of resultant surface topographies for any given laser ablation process with a calibrated system.
- 2) Extension of the aforementioned mathematical model to predict complex micro-geometries with short pulse laser systems on diamond targets, and larger macro-geometries on Nickel alloys in an On-The-Fly balancing scenario. This allows for process optimisation where specific masses are to be removed from rotating components.
- 3) Assessment and optimisation of the laser ablation process with a nanosecond pulse duration on Nickel alloy targets. This assessment involved measurement of negative secondary effects on the metallurgical properties of the target. In determining the relationship between values for each laser machining parameter and these secondary effects, processes can be optimised to reduce these effects whilst maximising material removal rates through use of the mathematical model described previously.
- 4) Fatigue and fractographical analysis of repaired components provided confidence to industrial parties invested in the project described in this thesis. Through demonstration of component fatigue life deficits being above a minimum requirement set by Rolls-Royce, laser ablation has been shown to be a viable repair technique for In-Situ maintenance of HPC components in the Trent XWB-84k engine.

# Chapter 2. Literature Review

## 2.1 Nickel usage in aerospace engines

Nickel-based superalloys such as INCONEL® 718 and NIMONIC® 105 are commonplace in aerospace technology due to their high-temperature mechanical performance; specifically, their strength, stiffness, and metallurgical stability. Given these properties, these alloys are ideal for use in some of the hotter parts of a modern turbofan engine, where components are held at high temperatures for several hours at a time, whilst being subjected both low and high cycle loading regimes. Alloying components and conditions are carefully selected to give these materials these capabilities, brought about by resistance to creep and oxidation [5].

### 2.1.1 Nickel alloy Metallurgy

INCONEL® 718 is a Nickel base alloy comprised of a face-centre-cubic (FCC) gamma ( $\gamma$ ) matrix [6] and additional phases. Its main strengthening phases are a gamma prime ( $\gamma'$ ) FCC comprised of Nickel and Titanium or Aluminium ( $\text{Ni}_3\text{Ti}$  or  $\text{Ni}_3\text{Al}$ ) [7], and a gamma double prime ( $\gamma''$ ) body-centre-tetragonal (BCT) phase comprised of Nickel and Niobium ( $\text{Ni}_3\text{Nb}$ ) [8]. Both INCONEL® 718 and NIMONIC® 105 are similar in composition and microstructure, and both are used to manufacture components in aero engines. It is suitable for use in high pressure/temperature environments, such as this area of the engine, due to its high-temperature strength, derived from its microstructure. This is solid solution strengthened and precipitation hardened by formation of its  $\gamma''$  and  $\gamma'$  phases as a result of its alloying additions [9]. The composition of INCONEL® 718 by weight percentage is provided in Table 1 below.

**Table 1 - Elemental Composition of INCONEL® 718 [80]**

Element	Symbol	Composition (wt%)
Nickel	Ni	50.00-55.00
Chromium	Cr	17.00-21.00
Niobium	Nb	4.75-5.50
Molybdenum	Mo	2.80-3.30
Titanium	Ti	0.65-1.15
Aluminium	Al	0.20-0.80
Carbon	C	0.08 max
Boron	B	0.006 max
Silicon	Si	0.35 max
Sulphur	S	0.015 max
Phosphorus	P	0.015 max
Iron	Fe	Balance
Copper	Cu	0.30 max
Manganese	Mn	0.35 max

This alloy can undergo phase change when held at elevated temperatures for extended periods of time (aging) [10]. A weaker, plate-like  $\delta$  phase found mostly at grain boundaries can be seen forming in Figure 4.

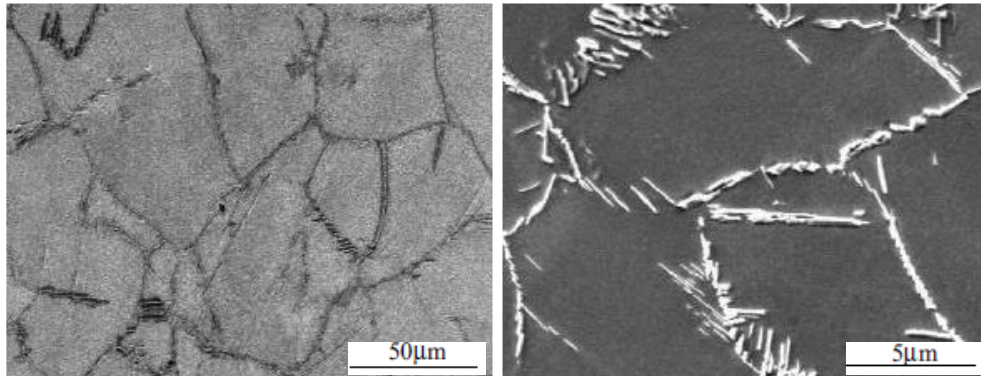


**Figure 4 - Heat-treated In718 microstructure showing a) individual grains and b) Inter-granular  $\delta$  phase [10]**

The growth of these plate-like  $\delta$  phases increases with time that the material is held at elevated temperatures, as shown in Figure 5 below.

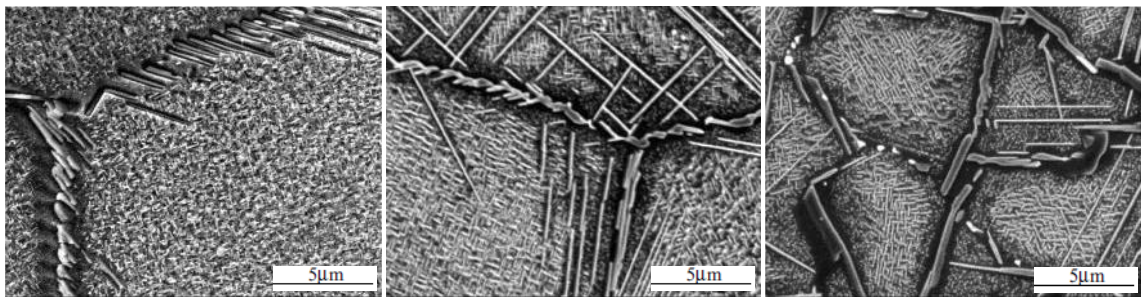


**Figure 5 -  $\delta$  Phase growth in In718 by aging at 760°C for a) 100h, b) 350h, and c) 500h [10]**

To strengthen this alloy, intra-granular  $\gamma''$  phases are formed during heat treatment. These form as elliptical phases typically 1 $\mu$ m or less in diameter (dependent on heat treatment regime). Figure 6 shows this  $\gamma''$  phase enclosed by  $\delta$  phase plates.

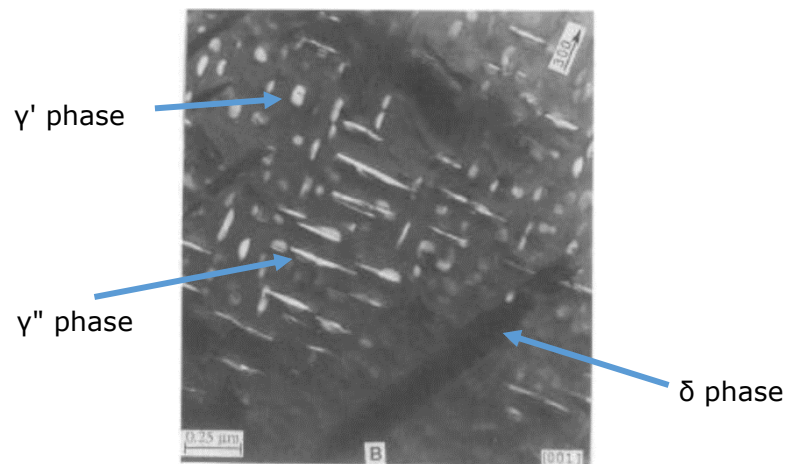


**Figure 6 - In718 ages at 649°C with  $\gamma''$  phase enclosed by  $\delta$  phase plates [10]**

## 2.2 Fatigue and failure modes of compressor components

### 2.2.1 Common damage and failure modes of Ni-Alloy components

Components made using INCONEL® 718 typically have a polycrystalline structure, and as such failure can occur inter or intra-granularly dependent on strain rate [11]. It should be noted that INCONEL® 718 can undergo recrystallization at temperatures above 1065°C, given sufficient time, and as such, grain size alteration can occur. These altered grain sizes can then have adverse effects on the high-temperature strength of the material and the component, which may lead to component failure after a lower number of loading cycles than would be expected. Common failure modes for nickel alloy compressor blades include foreign object damage (FOD), erosion, corrosion, and high cycle fatigue (HCF) [2].

Cracks tend to occur as a result of tensile loading, especially if there are surface anomalies such as voids or micro-pores pre-existent in the material microstructure, shown in Figure 7. Accelerated propagation of cracks due to tensile stresses can result in catastrophic component failure, especially at elevated temperatures, pressures, and loads. As such, the introduction of compressive stresses within the component surface can be beneficial to cancel out or reduce any tensile stresses arising from loading or processing. In general, compressive stresses are therefore beneficial where high cyclic loading is present due to their ability to reduce and negate the acceleration of crack initiation and growth arising from tensile stresses [12].

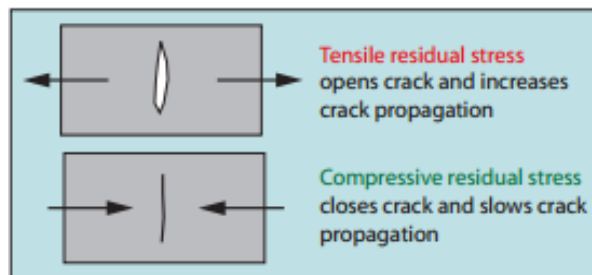


Figure 7 - Effect of Residual Stress on Cracks [13]

Compressor components can fail from stress induced by pre-existing flaws such as machining marks and striations [14], or foreign object damage arising from particulate inhalation into an engine which is in service [15]. The geometric and material imperfections caused by these mechanisms can lead to concentrations of stress within the component. Low cycle, high stress loading such as compressor stall/surge, and take of/landing cycles can cause component failure as well as high cycle loading through normal operation.

## 2.3 Component repair

### 2.3.1 Background to laser operation

Used throughout numerous fields of engineering and scientific research, light amplification by stimulated emission of radiation (LASER) has been of growing importance since its discovery and development in the 20<sup>th</sup> century. Laser technology involves the stimulation of a gain medium through some form of energy pump, typically electrical current or concentrated pulses of light. The stimulation within the gain medium generates monochromatic light (emitted radiation). Atoms within the gain medium may either emit a photon spontaneously (through their electrons moving from a high energy state, 'E<sub>2</sub>', to a lower one 'E<sub>1</sub>') or have photon emission be stimulated by an incoming high energy photon, when their electrons are already in a high energy state. An atom absorbing an incoming photon when its electrons are in a high energy state will emit two photons of identical phase, wavelength and propagation direction. The incoming photon may originate from the pump source, or another atom in the gain medium material. It is this process that allows for the amplification of light within a gain medium, and is shown below in Figure 8.

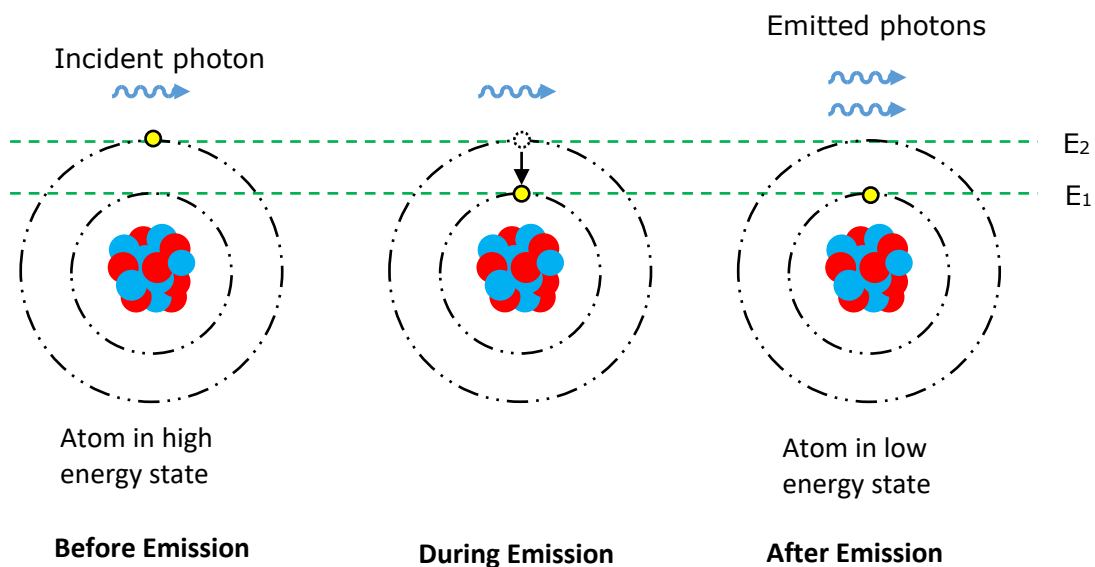


**Figure 8 - Principle of stimulated emission of laser radiation**

This emitted light is typically made to optically resonate by use of mirrors at the ends of the gain medium, being amplified upon each reflection through the mechanism described previously. One of these mirrors may be partially transparent, and as such a portion of the resonating light within the gain medium will pass through and be outputted as a laser beam [16]. This is shown in Figure 9.

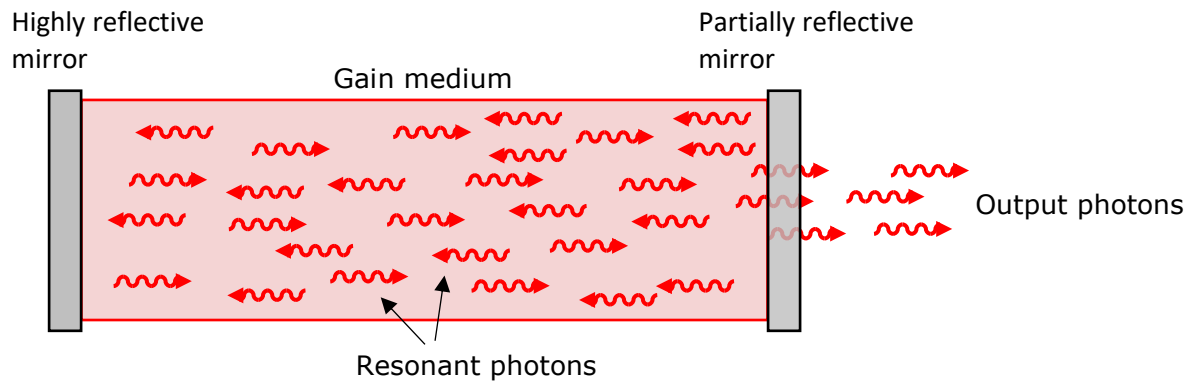


**Figure 9 - Principle of laser amplification within a gain medium**

With use of additional optical elements, characteristics of the outputted laser radiation such as wavelength, divergence and polarisation can be modified to suit a desired function. Laser machining involves the use and control of some key process variables (KPVs), specifically; average power output "P" (J/s), laser spot diameter " $\phi$ " (m), and in the cases where the laser beam is being redirected, laser scan speed " $v_f$ " (m/s), and wavelength  $\lambda$  (m). For a given laser system, laser wavelength and spot diameter is typically held constant as it is a feature of the laser and optics system itself and hence difficult to modify throughout a machining process.

### 2.3.2 Laser beam characteristics

Laser systems generate light beams with some characteristics which can be modified with external optical devices, such as; beam diameter, wavelength, divergence angle, and focal spot diameter. A number of parameters have been defined to describe these characteristics, such as a beam quality factor " $M^2$ ". This describes how tightly the beam can be focused, compared to a theoretically perfect, Gaussian beam it is. It is given by the beam parameter product of the actual beam, divided by the beam parameter product of a Gaussian beam. The beam parameter product is given by the product of the beam radius (at the focal plane) and the far-field beam divergence half-angle [17]. A beam with quality  $M^2=1$  displays divergence equivalent to a perfect Gaussian beam, and an  $M^2$  value greater than 1 describes a beam which will diverge more readily than a Gaussian beam [18],[19].

A beam with a gaussian shape will have an energy distribution such as the one shown in Figure 10.

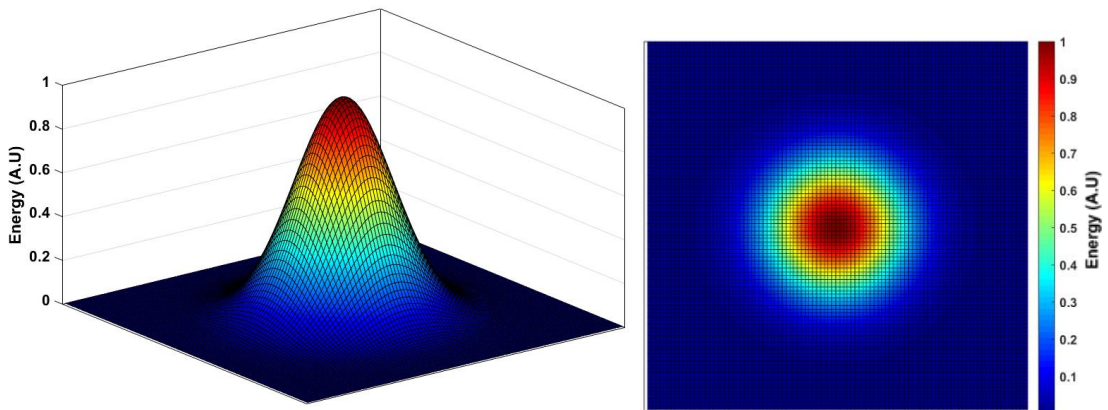


Figure 10 - Computer generated Gaussian beam profile

In reality, aberrations within the optics of a laser system such as imperfectly shaped lenses or mirrors will lead slight distortions within the laser beam itself, and its focal pattern will not match that of a perfect gaussian beam. Figure 11 shows an example of an imperfect beam, with aberrations indicated with arrows and an obvious non-circularity across the beam cross-section.

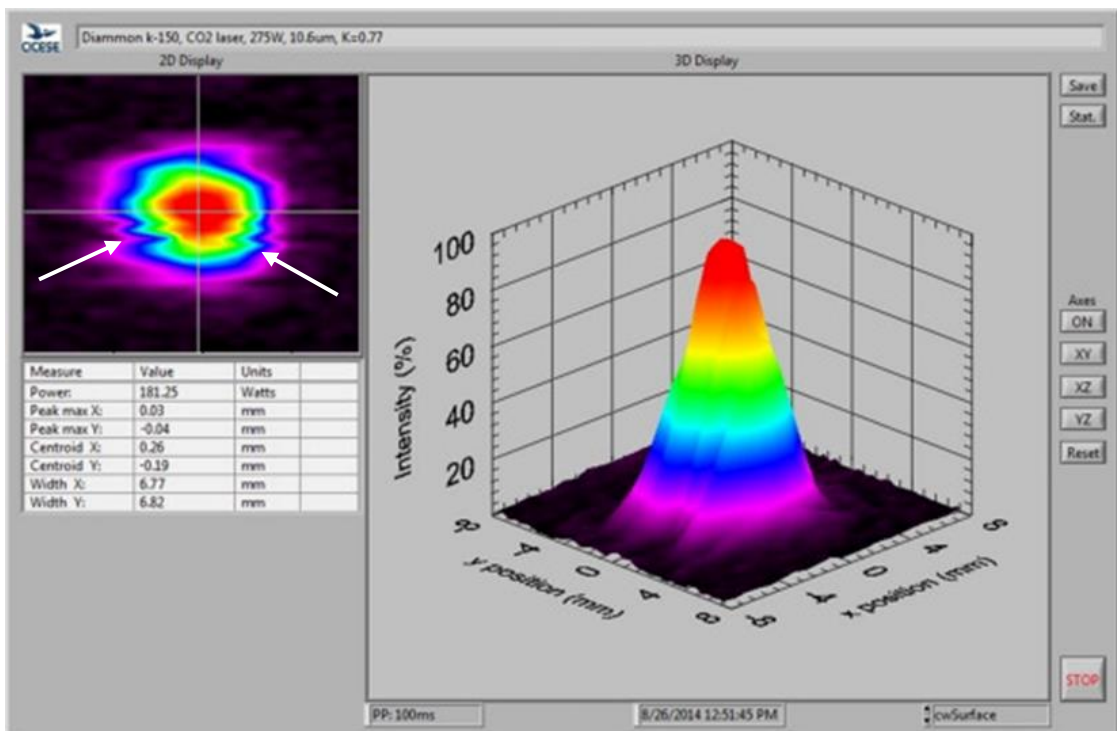


Figure 11 - CO<sub>2</sub> laser beam profile exhibiting imperfections and aberrations [81]

Laser beams are generated with a particular transverse electromagnetic (TEM) mode, manifesting as a specific intensity field taken in a plane perpendicular to the beam's propagation direction. These TEM modes result in a number of high-intensity peaks within the beam's energy distribution, however for the most simple,

lowest order TEM mode ( $TEM_{00}$ ), there is only a single peak in the centre of the beam energy profile, such as the one shown in Figure 10,.

### 2.3.3 Laser pulsing

When lasers are operated with a simplistic gain medium and optical resonator as described above, the power output of the laser will be a simple function of the power input to the gain medium through the energy pumping system. This is known as continuous wave operation. As such, the power that the laser can impart into a workpiece is limited by the input power. Many applications may require rates of energy absorption into the workpiece required for material modification (removal, melting) far higher than those that continuous wave operation can provide. A range of processes and their energy requirements are shown in Figure 12.

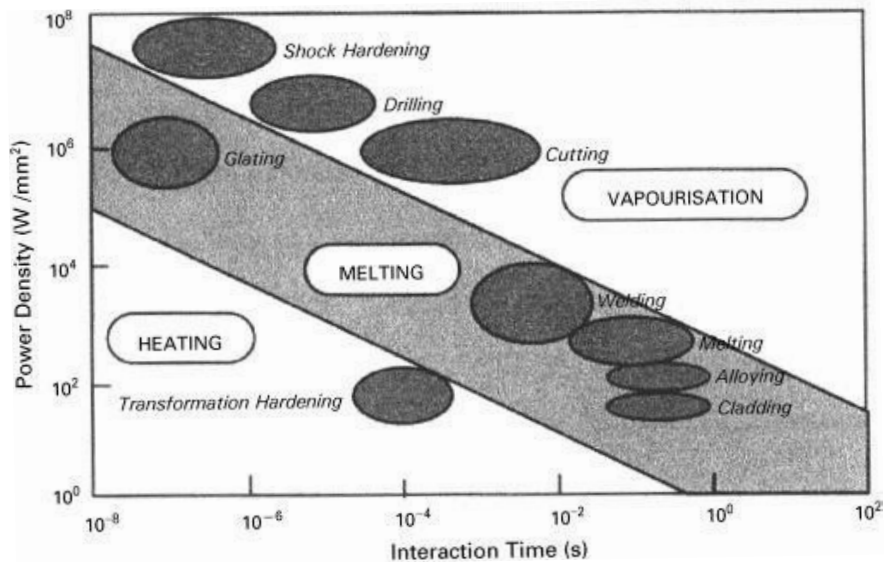


**Figure 12 - Power requirements for material modifications using lasers [20]**

It should be noted that these various processes require different power densities, and therefore if the laser beam focal area can be reduced, more energy will be imparted over a smaller area. The term given to the amount of laser energy distributed over a given area is fluence, and is typically given in units of  $J/cm^2$ .

To produce higher power output levels, lasers can be operated in pulses, allowing energy to accumulate within the resonator and then releasing this energy over short periods of time resulting in very high peak power output levels. This pulsing is achieved through various methods, each with different pulse characteristics such as pulse duration, pulsing frequency, and pulse energy. Three common methods of are listed below;

#### 2.3.3.1 Pulsed Pumping

Pulsed pumping of lasers involves charging and rapidly discharging electrical energy, typically through use of capacitors, such that gain media are energised in controlled pulses of energy. Pulse frequency is limited by the frequency at which the pumping system can be pulsed [21].

#### 2.3.3.2 Q-Switching

By attenuation of the optical resonance within the laser gain medium, light can be selectively allowed to exit the gain medium, or be contained allowing optical feedback [21]. This may be done either automatically, (mechanical shutter wheels, electronic control) or passively through selection of materials which allow transmission and certain light level thresholds. Pulses generated by this method are typically of high pulse energy ( $\mu\text{J}$  to  $\text{mJ}$ ) and hence peak power, frequencies in the order of kilohertz, and pulse durations as short as nanoseconds.

#### 2.3.3.3 Mode-Locking

Pulses of extremely short durations, anywhere from picoseconds to femtoseconds are achieved by creating self-interference of light waves within the optical cavity of the laser. By placing the mirrors at either end of the gain medium at a distance equal to an integer "q" multiplied by the half-wavelength ( $\lambda/2$ ) of the light being generated, standing wave modes can be set up within the optical cavity. By interference of these modes, constructive interference will generate pulses which will travel up and down the gain medium, and this will be accomplished in extremely short timescales due to the speed of light in the gain medium. These pulses are typically of very low energy ( $\text{nJ}$  to  $\mu\text{J}$ ), produced at very high (megahertz) frequencies [21].

### 2.3.4 Directing Laser Energy

Laser light can be redirected through use of mirror systems and lens arrangements, commonly driven by galvanometer scanners to give control over X and Y locations within a laser scan field.

Industry standard galvanometer scanners can be operated with an angular accuracy of  $10\mu\text{rad}$  or better [22]. Linear accuracy (i.e. the accuracy of beam placement on a workpiece) will depend on galvanometer angular accuracies, and any additional optical components being used such as lenses. Figure 13 shows how two galvanometer scanners combine their axes of rotation to create a near-square scan field for laser direction. The maximum values of angles  $\Phi_1$  and  $\Phi_2$  will determine the maximum size of the laser scan field

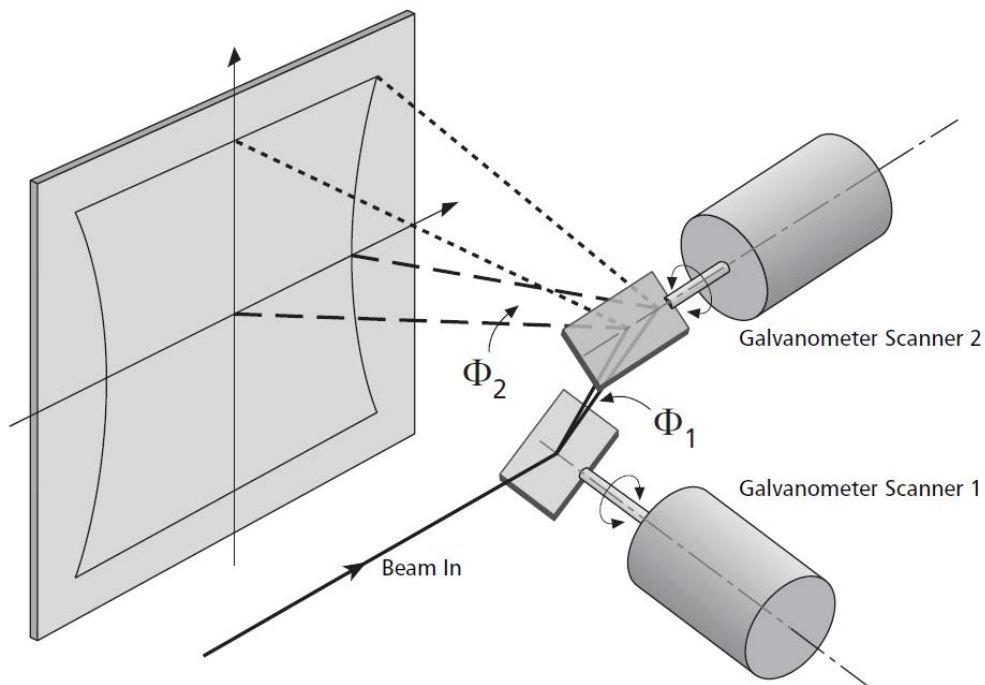


**Figure 13 - Typical galvanometer scanning system for directing laser light [23]**

## 2.4 Laser machining of nickel superalloys

### 2.4.1 Laser-alloy interaction

As there is an increased need to machine ever harder and tougher materials such as titanium and nickel superalloys for manufacturing components at macro/micro scale level, pulsed laser ablation (PLA) has become a viable processing method with the decrease in capital cost [24] and quick technology adoption across industries (e.g. medical, aerospace, defence). Thus, using PLA instead of other manufacturing technologies has unique benefits: (i) it allows removal of very small controlled masses of target materials at very high precision (spot diameters  $< 60\mu\text{m}$ ); (ii)

damage to the material structure of the component can be controlled/minimized if laser type/parameters are carefully selected for each workpiece material [25], [26]; (iii) it has the ability to be easily and safely automated; (iv) it allows machining of tough and hard materials [27] which would be very difficult to machine using conventional cutting methods.

#### 2.4.2 Modes of material removal

Laser radiation can induce a change of phase in a metal target, resulting in the removal of a volume of material dependant on the amount of energy absorbed, and the rate of absorption. Material removal may be through melting or ablation, and this may be as a direct or indirect result of the laser radiation. These modes of material removal will occur at different rates dependent on the characteristics of the laser system in use.

If the duration of the pulse ( $\tau$ ) is very short, the interaction time between the laser beam and the material lattice may be insufficient to induce thermal effects. This will depend on the time taken for lattice electrons to cool ( $T_e$ ) and for thermal energy to transfer from one lattice atom to another ( $T_i$ ).

Material melting occurs during ablation where pulse durations are tens of picoseconds or longer [28] ( $T_e < \tau < T_i$ ).

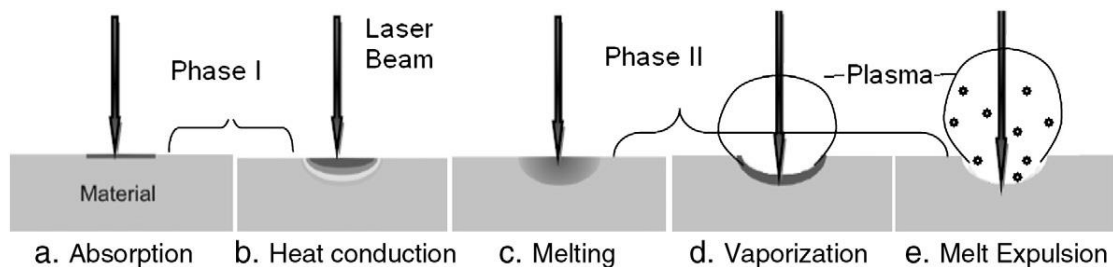


**Figure 14 - Material heating, removal and expulsion in short to long pulse ablation [29]**

Material melting and expulsion results in redeposition of some of the removed material back onto the parent material surface. Figure 15 shows some clear redeposition in a rim around an ablated crater. Melting and redeposition occurs more when the laser pulse energy is greatly above the threshold energy required for ablation with picosecond pulse durations [30].

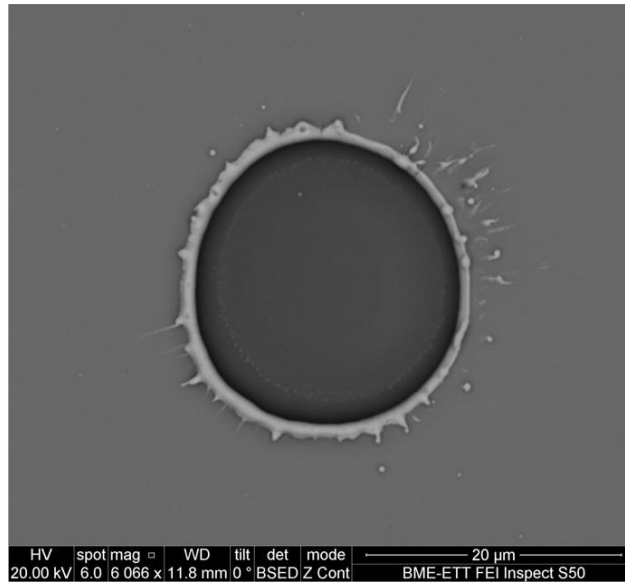


**Figure 15 - Crater ablated in Nickel by a single 30ns pulse showing material redeposition [28]**

In ablation with ultra-short pulse durations (femtoseconds) no melting is seen and instead material removal occurs almost exclusively as sublimation [31], [32]. This is due to there being insufficient time for heat to spread throughout the lattice as the pulse duration is much smaller than the time required for lattice atom heating ( $\tau < T_e < T_i$ ). Figure 16 shows an example of a laser ablated feature, a hole in steel foil ablated using 200 femtosecond pulse durations. It shows no visible material redeposition resulting in the edges and walls of the feature being very well defined.

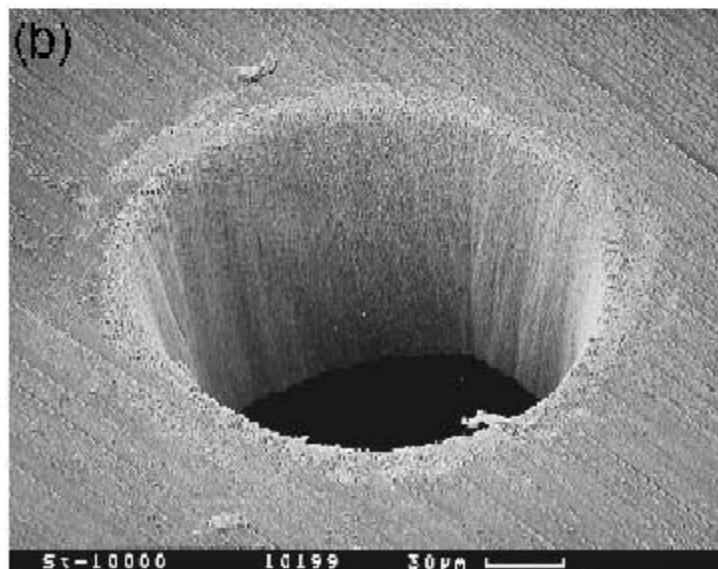


**Figure 16 – Laser ablated hole in steel foil with a pulse duration of 200fs [31]**

In ablation where pulse durations range from picoseconds to nanoseconds, the depth of the ablated crater from each pulse has a logarithmic relationship with the laser pulse energy [28], [33], [34].

### 2.4.3 Secondary Effects of laser machining

Thermal processing such as laser ablation (within the nanosecond regime) presents secondary effects aside from the bulk removal of material. These effects can negatively affect the properties of the material (both metallurgically and topographically).

#### 2.4.3.1 Residual Stresses

Stresses can be introduced into the component material in a variety of ways; mechanical manufacturing methods, in-service deformation, and thermal loading. These stresses can manifest in three main mechanisms;

- Macro-stresses over several grains within the crystal lattice
- Micro stresses over smaller regions, typically up to one single grain or inter-granular
- Crystal lattice anomalies (dislocations, inclusions etc.)

#### 2.4.3.2 Material recast Layer

During laser processing, material can become molten in localised areas around the treated area, and any molten material that is not ejected from the component as part of the processing will re-solidify. This layer of re-solidified material is known as recast. This layer undergoes re-solidification in a largely uncontrolled manner, and as such will have unpredictable properties. As such, the extent to which recast material is generated through any material processing method should be minimised [1]. In general, shorter pulse laser ablation gives rise to less recast generation, with "cold" femtosecond ablation creating negligible, or no, recast layer thickness. In general, at higher pulse energies more recast is created. As such, for high-power ablation applications, shorter pulse duration is necessary to minimise this negative phenomenon. Higher pulse repetition frequencies at high average laser power output however may produce lower recast, as individual pulse energies will be lessened. Previous conclusions have been made that recast layers have higher micro-hardness in comparison to bulk parent material, however strength and high-cycle fatigue properties may vary [35]. Figure 17 shows recast layer formation on top of parent material after ablation.

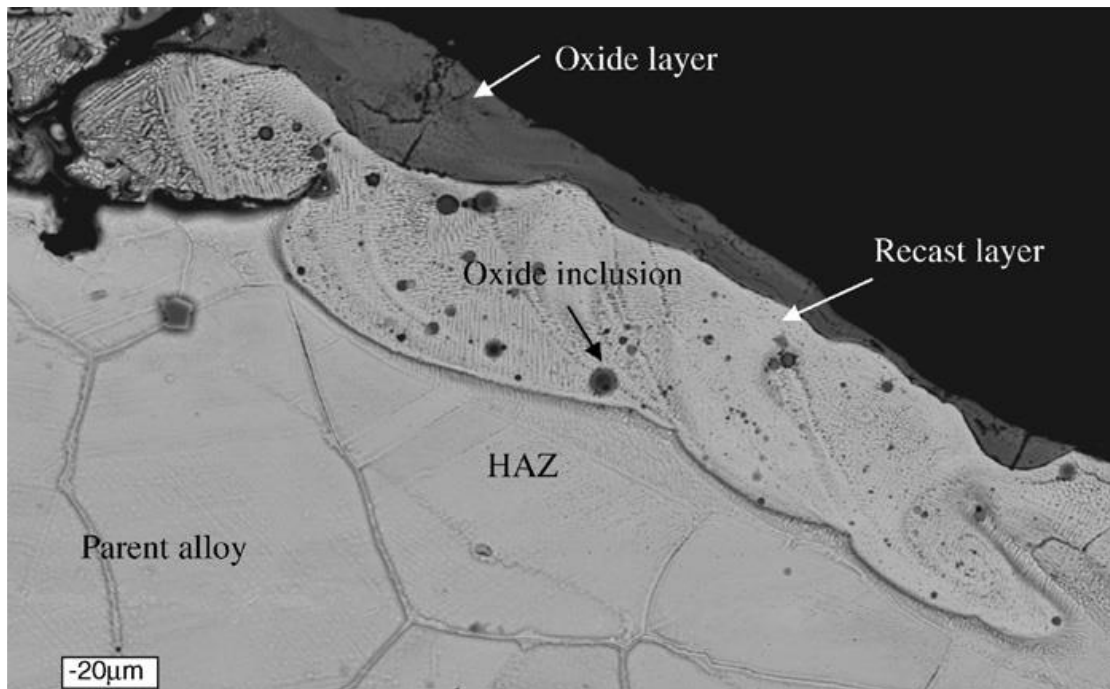


**Figure 17 – Oxide and recast layer present after ablation of NIMONIC® 263 nickel superalloy [37]**

#### 2.4.3.3 Micro-cracking surface and internal cracks

It is stated that after microstructural analysis cracking patterns and layouts can be differentiated by visual analysis of FEG-SEM images and classified as different morphologies, namely; “tight (closed with little visible material separation), medium (single cracks with visible material separation), and complicated (cracks with multiple branches in differing directions) morphology” [36]. This is illustrated in the image below in Figure 18.

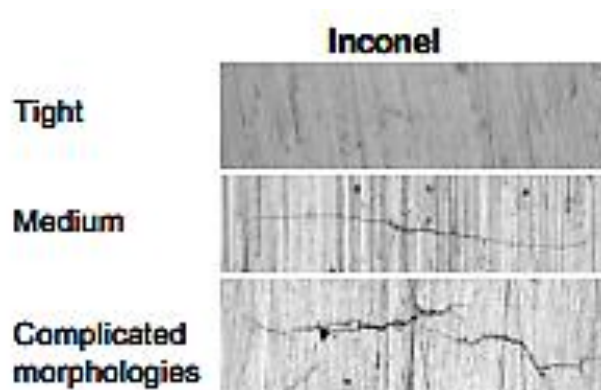


**Figure 18 - Crack Morphology Categories for INCONEL® 718 [36]**

Experiments have shown that micro-cracks generated and extending from the ablated surface seemed to rely heavily on the angle of incidence of the laser beam [37], with higher angles of incidence resulting in larger HAZ, oxidation and more cracking.

#### 2.4.3.4 Surface Roughness

Rough and uneven surfaces can be measured in either 2 or 3 dimensions to determine a surface roughness characterisation of a processed area of material. In general, lower surface roughness will result in better fatigue performance, where high roughness reduced fatigue life [38]. Surface roughness is defined as the arithmetic mean of the absolute departures of the roughness profile from the mean line.

#### 2.4.3.5 Material oxidation

Oxidation can occur when metallic ions from the parent material bond interact with atmospheric oxygen, particularly when it is processed or held at high temperatures for extended periods of time, typically a number of hours [39]. When nanosecond pulse duration is used laser ablation can produce a layer of surface oxide when processing occurs in normal air, particularly at low scan speeds; where surface heating is prolonged enough to raise surface temperatures to a critical level, allowing the dissolution of oxygen into the parent material [40]. Nickel alloys may have alloying elements such as chromium that give the alloy resistance to corrosion and oxidation [39].

Oxides tend to be brittle in nature and will have an adverse effect on the fatigue performance of a component, should their localised concentration become too high in areas of the component which are subjected to high stresses. It follows from this that high concentrations of oxide can act as crack initiation sites. On INCONEL® 718 laser machining can create layers of oxide with a copper-like or dark brown colour [35]. Figure 17 shows oxide layer formation on top of recast material created during laser ablation, with isolated spots of oxide inclusion beneath the bulk oxide layer.

#### 2.4.3.6 Heat affected zone

The heat affected zone (HAZ) is defined as the zone surrounding the directly laser-irradiated area of material. This zone is usually subjected to predominantly thermal effects such as melting (but not vaporisation) and re-solidification, or phase changes [41]. Again, this zone can have poorer mechanical and material properties than the unaffected parent material, for example reduced strength through phase change [41]. As previously stated, reduced thermal effects are seen when using shorter (picosecond or femtosecond) pulses and as such the size of the HAZ can be controlled and minimised by using shorter pulses. This is likely due to less time for heat to spread throughout the material microstructure. Figure 19 shows a diagram the effects of pulse duration on bulk material heating and damage. Longer pulses can (no shorter than a few tens of picoseconds) generate recast material, cracking

and large heat affected zones, whereas ultrashort pulses (femtoseconds) do not present these effects.

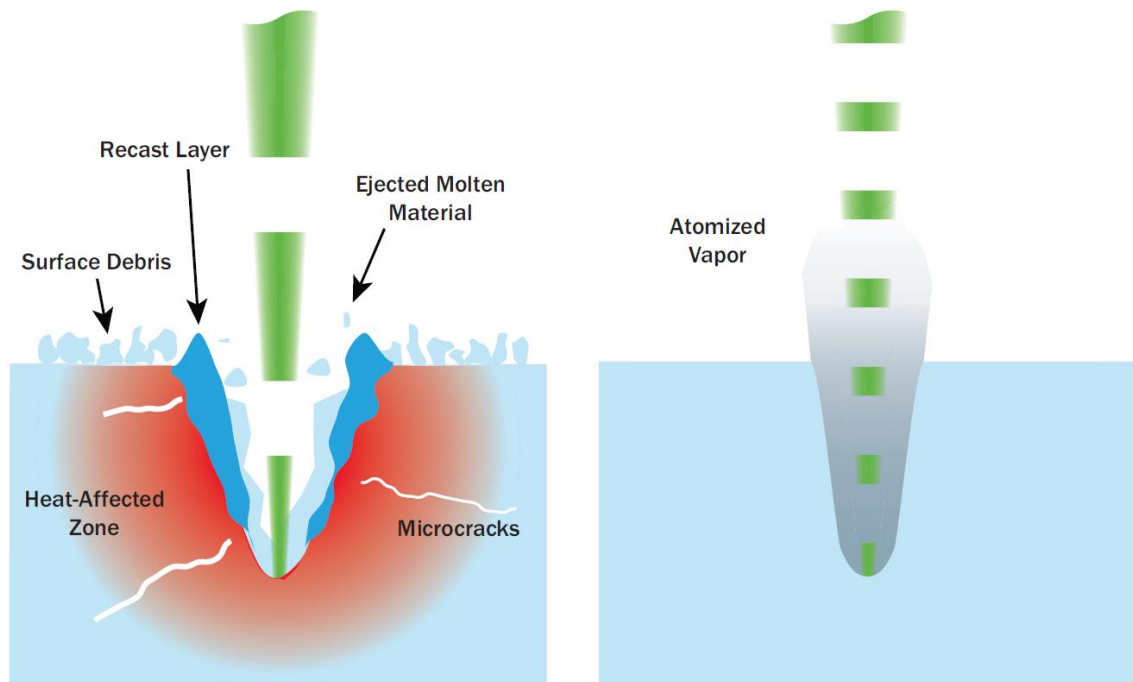


**Figure 19 - Heat affected zones generated by a) short (ns - ps) and b) ultrashort (fs) pulse durations in laser ablation [82]**

#### 2.4.4 Modelling of laser machining

Despite the advantages of PLA for generating complex shapes, it very often requires specialist knowledge/integrated CAM control to machine high precision features. This is due to the lack of a universally applicable model to predict the outcome of the laser machining processes, as is already available for other dwell time dependent process like water jet machining [42]. PLA machining modelling has been highly researched over the past decade but the focus has been mainly on experimental determination of laser parameters to enable processing the workpiece surfaces at required surface precision and accuracy [27] rather than on modelling to improve the predictability of laser machined surfaces. In this context, although the mathematical modelling of the surface to be obtained after PLA (as a superposition of individual laser craters) could lead to a step-change in controlling PLA process (avoiding expensive “trial and error” approaches), published literature suggests that limited attention has been dedicated to this research field. More attention has been focused on developing physics based models of how the laser/beam works instead on the micro/macro geometry of the laser ablated surfaces.

Existing analytical models can be divided into three different categories [27]: those based upon simplified assumptions, described using input and output parameters,

which are then related using empirical data. An example of this approach is Yilbas' model for predicting kerf width of holes using an oxygen-assisted laser cutting mild steel [43]. Other types may rely on FEM methods such as a model for predicting material removal and groove smoothness by Kim et al. [44]. The third type incorporates artificial intelligence methods, utilising knowledge from data bases with learning abilities e.g. work by Yousef et al. [45] to predict the required pulse energy for a specified crater depth and diameter. All of these models are difficult to apply because they only cover very specific situations or require extensive set up and computing power. Hence, there is a need for a computationally fast model with real process relevance.

Of specific importance has been research which aimed at investigating the effect of material removal without structural damage to the component such as oxidation or metallurgical changes [25], [46]. The material removal rate is highly dependent on the energetic (e.g. fluence) parameters of the laser as well to the material properties (e.g. thermal conductivity, specific heat capacity) and its surface quality (e.g. roughness) [47]. It has been observed that there is a relationship between fluence and material removal [34]. This allows the prediction of material removal although it neglects to consider further effects, which would allow making predictions of the resulting surface texture. Of course, this is by no means the perfect solution. Using multi-physics models, however, to predict the effect of the intensity over time increases calculation time for minor accuracy improvements of certain modelling aspects.

While there has been research into the surface roughness after pulsed laser ablation processes, it has been focused on considering a set of standard parameters [48], which lead to a certain quality of surface finish rather than on modelling the surface and to determine its features in an accurate way. This is of limited use when it comes to the prediction of macro-geometries (e.g. shapes) of PLA surfaces. Furthermore, most of the reported research relied on the empirical comparison of how one dynamic parameter affects the quality of the surface texture of the component or on identifying some "optimum parameters" for a specific pulsed laser process [49] rather than providing a "universal" model, which is independent of specific pre-set conditions. Also, most research focuses on one pulse rather than tracks of pulses or even complex geometries.

One of the first models of pulsed laser cutting mainly focused on how to determine the quality of the cut rather than surface texture [50]. The model uses the oxygen reaction with molten metal to determine the quality measured in terms of the kerf

width. Although, this model is an interesting step, since it incorporates chemistry rather than relying on a relationship between fluence and crater depth, it is unable to predict the surface texture of the component after the pulsed laser cutting process or even complex geometries. Furthermore, the model is limited to maximum scan speeds of 900mm/min, which is a limiting factor.

The idea to capture one crater and overlay it to produce a surface texture could be considered a major step in modelling of craters with a focus on dynamic parameters [26]. The model uses a time modulation step function to place pulses onto a component, and uses a logarithmic relationship between fluence and ablated depth. However, the model uses a measured non-adaptable crater and hence cannot include changes due to focal depth or the gradient of the target surface.

Another topic of much research is the recast layer which is present in most PLA operations below certain threshold fluence. W. Chien found that assist gas pressure, peak power and focal length affect the recast layer thickness on INCONEL® 718 most [51]. The paper by C. Momma talks about the effect of pulse duration on solid targets [31]. Further studies found a relationship between the cavity size and the recast layer thickness [52]. Recast layer formation has also been related to the material used and the frequency of the pulse [35]. None of these studies offer a simplified relationship between kinematic/energetic parameters and fluence, and resultant workpiece topography.

From the literature, it becomes apparent that all existent models are either very basic or too specific and are not applicable to predict the surface texture. Due to the many influential factors which make up the surface texture a new or improved model is needed.

## 2.5 Nickel alloy inspection and analysis

### 2.5.1 Nickel sample preparation

Metallic samples which have been cut, polished and mounted can have their microstructures revealed by a process of chemical etching. This allows analysis of the materials microstructure within the bulk of the sample, or near a surface where damage or machining artefacts may be present. Samples that are polished will act as a mirror under optical microscopy, and as such details within the metal microstructure are lost. By use of chemical etchants, different material phases can be selectively attacked such that a microstructure is revealed [53]. This also allows for chemical analysis of the sample through the use of Scanning Electron Microscopes (SEMs) by phase identification of different crystalline grains revealed

through etching. The etchant selected for use on Nickel alloys is Kalling's No.2 reagent.

### 2.5.2 Scanning Electron Microscope Analysis

Scanning electron microscopy (SEM) analysis involves the use of an electron beam directed at a material sample, and determining information about the target material from the signals and emissions released by or from the target. The information contained in these signals can help describe the structure of the target, and its composition in terms of chemical elements. Each chemical element has a unique set of possible electron energies and as such has a detectable "signature" from electrons emitted from the target surface. Electrons detected from the target material can be of two principle origins.

- Secondary electrons – In simple terms, when target material atoms are energised by absorbing SEM beam electrons they can emit electrons from their own shells back towards the detector within the SEM. This is caused by inelastic scattering interactions between target atoms and beam electrons.
- Back-scattered electrons – In contrast to secondary (emitted) electrons, back scattered electrons are those which originate from the SEM beam itself. Heavier elements reflect these electrons more strongly, and as such chemical elements can be determined from apparent brightness of localised materials within the SEM image.

### 2.5.3 X-Ray Diffraction (XRD) measurements

Atomic structure and morphology of crystalline phases present in component materials can be evaluated using X-Ray Diffraction (XRD) [40]. Figure 20 shows a schematic of typical XRD analysis equipment.

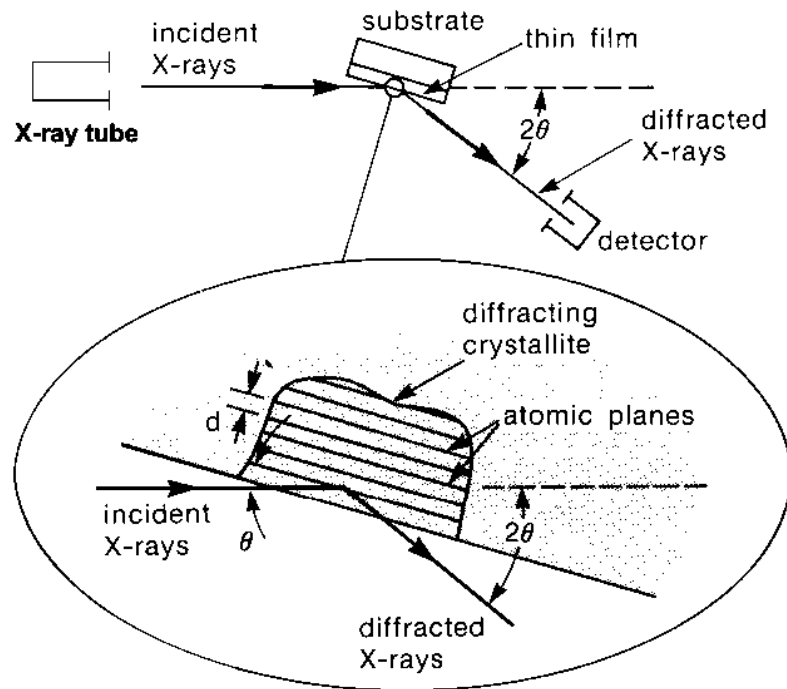


**Figure 20 - Basic Experimental Setup of X-Ray Diffraction analysis [54]**

XRD analysis has the capability to determine chemical information about the sample, through databases of typical atomic structures and inter-planar spacing, and hence X-Ray diffraction angles, found in known materials [13], [55]. Therefore, for this study, XRD can detect any presence of oxide phases in the processed material that may have weaker mechanical properties.

#### 2.5.3.1 Bragg's Law

The principle behind the operation of XRD is described by Bragg's Law. Bragg's Law is utilised to define the angle ( $2\theta$ ) at which X-rays diffract in crystalline materials such as metals and it is given by the equation  $n\lambda = 2d \sin \theta$ , "where  $n$  is an integer denoting the order of diffraction,  $\lambda$  is the x-ray wavelength of the x-rays,  $d$  is the inter-planar spacing of the crystal lattice, and  $\theta$  is the diffraction angle" [13]. The equation derived from Bragg's law manifests the correlation between  $\theta$  and  $d$ .

#### 2.5.3.2 Residual Stresses

Residual stress detection can be achieved using X-ray diffraction, which is a non-destructive method for on or near-surface stresses [12]. Samples need little to no preparation to be measured for stresses on or near the surface, however a degree of electrochemical polishing is required should stress measurements be required further into the material, typically beyond a few tens of microns into the material, which is of course a destructive measurement [12]. Understanding these residual stresses and the processing parameters which cause them is vital for process

optimisation, where component repair specifications are in place and validation is required [13]. Crack initiation commonly takes place on or near the surface of a serviceable component (i.e. without any major manufacturing defects such as large inclusions or metal lattice voids), and as such residual stress measurement on the surface of a component is necessary to ensure component integrity under high loading. Excessive tensile stresses at the surface of a component can cause cracking, and this may be exacerbated by additional tensile stresses induced by the processing of the material [13].

Stresses cannot be directly quantified from direct measurement of a material's microstructure. It is calculated from geometric measurements of the microstructure and material properties such as Young's Modulus and its Poisson Ratio. Geometric measurements are made to determine any elastic strain that may be present in the microstructure between material crystal lattice planes. Elastic strains are calculated from measured deformations and distortions in the crystal lattice, which manifest through varying spacing between crystalline lattice layers ( $d$ ), and hence angular diffractions ( $\theta$ ) of X-rays according to Bragg's Law [56].

In Nickel-based alloys 50% of measurement X-rays are diffracted at a crystalline layer approximately  $5\mu\text{m}$  from the material surface [13]. Machined specimens to be evaluated by XRD must be stored and handled extremely carefully to prevent altering the residual stresses through any mechanical influences it could be exposed to. Figure 21 further illustrates the concept behind residual stress measurement using XRD.

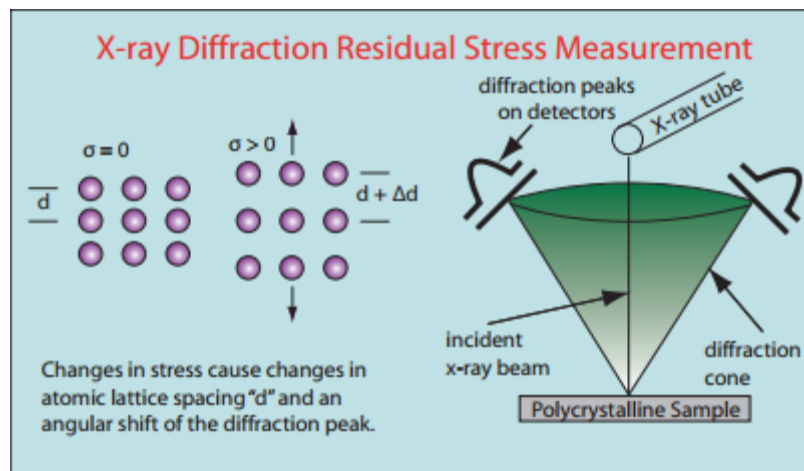


Figure 21 - Diagram to Illustrate Residual Stress Measurement [57]

# Chapter 3. Experimental Methodology and Equipment

This chapter describes the main equipment and methodologies used throughout this project. Where minor, one-off experimental operations are carried out they are described in the relevant section of the chapter concerning that phase of experimentation.

## 3.1 Pulse Laser Ablation (PLA)

Pulsed laser ablation was carried out using an SPI redENERGY G3.0 pulse Yb:YAG laser source, transmitted across an optical bench through a beam aperture with an expanded beam diameter of 2mm, a series of mirrors and an X/Y galvanometer scanner. The galvanometer scanner system incorporated an f-theta objective with a 163mm focal length, resulting in a planar scan field of approximately 100x100mm at the focal plane of the laser beam. The theoretical focused spot size was  $39.5 \mu\text{m}$ , with a beam quality of  $M^2 = 1.8$ , resulting in a measured  $D4\sigma$  spot size of approximately  $71\mu\text{m}$ . The laser source had a maximum power output of 20W, with a 200ns pulse duration. Pulse energy was attenuated at pulse frequencies below 25kHz (35kHz for the SPI redENERGY G3.1 laser source that was used for additional trials) to prevent damage to optical systems. All optical components were bolted to a pneumatically supported optical bench to minimise variations in beam guidance and placement due to vibrations. This set up is shown below in Figure 22.

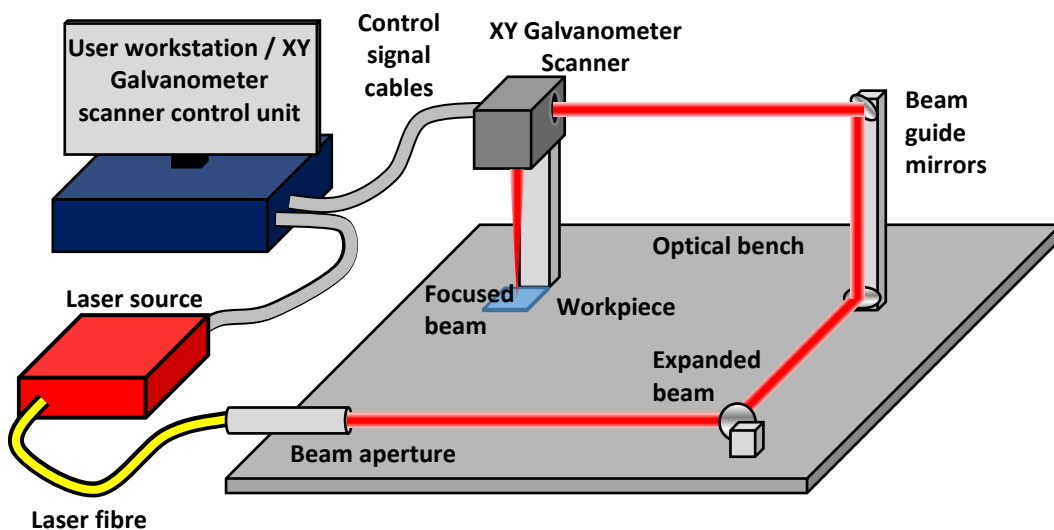


Figure 22 - Optical bench set up with laser source and X/Y galvanometer scan unit control

During ablation, samples were oriented such that the target surface was normal to the laser beam, and adjusted in height to ensure the laser beam was focused upon the target surface. No shield gas was used, as it was important to reflect conditions that would likely occur during the operation of repair equipment on components that remained on-wing and in-situ.

The laser source had a peak emission wavelength of 1064nm, ideal for processing nickel targets due to their high absorption of photons at this frequency.

## 3.2 Sample Cutting, Mounting, Polishing and Etching

Ablated samples were analysed using a range of techniques, including optical and electron microscopy. To carry out these analyses, samples had to be prepared in a way to enable data capture from the measurement equipment. Analysis of ablated sample microstructure carried out on SEM equipment required a series of preparation steps to reveal the sub-surface microstructure, as described in the following sub-sections.

### 3.2.1 Sample Cutting

Samples were cut across the middle of each ablated area, such that any non-steady-state phenomena from beam kinematics (beam acceleration etc.) would not be present in the area of material being analysed. Cutting was performed using an Accustom-5 Diamond cutter. A section through the ablated surface was cut, as shown in Figure 23

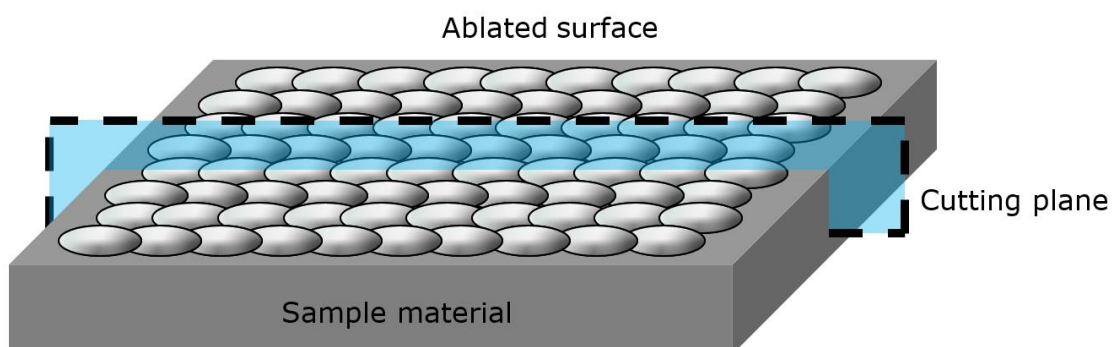


**Figure 23 - Cutting plane through ablated samples**

### 3.2.2 Resin Mounting

A Metaserv automatic mounting press was used for sample holding. Samples were supported with plastic or metal clips and buried in a conductive thermoplastic granular powder (Conducto-Mount Phenolic Mounting Resin). Mounted samples

were then extracted in 30mm diameter blocks, approximately 10mm in height, as shown in Figure 24.

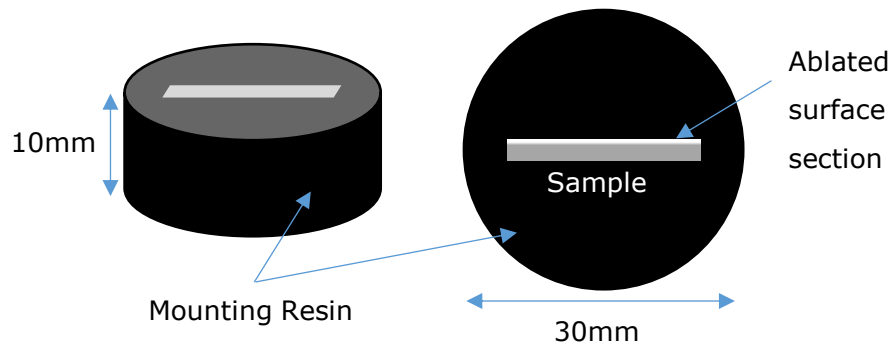


**Figure 24 - Sample mounting in conductive resin for analysis**

### 3.2.3 Abrasive Polishing

Mounted samples were then ground and polished to reveal the cut material surface, and to create a flat plane for inspection of the material substructure. Grinding and polishing wheels of progressively finer grits were used (Labopol-21 P240 grit @ 58.5 $\mu$ m down to 1 $\mu$ m diamond impregnated cloth wheels).

### 3.2.4 Chemical Etching

To reveal sample microstructure, chemical etching was used to selectively attack different material phases, revealing grain facets and boundaries [35]. The chemical reagent used in the sample preparation was as Kalling's No. 2 as it is ideal for revealing the microstructure of nickel alloys. This reagent has a composition of 2 grams of Copper Chloride, 40ml of hydrochloric acid and 40-80 ml of ethanol.

## 3.3 Topographical surface measurement

In cases where 3D profiles of ablated surfaces - either single craters or tracks of craters, were required for process characterisation - were required, white light interferometry was performed with a Bruker Contour GT using white light illumination. Sample surfaces were oriented such that they were normal to the measurement apparatus through alignment and expansion of light fringes reflecting off the sample surfaces. Sensor heights were determined by adjusting elevation above the sample such that the sample surface was fully out of focus at both extremes of the height adjustment. A range of magnification objectives from 2.5x to 20x was used. Data filtering of the measurements was carried out using a range of high, low, and band pass gaussian cut-off values. When data acquisition was not sufficient after one single measurement, multiple measurements (between 3 and 10) were taken and averaged.

### 3.4 Scanning Electron Microscopy

Microstructural and micro-scale ablated surface analysis was performed using a Philips XL30 FEG-SEM, with an integrated XYZ stage in the sample chamber, with tilt and rotation controls, as shown in Figure 25 - Philips XL30 FEG-SEM.

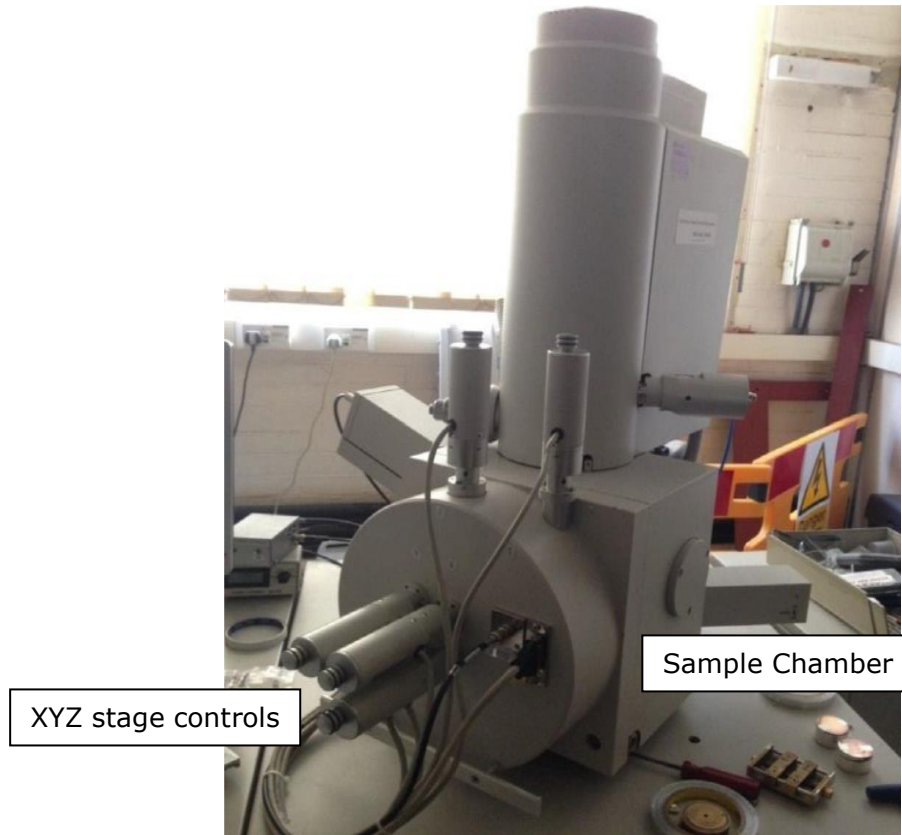


**Figure 25 - Philips XL30 FEG-SEM**

Beam acceleration voltage was set between 10 and 20kV, with a beam spot size of 3-5 $\mu$ m dependent on whether secondary electron (SE) or back-scattered electron (BSE) measurement was being used. A working distance of approximately 10mm was used.

# Chapter 4. Metallurgical changes in laser machined INCONEL<sup>®</sup> 718

## 4.1 Metallurgical requirements from Rolls-Royce

As with any machining process in which there is significant thermal input to a metallic workpiece, there will be a risk of metallurgical change within the material being machined. A range of thermally driven chemical and morphological changes must be understood and their likelihoods considered. Before defining laser repair schemes, preliminary work must be undertaken to assess a chosen laser system against target material. This feasibility study includes studying the laser-material interactions, and the metallurgical changes it will induce in the component. It will also describe material removal rates on the target material as a function of key process variables – laser power, pulse frequency and laser scan speed.

Rolls-Royce surface standard CME5033/5/E1 [1] describes a range of laser processes on different materials. The work carried out in this thesis falls under a category where the laser processing is used to create a finished repair geometry (i.e. not net shape or requiring further processing) and any recast material is not removed. Additionally, no active assist or shield gas is used in this category. INCONEL<sup>®</sup> 718 sheet (0.6mm thick) is used as a baseline test material for this section of the study.

### 4.1.1 Chemical and microstructural analysis techniques

There are a range of investigative methods available for both surface and sub-surface evaluation of material integrity after laser processing. Past approaches have commonly included analysis of strains through residual stress measurements. These changes have been caused by effects such as recrystallization and grain size alteration and phase change/formation of carbide and oxide phases which may make surface material more brittle, leading to degradation of mechanical properties and fatigue performance [58][59].

## 4.2 Methodology for assessing metallurgical impact of laser machining

### 4.2.1 Sample Preparation for machining and inspection

Samples were prepared for machining under pulsed laser ablation, and these samples were then analysed using a range of techniques. X-Ray diffraction was used to measure residual stresses and identify different phases within the material.

SEM analysis was used to measure chemical constituents, and qualitatively measure the samples for identification of different material phases. 3D profilometers were also used to measure ablated surface roughness.

#### 4.2.1.1 Laser Ablation sample preparation

The main objective of the work in this report is to investigate the effect of 3 laser parameters (power, frequency and scan speed) on the nickel-based superalloy (INCONEL® 718) used to make compressor blades, and optimise them to effectively get a range or combination of these 3 parameters that will induce the least negative effects when using pulsed laser ablation. The objectives of this chapter are summarised below.

- To investigate some of the metallurgical and microstructural transformations that could occur in nickel-based alloys (INCONEL® 718, NIMONIC® 105) after performing laser machining and processing using nanosecond pulsed laser ablation, during repair of the compressor blades.
- To investigate the pulsed laser ablation process to establish an optimal set of parameters that can be used to repair the target component with an efficient material removal rate whilst preserving surface quality and microstructural integrity.

A full factorial design of experiments (DoE) approach was used with the 3 main laser processing parameters (factors); average power output, pulse repetition frequency and laser scan speed, shown in Table 2. Pulse duration was set at 200 nanoseconds. Each factor was set at 3 levels, covering a range of material removal rates. Combinations of factor-pairs were considered to compare process characteristics such as ablation crater offset distances (scan speed and repetition frequency) and pulse energies (power output and repetition frequency). Average power output was varied as an input value to laser programming software, Nutfield Waverunner, rather than a measured output power.

<b>Table 2 - Full factorial experiment design</b>			
<b>Factor</b>	<b>Levels</b>	<b>Values</b>	<b>Units</b>
<b>Average power output</b>	3	10,15,20	Watts
<b>Pulse repetition frequency</b>	3	25,50,75	kHz
<b>Laser scan speed</b>	3	400,800,1200	mm/s

These combinations of factors resulted in a range of fluences being used to ablate the material. Fluence is defined as energy per area, for one pulse;

$$\Phi = \frac{8P}{\pi f \varphi^2} \quad (3.1)$$

where;

$\Phi$  = Fluence (J/m<sup>2</sup>) \*

P = Average power output (W)

f = Pulse repetition frequency (Hz)

$\varphi$  = Laser beam spot diameter (m)

\*It should be noted that laser fluence  $\Phi$  is commonly expressed in units of J/cm<sup>2</sup> rather than J/m<sup>2</sup>.

Samples of INCONEL<sup>®</sup> 718 sheet were used as shown in Figure 26a. 9 parameter sets were generated per sample, and each sample was conducted with one of the 3 factor levels for power output. This resulted in 3 samples, containing 27 unique factor/level combinations of power output, scan speed, and pulse repetition frequency. An additional parameter, scan track offset distance was varied to match

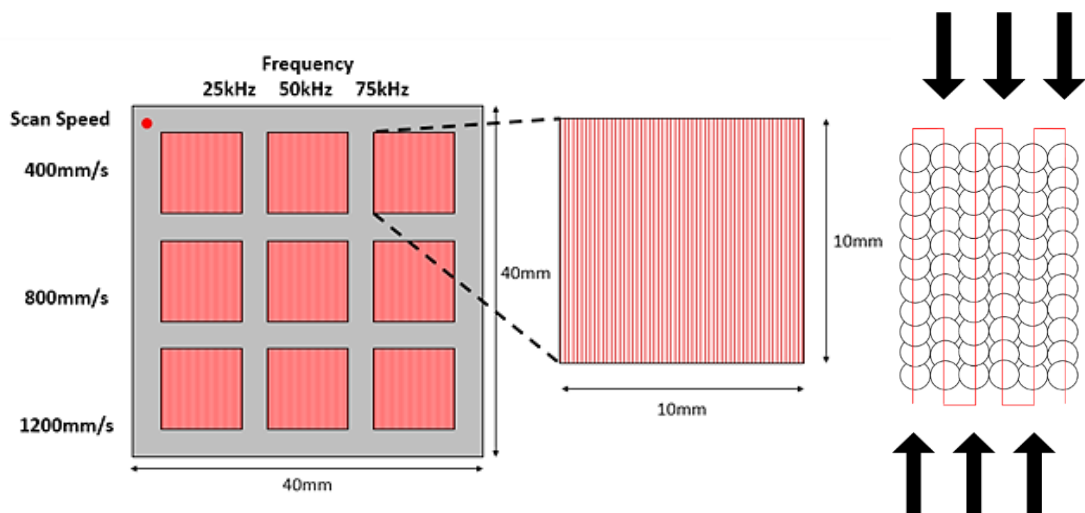


**Figure 26 - a) Experimental sample layout, b) Pulse scanning direction and track offsetting**

crater offset distances, resulting in a 'square' matrix of craters (shown in Figure 26b). This resulted in a consistent overlap between pulses in both the X and Y direction and was done to ensure uniform results within the surface of the sample in both X and Y directions.

The levels chosen for each of these parameters were determined from the operational ranges of both the laser system, and the optical scanning equipment intended for use in the In-Situ deployment of these repairs as described previously. Laser scan speed was chosen to fall within the range of speeds achievable by the optical equipment intended for In-Situ repairs. Values for laser pulse frequency were chosen to ensure material removal at the highest values, and maintaining un-attenuated laser power output (due to laser safety features of the SPI G3.0 system) at the lowest values. Power values were set to ensure material removal at the lowest resulting pulse energies (as a combination of lowest laser power output and highest pulse frequency), and maximum available power output from the laser system for the highest value. From these samples, optimal parameter sets were identified in accordance to the stated aims and objectives.

The laser power was selected as the parameter to remain constant on each INCONEL<sup>®</sup> 718 sample because the laser modulates better and responds more readily to quick changes in frequency and scan than it does to quick changes in power. Therefore, the laser would operate more accurately and effectively if the power was kept constant over each sample. The laser beam spot size  $\varphi$  (at focus) that was used was calculated from the theoretical beam radius for the given laser wavelength and optical systems used to deliver the beam ( $71.1\mu\text{m}$ ). The spot offset (distance between the centres of consecutive pulses) had to be set equal to the track offset in the scanning direction, for each  $10 \times 10$  mm parameter set.

Only one pass of the laser beam was done for each square pattern, i.e. no repeated scanning of the trial squares, and laser ablation was carried out in normal air conditions (assuming 78% nitrogen, 21% oxygen, 1% other).

#### 4.2.2 Measurement of samples using XRD (X-Ray Diffraction) for residual stresses and chemical constituents

Before samples were analysed, they had to be mounted in putty to align with the mechanical axis/plane of rotation. If there is significant misalignment in this respect the measurements will be inaccurate as they are taken through a geometrical method. All of the various crystalline phases present in the processed material will have unique characteristic peaks in the spectra of diffracted X-rays. These peaks relate to the atomic spacing in the crystalline structure.

##### 4.2.2.1 Residual Stress Measurement

For measurement of residual stresses, no special sample preparation was required. The equipment used was a Bruker-AXS D8 Advance, with the following configuration: Copper x-ray tube at 40kV and 30mA, Nickel filter for Cu K $\alpha$  x-rays,

a focusing polycapillary with 1.0 mm diameter near-sample aperture, a motorised Eulerian cradle sample stage, 1.0 mm anti-scattering and detector slits, scintillation counter x-ray detector. Bruker-AXS DIFFRAC plus software was used to operate the diffractometer and analyse the results.

The sample was mounted on a stage and levelled built into the machine; x, y & z positions for each sample area were ascertained; a suitable diffraction peak was chosen and scanned to ascertain the 2theta range to scan; the residual stress scans were set up for seven tilt angles and two angles within the sample surface plane. To calculate stresses in the material using elastic strain measured by the XRD analysis, the Young's Modulus and Poisson Ratio for INCONEL® 718 were required. These are used to calculate x-ray elastic constants, which were then used to determine and measure the strain components from which the residual stresses were derived. All calculations were performed by the Bruker-AXS DIFFRAC plus software used to operate the XRD machine. The following values for INCONEL® 718, taken from the software manual, were used:

Young's Modulus = 205 GPa

Poisson's Ratio = 0.29

Both normal and shear stresses were measured in the ablated samples. The directions upon which these stresses act are shown in Figure 27.

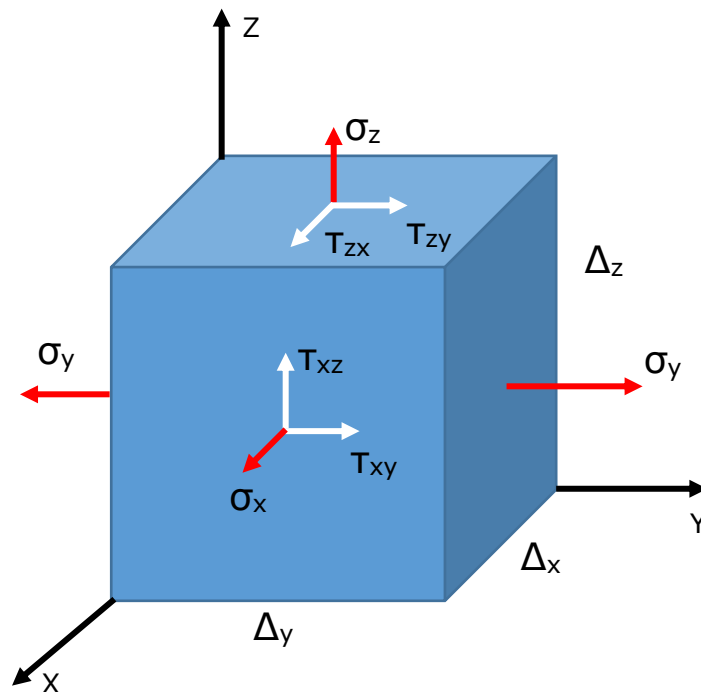


**Figure 27 - Normal and shear stresses acting upon a cubic element within a component.**

X,Y,Z = Principle axes

$\Delta_{x,y,z}$  = Change in element dimensions

$\sigma_{x,y,z}$  = Normal stress in directions x, y, z

$\tau_{AB}$  = Shear stress on a plane perpendicular to an axis A in the direction of an axis B

#### 4.2.2.2 Material Phase Analysis

The varying elemental and oxide phase constituents in the resultant ablated surfaces were analysed using the same XRD equipment as used for residual stresses. By obtaining diffracted X-Ray spectra from the sample, peaks within a spectrum can be used to identify different elements or compounds by their unique  $2\theta$  diffraction angles. High counts of x-rays diffracted at any given angle  $2\theta$  indicate an atomic or molecular structure specific to a known element or compound.

#### 4.2.3 Surface Roughness Evaluation

Surface roughness was evaluated using Fogale Photomap 3D, a full field white-light interferometric 3D surface profiler. An example of the 3-dimensional representations of each surface can be seen in Figure 28.

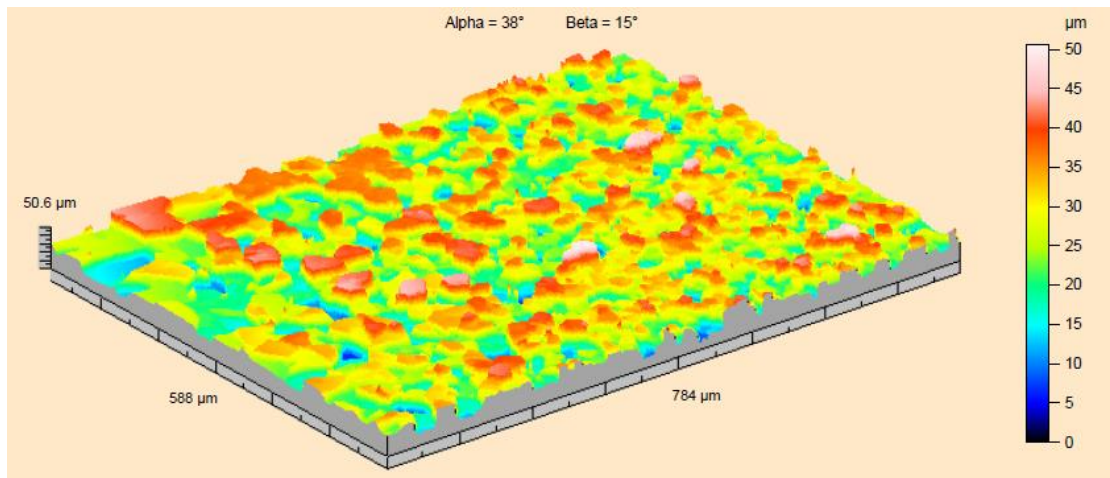


**Figure 28 - Example 3D surface measurement of sample ablated surface using white-light interferometry**

Surface roughness ( $R_a$ ) values were calculated in MountainsMap software from the 3D surface measurements, using cut-off filter and evaluation lengths automatically determined by the surface analysis software in accordance with ISO 4288. These  $R_a$  values were then compared against each other, and the laser operating parameters used to create them, to determine a relationship between process input and material roughness output.

## 4.2.4 Scanning Electron Microscopy (SEM) Analysis

### 4.2.4.1 Microstructural Analysis using SEM

Samples were then mounted on a XYZ stage in a Philips XL30 FEG-SEM. The system was closed, the required vacuum created and the working distance set at approximately 11mm. Electron beam size was  $3\mu\text{m}$  with an accelerating voltage between 10-20kV. An image of the mounted samples in the FEG-SEM is also provided in Figure 29 below.

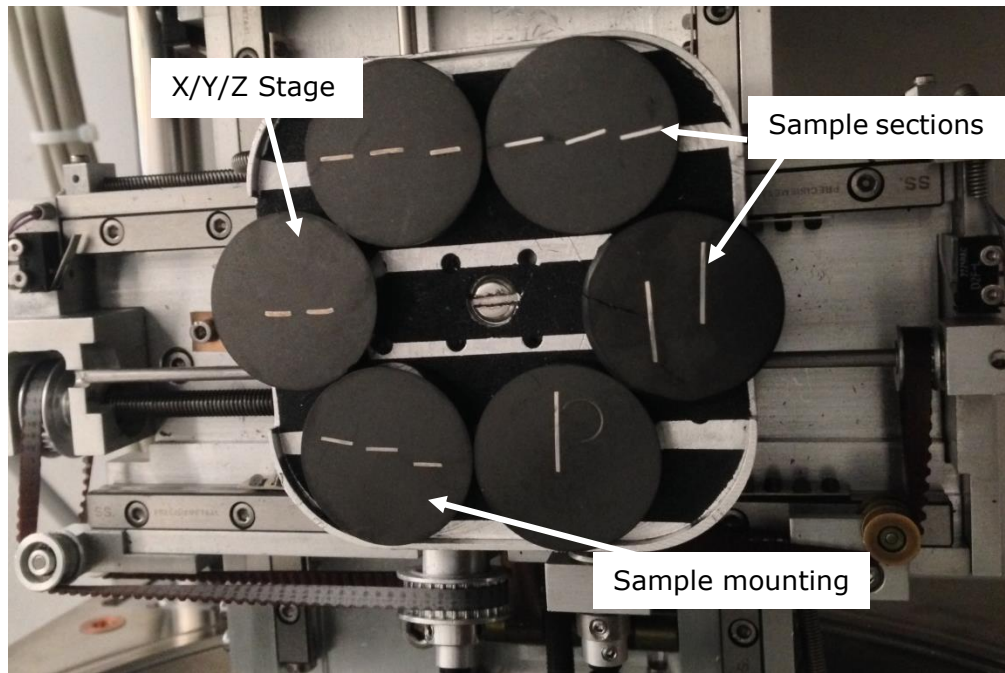


**Figure 29 - Prepared Samples Mounted on XYZ Stage in FEG-SEM**

### 4.2.4.2 Chemical Analysis using SEM

Chemical analysis was performed by the same SEM equipment used in the previous section. By computer analysis of X-Ray spectra emitted from the sample, unique chemical elements can be identified. Scans of each sample were carried out anywhere from 30 seconds to 5 minutes, until sufficient chemical data was acquired to give a detailed map of elements within the sample. These 2D scans of samples are referred to as "hypermaps". If traces of any oxide were indicated by the hypermaps, a line scan could then be performed to quantify the amount of oxide present in terms of percentage mass. The line scans were taken through the 'worst' looking regions of the sample cross-sections, for instance, where the recast layer appeared thickest.

### 4.3 Results and Discussion

#### 4.3.1 Results for Surface Roughness Evaluation

Table 3 below contains the Ra values (in  $\mu\text{m}$ ) for the surface roughness measurements carried out on each ablated pattern with the Fogale measurement equipment.

**Table 3 - Surface roughness measurements (in  $\mu\text{m}$ ) for all samples ablated at 10, 15 and 20W**

		Power (W)		
		10	15	20
Scan Speed (mm/s)	Frequency (kHz)	Average Surface Roughness ( $\mu\text{m}$ )		
400	25	0.44	1.01	1.62
400	50	0.90	2.79	3.71
400	75	0.30	1.61	1.20
800	25	1.42	1.04	*
800	50	0.88	1.22	1.40
800	75	0.90	2.19	1.27
1200	25	1.00	0.60	2.86
1200	50	1.00	0.94	1.50
1200	75	0.42	1.00	1.06

\* Some sample surfaces were damaged and rendered un-measurable by the equipment available, and as such missing data points are indicated with an asterisk.

From the values shown in Table 3, average roughness values for each level of the three process factors (power, scan speed, frequency) were calculated and these are shown in Figure 30. Values for each of the factor levels are shown previously in Table 2. From the figure below there is a clear positive correlation between surface roughness and laser power output. However, given the large variations in surface roughness measurements for both varied scan speeds and frequencies, no clear trend can be identified.

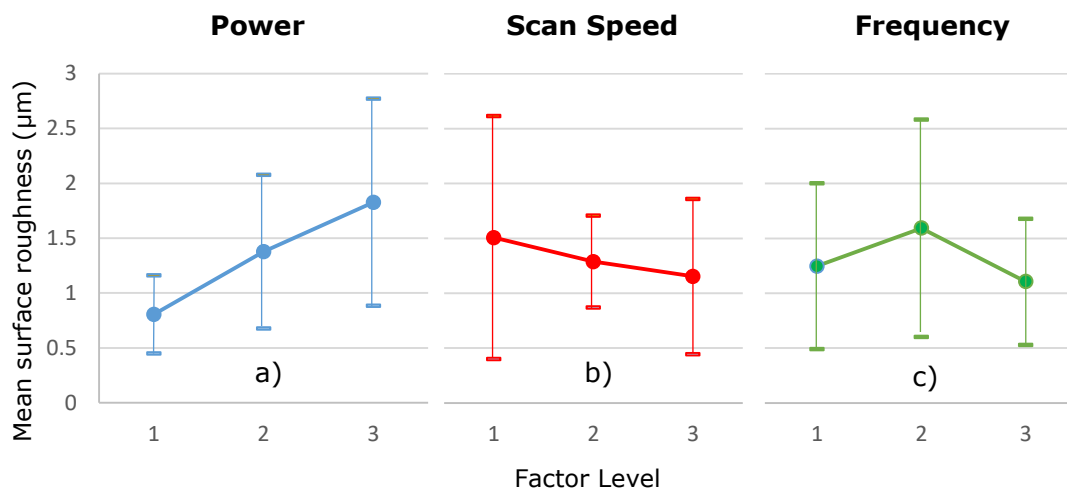


**Figure 30 - Mean surface roughness with standard deviation for each level of process variables a) Power, b) Scan speed, c) Frequency**

It was found that out of the surface roughness values obtained for samples with reasonable levels of recast (<15µm continuous thickness), none were excessive. The sample ablated at 20W, 400mm/s and 50kHz had the highest surface roughness. It is clear from the top-down SEM image of this sample (Figure 39b) that the observed topography will result in a high surface roughness. In addition, the surface roughness could be higher than stated in Table 3 due to the irregularity of the structures seen, and as such choosing a different frequency/wavelength of measurement may result in a higher roughness. Error bars on Figure 30 show large variations in measurements for roughness, due to interactions between secondary factors, i.e. secondary factors of scan speed and frequency when considering the effect of power shown in Figure 30a. As such, the effect that factors have on the resulting surface roughness are difficult to identify, other than the clear positive relationship between surface roughness and power.

#### 4.3.1.1 Residual Stress Measurement

The diagram in Figure 31 can be used to show which ablated square each row of obtained values relates to, with respect to the frequency and scan speed parameters. It also depicts the directions of 2 principal axes in which the residual stress measurements were taken.

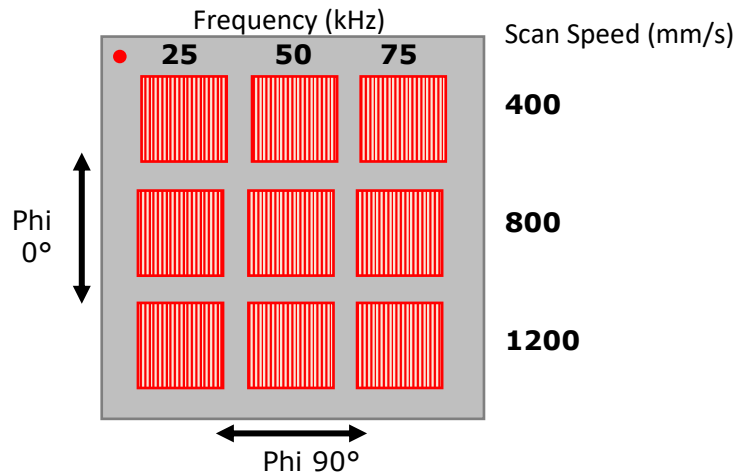


**Figure 31 - Schematic to Show the Principal Axes in which the Residual Stress Measurements were taken**

The Poisson Ratio and Young's Modulus of a material are required to calculate residual stresses as they help to incorporate factors such as the elastic anisotropy of the crystal lattices being evaluated, thus, minimising the error in the derived values and improving the reliability of the computations. The isotropic x-ray elastic constants (XECs) are calculated using the following equations [60]:

$$s_1 = -\frac{\nu}{E} \quad (3.2)$$

$$\frac{1}{2}s_2 = \frac{\nu+1}{E} \quad (3.3)$$

Where,

$\nu$  = Poisson's Ratio

$E$  = Young's Modulus

Results were recorded for all normal ( $\sigma$ ) and shear ( $\tau$ ) stresses in the Phi 0 and Phi 90 directions shown on Figure 31. Both linear and elliptical fits were applied to the data. The measurements are presented in Table 4 as mean stresses across the entire ablated square, with ranges ( $\pm$ ) of stress observed above and below the mean included.

**Table 4 - Normal and shear stress measurements for all samples**

Sample No.	Power (W)	Frequency (kHz)	Scan Speed (mm/s)	Pulse Energy (mJ)	Phi 0						Phi 90					
					Linear Fit		Elliptical Fit				Linear Fit		Elliptical Fit			
					$\sigma_0$ (Mpa)	+/-	$\sigma_0$ (Mpa)	+/-	$T_0$	+/-	$\sigma_{90}$	+/-	$\sigma_{90}$	+/-	$T_{90}$ (Mpa)	+/-
1	10	25	400	0.40	486	20	486	40	23	30	452	69	536	43	-65	33
2	10	50	400	0.20	860	26	899	70	-33	53	496	31	449	43	51	33
3	10	75	400	0.13	693	22	680	57	15	43	800	77	901	72	-104	55
4	10	25	800	0.40	475	26	456	40	24	31	420	63	492	37	-74	28
5	10	50	800	0.17	418	31	389	36	29	28	359	26	386	31	-31	24
6	10	75	800	0.13	568	38	503	47	74	35	536	73	628	48	-81	36
7	10	25	1200	0.40	396	33	341	32	59	24	411	33	428	38	-14	29
8	10	50	1200	0.20	483	31	482	39	11	30	471	52	562	39	-94	30
9	10	75	1200	0.13	479	20	459	40	19	30	465	70	523	41	-64	31
10	15	25	400	0.60	594	35	541	49	55	37	521	42	499	48	24	36
11	15	50	400	0.30	301	33	245	27	65	21	156	31	93	14	68	10
12	15	75	400	0.20	381	27	343	32	41	24	387	36	341	33	50	25
13	15	25	800	0.60	493	21	501	42	-4	32	472	53	514	42	-32	32
14	15	50	800	0.25	603	29	580	49	24	37	371	42	309	34	70	26
15	15	75	800	0.20	823	29	867	66	-41	50	513	19	522	43	0	33
16	15	25	1200	0.60	492	27	491	39	8	30	412	32	408	36	5	28
17	15	50	1200	0.30	565	24	573	48	2	36	457	54	540	40	-76	31
18	15	75	1200	0.20	556	38	490	47	79	36	473	43	497	42	-25	32
19	20	25	400	0.80	328	19	301	26	30	20	161	20	137	15	25	11
20	20	50	400	0.40	-17	32	-34	6	18	4	97	23	88	19	13	7
21	20	75	400	0.27	219	20	202	20	23	15	302	34	356	27	-46	21
22	20	25	800	0.80	Sample damaged and rendered unmeasurable											
23	20	50	800	0.33	320	26	343	26	-4	20	169	24	128	14	38	11
24	20	75	800	0.27	372	16	408	31	-29	23	187	41	194	17	-4	13
25	20	25	1200	0.80	13	25	-27	5	47	4	63	19	49	8	14	6
26	20	50	1200	0.40	391	9	386	33	10	25	180	33	165	19	38	14
27	20	75	1200	0.27	448	23	465	36	-15	28	245	18	238	18	6	14

From the results shown in Table 4, it is clear that there is some error present when measuring samples ablated at 20W (sample numbers 19-27). The samples in this subset displayed very large variations in normal stresses from both linear and elliptical fits of data, in the Phi 0 and Phi 90 directions. Moreover, the stresses measured on these samples were so close to zero that in some cases a negative stress was measured indicating compressive stress where tensile stresses are found in other samples. The most likely explanation for this behaviour in the data for samples ablated in 20W is the irregularity of the surfaces of these samples, some examples of which are shown in section 4.3.2. These readings are seen as anomalous because there is no clear trend with the KPV values and the stress measurements. An additional anomalous was observed for sample number 11 in the phi 90 normal stress measurements, with stress values much lower than the other samples ablated at 15W (samples 10-18). It should also be noted that the Phi 0 stress measurements for this same sample displayed the lowest normal stresses of all samples ablated at 15W. Upon inspection of this sample under SEM, it is clear that there is a similar reason for the anomalous reading to the samples ablated at 20W; the irregularity of the ablated surface. A cross section for the sample ablated at 15W, 50kHz and 400mm/s is shown below in Figure 32.

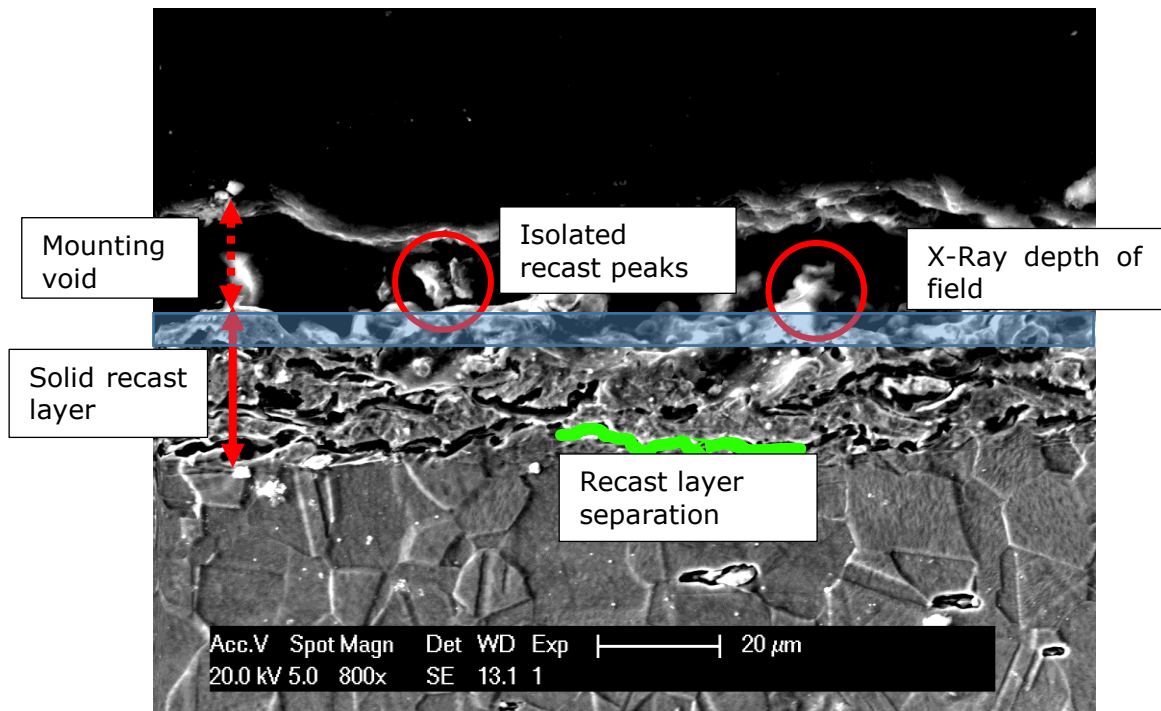


**Figure 32 - SEM Cross section of sample ablated at 15W, 50kHz, 400mm/s**

The red arrow indicates the layer of solid 'recast' material, between 20-25 $\mu$ m thick across the entire sample surface. The red dotted arrow indicates an additional 10-20 $\mu$ m thick layer where isolated metallic structures (circled in red) could be found, which have inhibited mounting material from forming a flat interface against the

solid recast layer. The area underneath this recast layer is the parent material. It has an unchanged microstructure from the boundary between it and the recast layer (green line), and the microstructure further into the sample.

Shown as a blue band across the image is the approximate depth of field for data acquisition through X-Ray diffraction. Throughout this band there are areas where recast material is present, and voids in the recast topography. As such, there will be no consistent measurement of the sample across the entire ablated area.

Of the sample sets where lower surface undulation was observed, consistent readings were taken. When comparing these observations against surface roughness measurements in Table 3 it is apparent that samples with lower surface roughness produced consistent results. It should be noted that the sample in Figure 32 had the highest surface roughness of the all samples ablated at 15W, at  $2.79\mu\text{m}$ . Similar behaviour was seen in the samples ablated at 20W, where there is high surface roughness ( $1.06 - 3.71\mu\text{m}$ ) and as such stress values for these samples may be unreliable.

Maximum and minimum stresses in both the Phi 0 and Phi 90 directions are highlighted in Table 4 and it is clear that samples which showed the maximum stress in the Phi 0 direction are not necessarily the same samples with maximum stresses in the Phi 90 direction. Two examples of this can be seen in the set of samples ablated at 10W, which show the highest stresses out of all ablated samples. Figure 33 shows these surfaces, ablated with process parameters of  $P=10\text{W}$  and  $v_f=400\text{mm/s}$  at  $f=50\text{kHz}$  and  $f=75\text{kHz}$ .

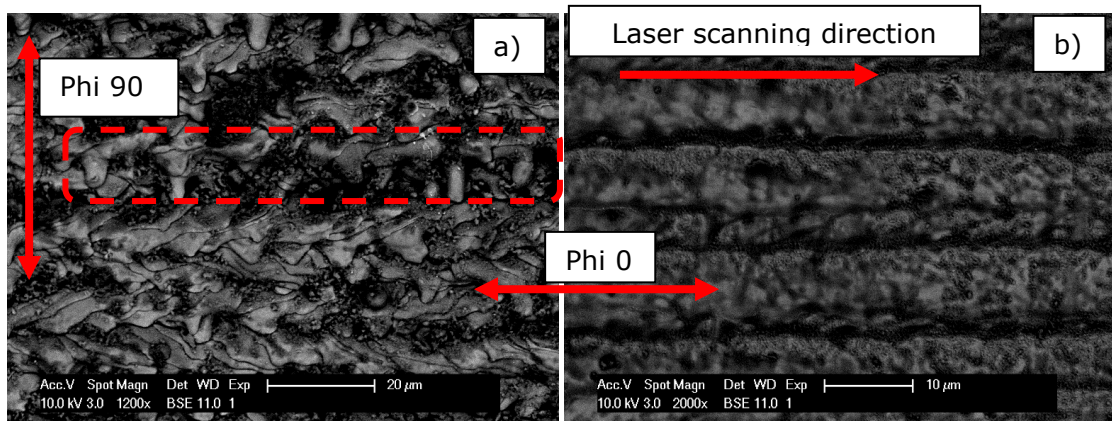


**Figure 33 - Top-down surface quality of samples ablated at a) 10W, 50kHz, 400mm/s b) 10W, 75kHz, 400mm/s**

Both of these surfaces show directional topographies, namely “tracks” running from left to right in the direction of laser scanning. The topography in Figure 33a is less apparent, however there are still defined “edges” to the laser scan tracks where multiple recast features have settled on top of one another. One of these tracks is

circled in a dotted red line. The measurement directions Phi 0 and Phi 90 are marked on the image. These samples showed normal stresses in both Phi 0 and Phi 90 directions ( $\sigma_0$ ,  $\sigma_{90}$ ) which were above average for samples ablated at 10W. The sample in Figure 33a displayed the highest  $\sigma_0$  value and Figure 33b had the highest  $\sigma_{90}$  value, of both the 10W subset and the entire sample set. It should be noted that the sample in Figure 33b also displayed the 2<sup>nd</sup> highest  $\sigma_0$  value in the 10W subset, the 3<sup>rd</sup> highest from the entire sample set, and the highest average of normal stresses  $\sigma_0$  and  $\sigma_{90}$  from the entire sample set. As such it can be stated with some confidence that those samples which show directional topographies display higher normal stresses than average.

All the shear stresses induced on the samples are very small, and in many cases the variation seen in these measurements is larger than the mean of the measurements. As such, all shear stress results are ignored when considering the residual stress effects of laser ablation.

#### 4.3.1.2 Chemical Analysis of XRD data

From analysis of the graphical data obtained from the XRD scan there was little indication for the presence of oxides. The majority of analyses showed peaks from metallic elements used in INCONEL<sup>®</sup> 718, and there were no significant oxide phases detected. Where trace oxide phases were detected, they were very small and isolated which would indicate a very low concentration within the volume scanned. Few samples showed any large enough instances of oxidation to raise concern. Two of the samples where trace oxide phases were found were those with the surfaces ablated at a power of 20W, a scan speed of 400mm/s and frequencies of 25 & 50kHz. The samples where isolated oxide phases were found were all ablated at high powers and low frequencies, indicating that oxide generation is closely related to pulse energy. This is likely due to the elevated local material temperatures required to achieve oxidation, as more material will reach this oxidation temperature with higher energy inputs, i.e. as thermal energy per unit volume increases, oxide formation becomes easier.

Figure 34 shows XRD chemical analysis for the identification of different element and compound phases for the sample ablated at 20W, 400mm/s and 50kHz. As seen in the figure, two prominent peaks are identified for pure nickel phases, indicated with red markers.

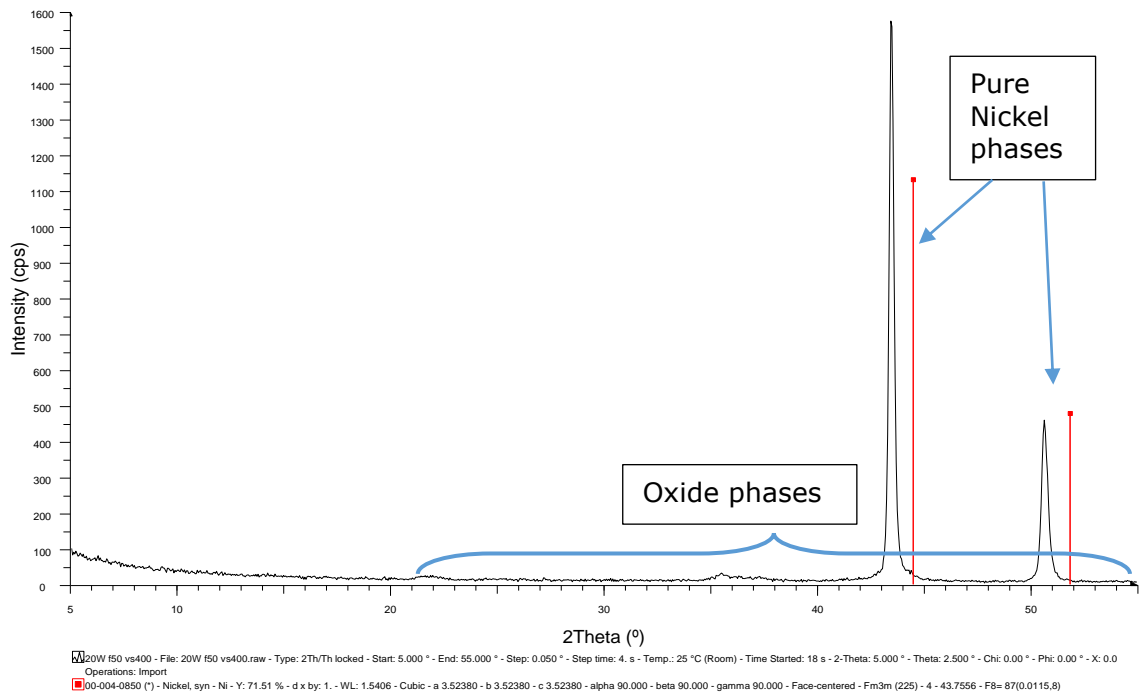


**Figure 34 - XRD Spectrum for Identification of Nickel Oxide in sample ablated at 20W, 400mm/s, 50kHz**

Figure 35 shows XRD spectra from the sample ablated at 20W, 400mm/s and 50kHz (the same sample as shown in Figure 34) scaled such that oxide phase detection can be seen. It is clearly shown that the largest peaks in the spectra are linked to nickel (500-1600 cps detection rate). The most prominent oxide phases found were those of magnetite ( $\text{Fe}_3\text{O}_4$ ) and Bunsenite ( $\text{NiO}$ ) which are circled in red in the figure, up to 20cps detection rate. Smaller rates of detection were present for other oxide phases, including oxides of Chromium ( $\text{Cr}_2\text{O}_3$ ) and another form of Iron Oxide, Hematite ( $\text{Fe}_2\text{O}_3$ ). With oxide phase detection rates ranging from 1.25-4% for that of pure nickel detection, there does not appear to be significant oxide generation at, or near, the ablated surface. Further validation of this assumption can be gained through energy-dispersive X-ray (EDX) analysis, detailed in the following sections. From depths of recast measured through SEM analysis, the volume of oxidation observed within the recast layer falls well within acceptance limits.

If the ablation was carried out in a vacuum or with an inert shield as atmosphere, it would be expected to see even lower levels of oxide present in the samples, if any. It is worth noting that due to the rough nature of some of the samples and the requirement for measurement surfaces on the sample to be relatively flat, there may be some loss of data in oxide detection. Additionally, with a penetration depth of several micron, it is possible that only parent material is being measured and any surface oxide is being bypassed in the measurement process. Whilst this is not ideal for a full quantitative analysis of the samples, it does indicate that if there are

any significant oxide phases present, they will not be present beyond the first few micron of material given the detection depth of X-Ray diffraction.

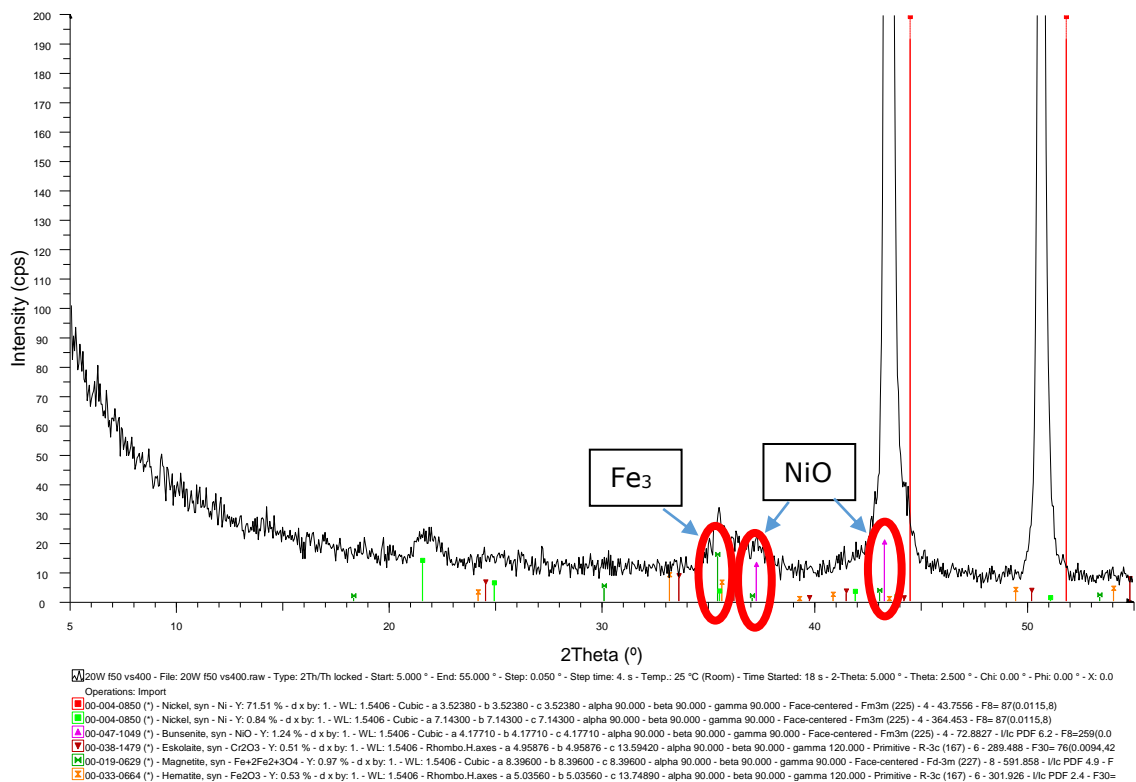


**Figure 35 - XRD Spectrum for Identification of Oxides and other Metallic Elements in Sample ablated at 20W, 400mm/s, 50kHz**

## 4.3.2 SEM measurement results

### 4.3.2.1 Qualitative Analysis

Ablated surfaces were initially qualitatively assessed, to narrow down parameter sets which resulted in 'good' surface finishes. Minimal visible recast and flat/smooth features were indicators of these ideal surface finishes. Figure 36 shows an example of one of these surfaces, where there is a visibly low level of recast around pulse crater edges (circled in dotted red, with solid red for the crater segment) and a regular, smooth pattern is apparent.

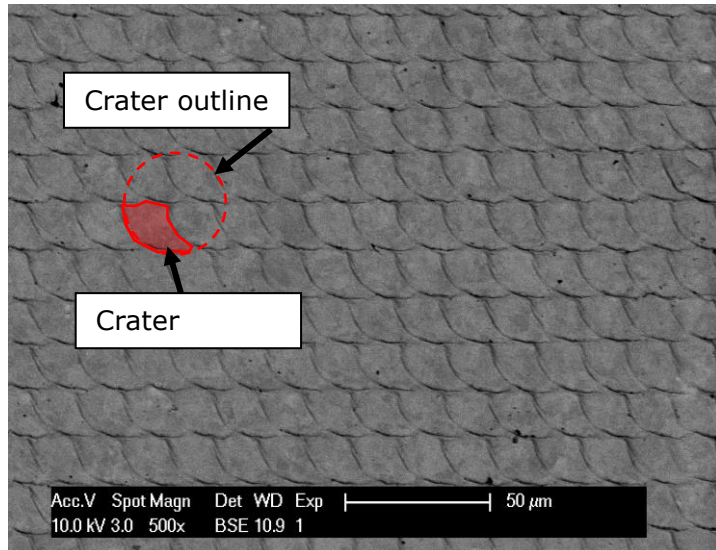


**Figure 36 - Example of regular surface topography from 10W, 400mm/s, and 25kHz processing parameters**

Certain surfaces produced by a range of parameter sets were then sectioned, mounted, polished down to 1 $\mu$ m surface roughness, then chemically etched to reveal the metallurgical microstructure directly at, and near to, the laser ablated surface. Figure 37 shows an example of minimal metallurgical change incurred from laser ablation processing using an optimum set of parameters. Notice the grain structure at the laser treated surface is very similar to the grain structure away from the surface, indicating no microstructural change has occurred. There is also no visible recast, or oxide layer on this sample. EDX analysis confirmed minimal or no oxide formation on any of the samples which produced good surface finishes.

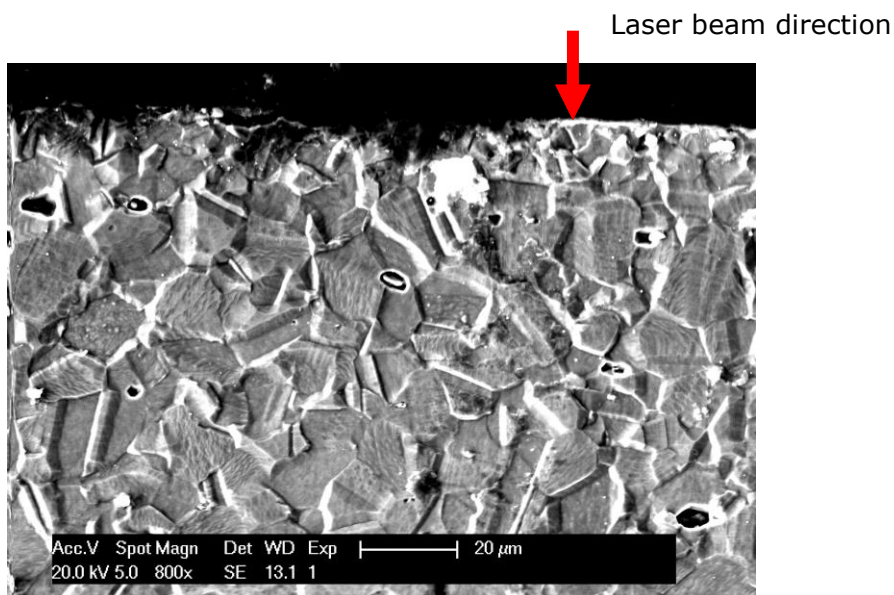


**Figure 37 - Cross section of optimal sample displaying low recast thickness and metallurgical change, ablated at 15W, 400mm/s, and 25kHz**

#### 4.3.2.2 Recast thicknesses

Sections of all samples were analysed under SEM equipment such that recast thicknesses could be quantified. It should be noted that for the samples with higher degrees of recast ( $>50\mu\text{m}$ ), more variation was seen between the maximum and minimum recast layer thickness. These values were judged by eye from SEM images, and as such a  $\pm 5\mu\text{m}$  deviation in measurement is noted. Table 5 shows recast thickness measurements for all ablated samples in this experiment.

Table 5 - Measurements for recast thickness for all ablated samples			
Power (W)	Frequency (kHz)	Scan speed (mm/s)	Maximum recast Thickness $\pm 5$ ( $\mu\text{m}$ )
20	25	400	20
20	25	800	*
20	25	1200	70
20	50	400	60
20	50	800	20
20	50	1200	30
20	75	400	15
20	75	800	15
20	75	1200	10
15	25	400	5
15	25	800	5
15	25	1200	5
15	50	400	20
15	50	800	10
15	50	1200	20
15	75	400	20
15	75	800	15
15	75	1200	15
10	25	400	5
10	25	800	*
10	25	1200	*
10	50	400	10
10	50	800	<5
10	50	1200	<5
10	75	400	10
10	75	800	<5
10	75	1200	5

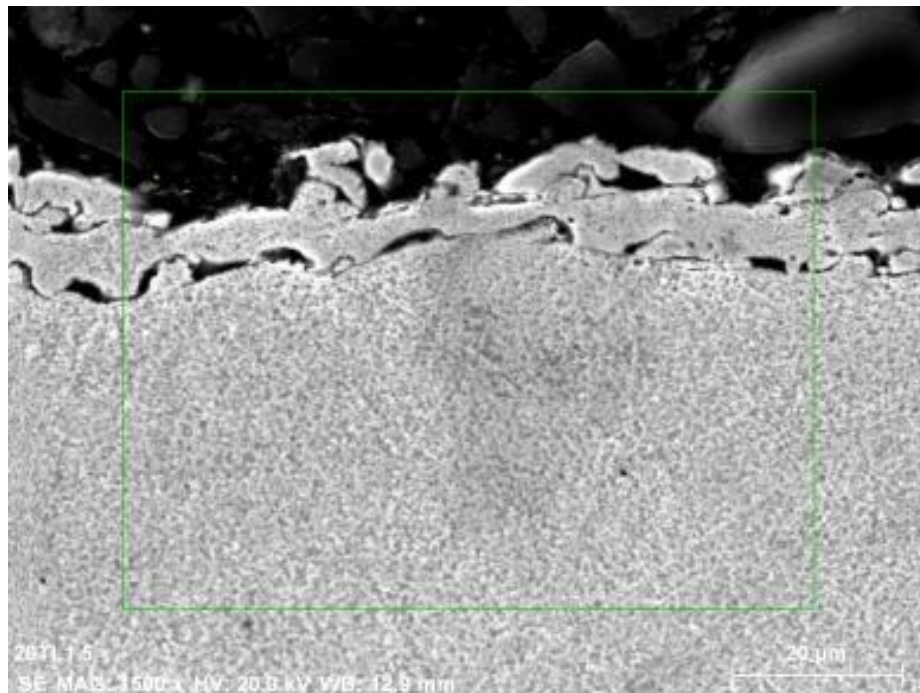
\* Sample surfaces damaged and rendered unmeasurable by SEM equipment.

SEM analysis was carried out on samples to quantify any metallurgical changes that may have happened within the sample cross section. In general, higher power samples displayed higher thickness of recast. The following section presents some

examples of microstructural cross sections of note, including those with high levels of recast, or well-maintained crystalline microstructure after ablation. Cross sections are accompanied by qualitative images showing the ablated surface for comparison. For comparison, an example of a surface with minimal recast and microstructural change (ablated with an optimum set of laser parameters) is shown in the previous section, in Figure 37.

In contrast to samples ablated at higher power, when paired with high pulse repetition frequencies, producing sub-optimal recast layers and microstructures, the samples which were ablated at low to medium powers (10-15W), with pulse repetition frequencies between 25-50kHz, produced minimal recast layer thicknesses and microstructural changes.

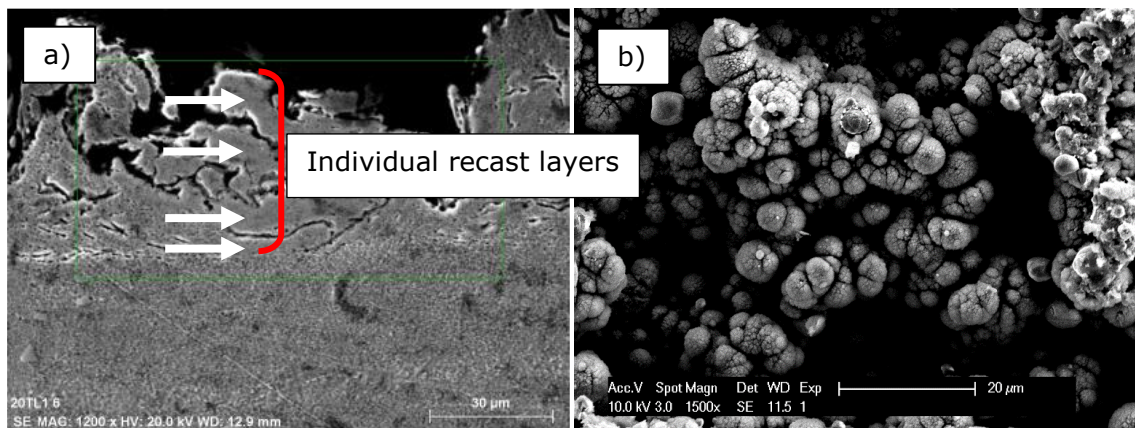
Some samples presented a 'mid-range' surface quality, with recast layer thicknesses ranging from approximately 10-20 $\mu\text{m}$ , such as the sample shown in Figure 38.



**Figure 38 - Sample ablated at 20W, 400mm/s and 25kHz**

The sample ablated at 20W, 400mm/s, 50kHz shows a high degree of recast material in the cross sectional SEM image (Figure 39a). The thickness of recast varied from approximately 20 to 60 $\mu\text{m}$ , with a highly irregular internal structure. Successive pulses likely produced layers of recast which solidified on top of previous recast material generated by preceding pulses, with clear separation lines between the layers visible in the cross section. There is also visible, albeit irregular,

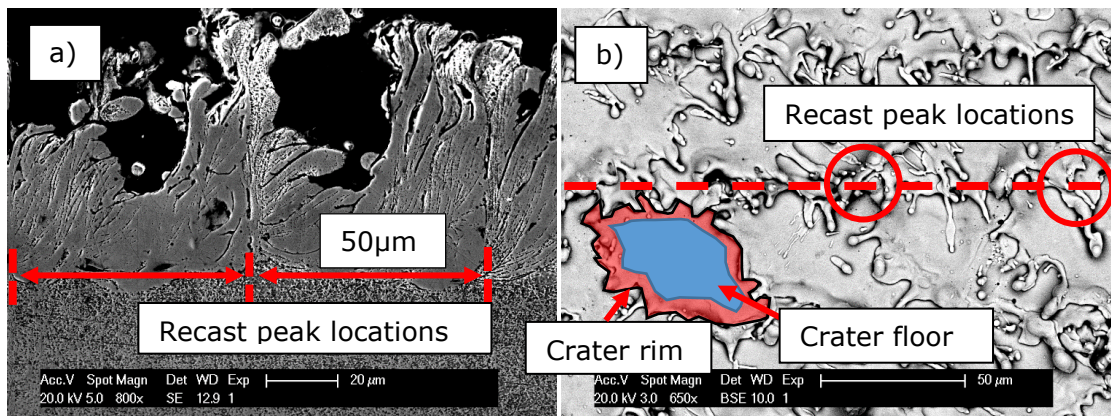
separation between the recast layer and the underlying parent material, similar to the recast-parent material separation line visible in Figure 32. As such it is possible that this recast layer would not remain firmly attached to the parent material under loading. A top-down view of the same sample (Figure 39b) shows the high irregularity in the thickness of this recast layer. It also shows an interesting morphology of the recast material, with a pop-corn like structure. A topography like this may arise from highly overlapped pulses, with an 8 $\mu\text{m}$  offset between successive pulses with process parameters of 400mm/s and 50kHz. When laser ablated craters are in the order of 50 $\mu\text{m}$  in diameter, as seen in Figure 39, this represents an approximate 84% overlap resulting in at least 5 laser pulses being placed upon any given point on the material surface. As such, repeated material heating, melting and recasting will result in compounded recast structures (indicated in the figure with white arrows) separated by void areas. These recast structures will undergo heating from successive pulses, and will either be removed by ablation, heated and re-melted before recasting, or simply heated with no structural change. In the case where the structure is heated with minimal melting and recasting (indicated by the clear voids between successive recast layers) oxidation may occur as thermal energy builds up within the recast structure from successive laser pulses. This oxide will appear as lighter, white pixels in the SEM image presented.



**Figure 39 - a) Cross sectional and b) Top-down view of sample ablated at 20W, 50kHz and 400mm/s**

The sample ablated at 20W, 1200mm/s and 25kHz shows a similar structure both internally and externally. An irregular recast structure, with peaks as high as 70 $\mu\text{m}$  above the parent material surface (Figure 40a) and a clear distinction between the recast and parent material suggest a similar set of process characteristics to the sample ablated at 20W, 400mm/s and 50kHz. The recast structure also has a more regular undulation between its peaks and troughs (70 to 20 $\mu\text{m}$ ). However when looking at the top-down surface image (Figure 40b) it is clear that the two samples

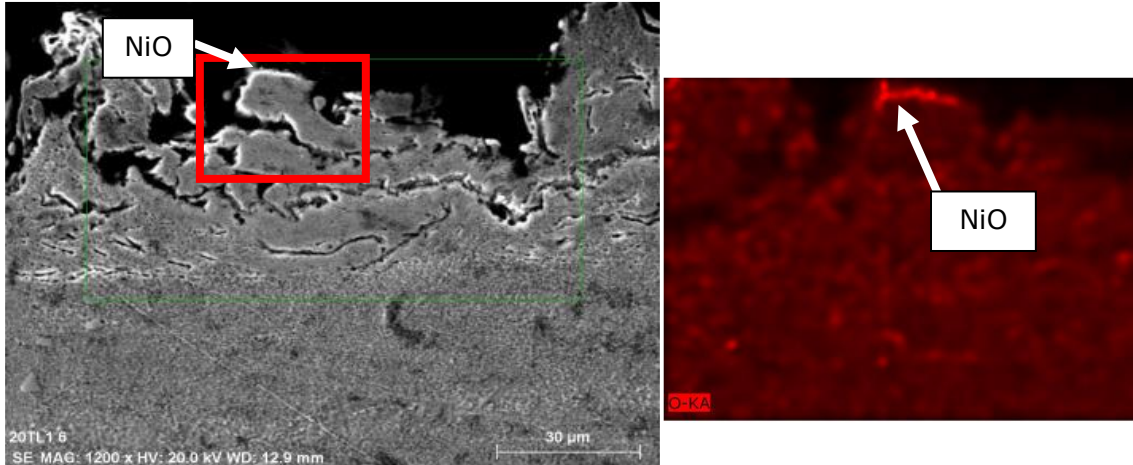
are very different. Where sample the sample ablated at 20W, 400mm/s and 50kHz shows a highly rough and irregular surface, the sample ablated at 20W, 1200mm/s and 25kHz shows a much flatter surface but only at the centre of ablation for each pulse (i.e. at the centre of the laser spot). This is likely due to the higher spot offset (48 $\mu$ m vs. 8 $\mu$ m) resulting in fewer laser pulses (1-2 vs 6-7 with a 50 $\mu$ m approximate crater size) affecting any given point on the sample surface. Having more distance between successive pulses will result in more of the smooth, flatter part of a crater floor (shown in blue in the figure) being left uncovered by the rougher, uneven crater rims (shown in red). Figure 40a shows high levels of recast and material redistribution. Therefore it is reasonable to assume that the cross section shown in Figure 40a was taken at a point where these craters meet, i.e. at the plane half way between two tracks of ablated craters indicated by the red line in Figure 40b. The large recast peaks seen in the cross sectional image (measured at approximately 50 $\mu$ m apart) are likely produced by the cumulative deposition of recast material at one location where multiple crater rims overlap.



**Figure 40 - a) Cross sectional and b) Top-down view of sample ablated at 20W, 1200mm/s, and 25kHz**

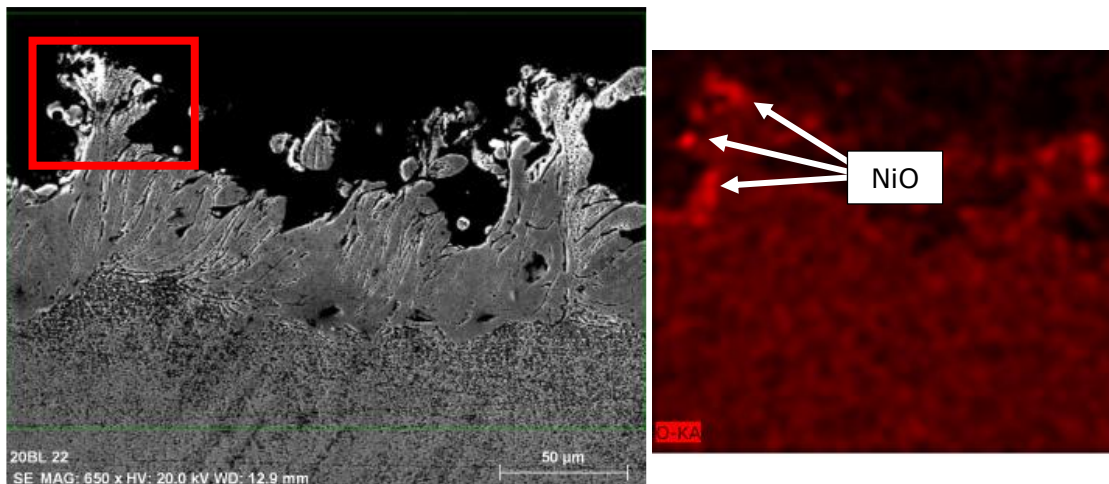
Chemical analysis performed by EDX on the Philips SEM system was done on all of the samples. Separate and combined colour maps (hypermaps) were obtained for each sample to show isolated concentration of individual elements, and to highlight if/where they commonly appear together. Few of the samples showed any indication of high concentrations of oxygen within the sample. Of those that did show any significant concentrations of oxygen, only isolated occurrences were observed (i.e. no continuous layer of oxide over a significant distance). In addition, the samples within which concentrated oxide phases were detected were those with the highest levels of recast; those shown in Figure 39 (ablated at 20W, 400mm/s 50kHz), and Figure 40 (ablated at 20W, 1200mm/s, 25kHz).

Figure 41 shows oxide detection for the sample ablated at 20W, 400mm/s and 50kHz. An isolated concentration of oxygen is visible. As such, oxygen dissolution into the component material in the form of oxide phases is of little to no concern in this process.



**Figure 41 - Oxygen detection in EDX hypermap for sample ablated at 20W, 400mm/s, 50kHz**

As in the sample ablated at 20W, 400mm/s and 50kHz, the sample ablated at 20W, 1200mm/s and 25kHz shown in Figure 42 only presents isolated occurrences of oxygen dissolution. It also only shows this oxygen presence at the top side of the recast layer. Any other oxygen detection was of such small concentrations that it was deemed insignificant. The reason for such a low amount of oxidation being observed across all ablated samples is most likely due to the limited time that the samples are being heated for. In the cases where laser pulses are placed very close together (a minimum of  $5.3\mu\text{m}$  offsetting between successive craters), there may be as many as 10 pulses directly imparting energy to the same localised area of material. To achieve this low pulse offset, a frequency of 75kHz and a scan speed of 400mm/s must be used. These pulses will therefore all be absorbed by the target material within approximately  $120\mu\text{s}$ . Other than indirect heating of the material from thermal energy dissipation from material surrounding the area in question, this is the maximum duration of direct heating it is exposed to. As such, there is little time for oxygen to dissolve into the heated material, as cooling will initiate almost instantly after the surface has been heated. Without the material being held at elevated temperatures for a prolonged period, oxidation is minimised [39].



**Figure 42 - Oxygen detection in EDX hypermap for sample ablated at 20W, 25kHz, 1200mm/s**

All samples ablated at 15W and 10W showed no oxide presence. When comparing these results to chemical analysis performed by XRD analysis (Figure 34 and Figure 35) it is clear that across all of the samples there is little to no significant oxide generation

#### 4.3.3 Statistical Analysis of impact of KPV values on metallurgical changes

Statistical analysis was performed to determine which of the 3 key process variables (KPVs), namely laser power  $P$ , pulse repetition frequency  $f$ , and laser beam scanning speed  $v_f$  had the biggest effect on recast layer thickness, volume of oxide phases generated, and any metallic phase changes in the parent material. Additionally, any interaction between the KPVs was analysed to further characterise the process and how to minimise these negative effects. Of all of these effects (recast thickness, micro-cracking, oxide generation, surface roughness and residual stress), recast thickness is the only one to have presented any potential problems as far as acceptance limits are concerned [1] given the findings presented thus far in the results section of this chapter. As such, this is the only parameter to be considered when quantifying the effects of KPV values.

#### 4.3.3.1 Statistical main effects

Figure 43 shows the effect on maximum depth of recast thickness observed from each of the key process variables (KPVs); power, frequency and scan speed. Pulse energy is included to highlight the interdependent nature of these variables. Pulse energy is defined as the energy transmitted in each laser pulse, and is calculated as Power / frequency. It can be seen that there is an obvious, positive correlation between power and recast thickness observed, with frequency and scan speed having less of an obvious effect. As each of the three plots for the KPVs (power, frequency, and scan speed) shows the mean for each level of the selected variable, the data points are mean values for 9 separate ablated samples.

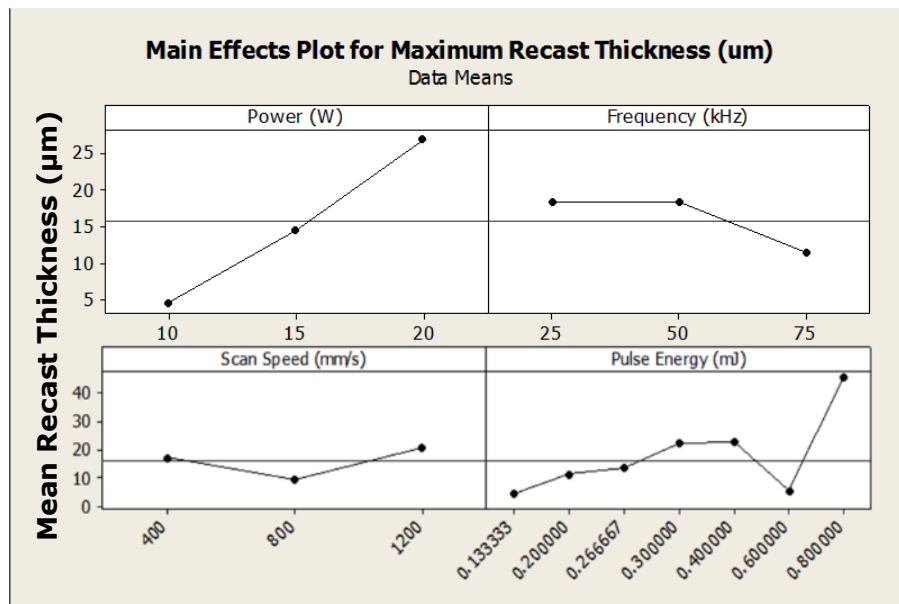
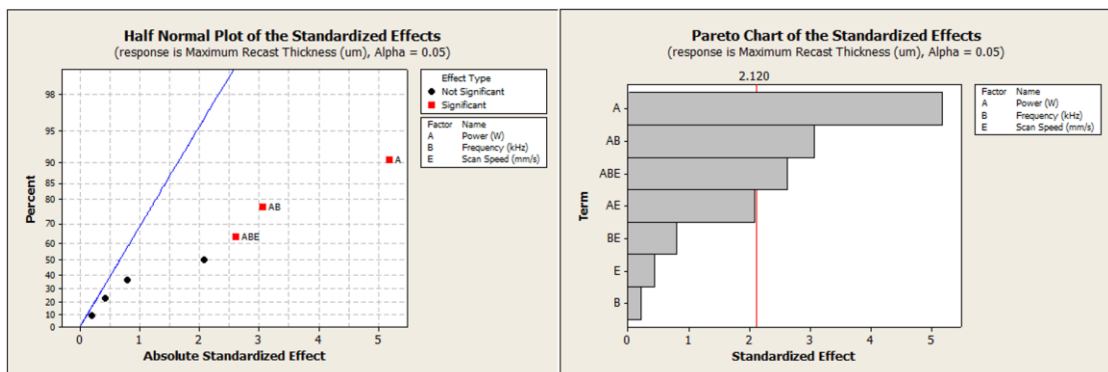


Figure 43 - Main effects plot for each controllable parameter on Maximum recast depth observed.

#### 4.3.3.2 Key process variable significance

Initial observations from studying the main effects on recast thickness from each of the KPVs indicated that power had the greatest effect. This is confirmed in Figure 44, where a pareto analysis was carried out to study the interactions between KPVs. A confidence interval was automatically determined within MiniTab software being used to carry out the analysis. It shows their effects, either as a standalone variable or combination of one or more variables, on the recast thickness. Again, it is clear that power has the greatest effect on recast thickness, as well as the combination of power and frequency i.e. pulse energy. It can be said also that scan speed, and other kinematic characteristics of the process such as crater offset (when combining frequency and scan speed) have less significant effects on recast thicknesses. As such, through the tests and analyses performed in this chapter, optimal KPVs can be selected to ensure minimum recast thickness of ablated surfaces. From Figure 44 it follows that a power should first be chosen to perform the process, followed by choosing a frequency which when applied to a certain power will result in an ideal pulse energy. Lastly scan speed can be selected whilst considering frequency to create a process with a desired crater offset. This offset may affect component features such as surface roughness or undulations.



**Figure 44 - Half normal and Pareto plots for the significance of each of the KPVs, and combinations of them, on maximum recast thickness**

#### 4.4 Observations from sample analysis

Pulsed laser ablation of IN718 with the ranges of the laser parameters used in this project does not result in the significant formation of any identifiable oxides on the surface of the material.

The recast layer and sub-recast surface quality appear to be the most significant surface concerns. The recast thickness and quality of the underlying surface (which could be prone to cracking on detachment of the recast layer) are crucial

determining factors in the parameter optimisation of PLA using the given range of parameter values. Within the set of parameters being varied, power and frequency significantly affect the surface quality and morphology of IN718, compared to scan speed which affects it to a lesser extent. The samples ablated at a power of 10W generally produced the best quality surface but this power will be unsuitable because the laser will then have very low material removal capabilities and processing speeds.

#### 4.5 Summary

From the given range of the selected parameters, PLA of IN718 will produce surface quality and effective integrity, that is satisfactory whilst also ensuring acceptable processing speeds, when the laser key process variable values include; a laser input power of 15W (measured at the laser output at 13W), a frequency of 25kHz and a scan speed of 400 mm/s. At these parameter values, the ablated surface showed minimal material redistribution and cross-sectional analysis demonstrated a minimal recast layer depth with no significant oxidation.

The full factorial design of experiments (DoE) and qualitative analysis approach that has been employed to optimise the process parameters in this project seems to be effective. This is due to the narrow operating range that has been used to explore the phenomena. However, considering these operations from a large-scale industrial perspective (where several factors will be considered at several levels), further investigations would need to be performed following a slightly more quantitative route to optimisation.

The values for the parameters selected through this process (laser power, pulse frequency and scan speed) show promise to produce a repair feature with suitable surface quality and metallurgical integrity for in-service aerospace components where safety is a major concern.

# Chapter 5. Laser Beam – Work piece interaction at micro-geometrical level

The generation of micro-features in a predictable and repeatable manner by use of pulsed laser ablation requires an understanding of the temporal and energetic distributions of the laser beam upon the workpiece surface. Modelling the response of the material to known energetic and kinematic parameters of the pulsed laser ablation process can be carried out in a discretised time-based approach, allowing the workpiece topography to be simulated mathematically to reflect a real-life process. Considerations of the antecedent workpiece surface texture such as increases in irradiated area due to the surface gradient, and increases in laser spot size due to beam divergence throughout the elevation of the workpiece are used to predict energy densities and hence the resultant ablated depth and texture of the targeted surfaces. A fully calibrated Yb:YAG pulsed fibre laser (SPI G3.0 RM) was used to validate the model on two materials, highlighting the models strengths for different material types. It was found in experimentation that Ni-based (i.e. INCONEL<sup>®</sup> 718) workpieces presented redeposition phenomena under these laser ablation conditions, similar to those found in literature on other metallic targets [28]–[30].

To understand the response of the proposed model without when redeposition is not present, validations trials on materials that do not present such side effects, e.g. diamond, were carried out and differences were found to be up to 9.39% when using pulse durations in the nanosecond range. In addition to validating the model on CVD diamond targets using the SPI G3.0 laser, calibration and validation experiments were also performed using an EWAG LaserLine system which displayed very low errors (<1%) in some cases, but validating samples outside of the model's capabilities errors were seen to grow. Finally, including an empirical model of the material redeposition, the validation of the proposed surface texture model was carried out on INCONEL<sup>®</sup> 718 and results proved to be promising (i.e. errors as low as 1.3%).

## 5.1 Introduction to mathematical modelling approach

### 5.1.1 Scope of the mathematical model

This chapter presents a mathematical model which can be calibrated for any material, laser and set of dynamic and energetic parameters to determine the dynamic effect, i.e. micro-topography, when pulse laser ablation of a target surface. This model will use an experimentally determined logarithmic relationship between fluence levels and the maximum depth of the laser crater while taking into account for the overlapping of pulses, depth of field and the surface gradient of the component. Finally the model is validated on INCONEL® 718 and CVD diamond.

In this respect, the model for surface micro-topography obtained by PLA takes into consideration the following aspects:

- The depth of field effect: the reduction in fluence due to the workpiece surface being off the focal point of the laser.
- The surface gradient effect: the reduction in fluence due to the laser spot energy being distributed over an increased area due to the target surface not being parallel to the laser focal plane.
- The relationship between laser fluence on the sample surface and ablated crater depth for specified materials.
- A step function accounting for the placement of the laser pulses along a track scanned across the sample surface.

The development of a mathematical model presented in this chapter will create a baseline technique for characterising features created by pulsed laser ablation in a specific material (INCONEL® 718) using a specific laser system (SPI G3.0). After having established an accurate pulse-by-pulse modelling method, characterisation of larger 2.5D features is possible. Dependent on computing resources available, either full 2.5D features or smaller sections of a blend may be modelled.

By incorporating results from the previous chapter on parametric optimisation of the process, predictive material removal rates/repair process times and surface finishes can be estimated using this model.

### 5.1.2 Approach in modelling of surface roughness in PLA

The analytical modelling approach presented in this chapter does not consider material redeposition, but only the primary effect of material removal. To evaluate

the robustness of the analytical models and validation trials were carried out on diamond (which does not present the material redeposition phenomena). Furthermore, experimental calibrations and validation trials were carried out on INCONEL® 718 to empirically evaluate the secondary effect of material redeposition.

The methodology for predicting the surface micro-topography under pulsed laser ablation involves several stages. The first stage involves the collection of various laser specific parameters, defining initial conditions such as pre-ablation workpiece texture. Secondly, laser-material interaction calibration data must be gathered from sets of experimentally generated craters to allow the model to interpolate ablated depths at different fluence levels. Lastly, the fluence field is generated considering its reductions that may arise from pre-existing surface gradients (non-orthogonal angles of incidence) and laser spot diameter increases arising from beam divergence. On a pulse-by-pulse basis, the antecedent workpiece micro-topography outputted from the model is used as an input surface for the next pulse. Hence, any overlapping pulses are calculated after considering effects of the preceding pulse.

Therefore, a kinematic/energetic model is presented to assess the evolution workpiece surface micro-topography throughout a prescribed process with known parameters, on a specific laser system and target material. Of course, having different material and laser specifications, the procedure for calibrating the model as presented in the following should be carried out.

Figure 45, showing a generic freeform surface with the focal plane of the laser (grey), highlights the two main considerations of this model: (i) surface area increase arising from a non-flat angle of incidence for the laser beam; (ii) increase in laser spot size due to its divergence characteristics. The divergence behaviour of the laser beam is presented, demonstrating that at a location on the workpiece which does not lie on the focal plane, the laser spot diameter will be larger than that at focus. In addition to increased spot diameter away from the focal plane, a

distorted laser spot also demonstrates the increase in irradiated area through spot 'stretch' when incident upon a non-flat surface.

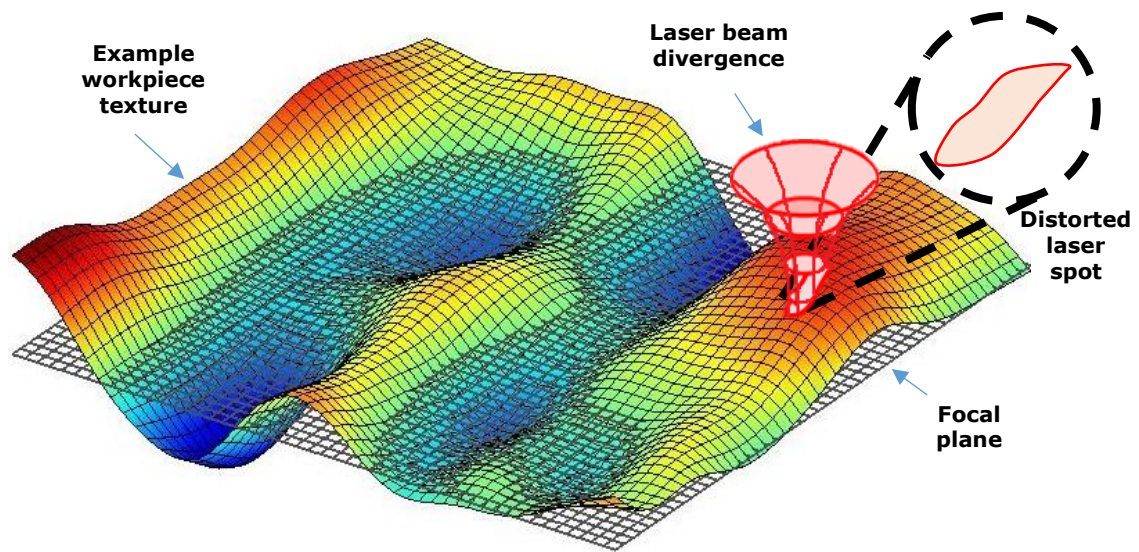


**Figure 45 - Top: Example workpiece texture with focal plane (grey) and laser beam divergence (red)**

### 5.1.3 Geometrical modelling of pulsed laser ablated surfaces

The model works on the principle of a pulse-by-pulse evaluation of a laser ablation process. Starting from a set of isolated pulses generated in known (i.e. set frequency, pulse duration, wave form and power) conditions and imitating a specific laser system and its operating range/tolerances it allows the demonstration of what components and features a laser system is capable of producing. Each laser pulse is 'projected' onto the antecedent (non-flat) workpiece surface. This results in surface texture data for the entire working area, before and after each pulse. The model describes these features within a steady kinematic state working area of the system – where beam velocities and pulse repetition frequencies are constant; these capabilities are available on state-of-the-art galvanometer mirrors that manipulate the laser beams in x-y axis.

To model the evolution of workpiece surface micro-topography throughout a process, the effects of individual laser pulse on the surface must be considered. By determining the effect of a laser pulse at a known position and set of known laser parameters (power, frequency, wavelength etc.) a response of the material can be modelled.

### 5.1.4 Generic relationship between laser fluence and depth of ablation

To calibrate the model to a specific material and laser system, experimental data can be analysed to determine a relationship between depth of ablated material and the incident energy on the surface.

Research and experimental data suggest that the relationship takes the generic form [26], [34], [61]–[63] as in Eq. 4.1a. Calibration between a specific laser system and a specific target material gives the equation relating ablated depth to incident laser fluence.

$$\Delta h = a' \log (\Phi) + b' \quad (4.1a)$$

where:  $a'$  and  $b'$  - constants depending on workpiece material and laser type

$\Phi$  - actual fluence that takes into consideration the beam out off focus, gradient of the target surface

To give the constants  $a'$  and  $b'$  units of length, the logarithm is taken of the ratio between the actual fluence for the pulse ( $\Phi$ ) and the reference fluence ( $\Phi_0$ ), thus, resulting in a normalised fluence as in Eq. 1b. This reference fluence may be, for example, the maximum fluence achievable by the chosen laser system, occurring when the pulse energy is at a maximum, and the laser spot diameter is at the minimum size allowable by any optics being used.

$$\Delta h = a \log \left( \frac{\Phi}{\Phi_0} \right) + b \quad (4.1b)$$

Calculation of the reference fluence ( $\Phi_0$ ) will be dependent on the laser system to be used. In some systems, there will be a pulse repetition frequency (in this setup  $f_0=25$  kHz) below which laser output power is reduced to maintain constant pulse energy; this is to protect internal components from excessively high peak powers and any possible damage. With the maximum power laser output being  $P_{max}$ , the maximum pulse energy of a laser system of this type can derived as;  $E_{max} = \frac{P_{max}}{f_0}$ .

To make use of the modelling approach proposed in this chapter, initial calibration between the target material and the proposed laser system must be done. This calibration informs the model about the relationship between depth of craters made by the laser beam and the input laser fluence.

As 'instantaneous' ablation is assumed, there is a need to recalibrate the model for any different laser, or different pulse duration/pulse shape on the same laser. Thus, without multi-physics simulation of the process, it is possible to use the model for fast computational evaluation of real micro/macro-features generated by pulsed laser ablation.

#### 5.1.4.1 Fluence definition and calculation when considering a freeform target surface

In this model, the fluence across an element on the workpiece, not necessarily flat, is defined by the total energy incident on an area  $A$ . As  $\delta x$  and  $\delta y$  tend towards 0, a fluence field  $\Phi(x, y)$  can be described as a function of location on the workpiece  $(x, y)$ . The formula describing fluence as a function of laser average power  $P$  (W) and pulse repetition frequency  $f$  (Hz) is as follows:

$$\Phi = \frac{P}{f\delta x\delta y} \quad (4.2)$$

Therefore, the maximum fluence from the energy distributed over a laser spot of diameter  $\varphi$  is:

$$\Phi_{max} = \frac{8P}{\pi f\varphi^2} \quad (4.3)$$

Eq. 4.3 assumes that the maximum fluence (typically located at the centroid of the beam) is twice the average fluence over the whole laser spot, for a typical near-TEM<sub>00</sub> (Gaussian) beam, [21].

#### 5.1.4.2 Kinematics of the beam

The  $(\bar{x}_i, \bar{y}_i)$  location of the centre of laser beam at any point in time,  $t_i$ , can be described by Eq. 4.4 and 4.5.

$$\bar{x}_i(t_i) = x_i + v_{fx}t_i \quad [\bar{x}_i = x_0 + \delta x_{track}(N_{track} - 1)] \quad (4.4)$$

$$\bar{y}_i(t_i) = y_i + v_{fy}t_i \quad [\bar{y}_i = y_0 + \delta y_{track}(N_{track} - 1)] \quad (4.5)$$

Where  $(\bar{x}_i, \bar{y}_i)$  – position of the laser beam at a moment,  $i$ ;  $x_0, y_0$  – initial position of the laser beam;  $N_{track}$  – nominal track number in parallel hatching.

From the beam path arbitrary angle,  $\theta$ , with respect to the reference frame (XYZ) as presented in Figure 46, the velocities in x and y can be formulated as Eq. 4.6 and 4.7.

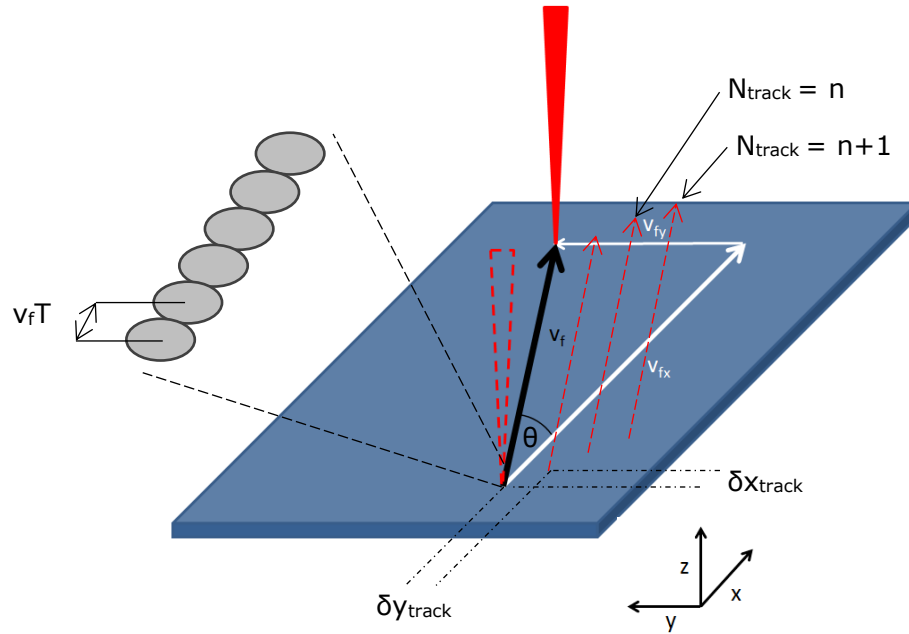


**Figure 46 – Pulse and track offsetting with beam path at an angle to reference axes**

$$\vec{v}_{fx} = \vec{v}_f \cos(\theta_i) \quad (4.6)$$

$$\vec{v}_{fy} = \vec{v}_f \sin(\theta_i) \quad (4.7)$$

A real process (and real processing equipment) will include transient behaviour such as galvanometer mirror acceleration, power ramp up etc. These effects will have localized inferences on the positioning of the laser beam at any point in time (e.g. at scan geometry edges), or ablated depths. In addition to this, for a machine not using an F-Theta type lens the spot size will vary radially from the optical axis. This will then introduce an error on fluence calculation as spot size is assumed to be constant within any given plane parallel to the focal plane of the laser.

### 5.1.5 Time modulation of laser input signal

Time modulation of a laser process, in this model, considers only the time period  $\mathbf{T}$  (i.e.  $1/f$ ) between consecutive pulses. The model does not simulate the process of ablation, i.e. physics of material removal, throughout the pulse duration  $\tau$ , where  $t_i \leq t \leq t_i + \tau$ . The implication of this is such that calibration of the model must be done for each separate pulse duration/pulse shape to be used in the ablation process. As a result, by combining Eqs. 4.4, 4.5 and considering the modulation below, the  $(\bar{x}_i, \bar{y}_i)$  centre of a laser pulse can be examined. For the range of

operating scan speeds, frequencies and durations of the pulses to be considered in this model, the significance of laser spot stretch (increase in effective size of laser spot in scan direction) could be negligible. For example, at a high scan speed of 2000mm/s (often used for material ablations) and pulse duration of 20ns leads to 40nm spot stretch which represents  $\sim 0.1\%$  of the spot diameter, hence the negligibility of this effect.

For this model, time modulation  $g(t+T)$  is used to modulate the instantaneous ablation process. Whilst the process is simulated, only at times when  $g(t+T) = 1$  (shown in Figure 47) will there be a laser pulse.

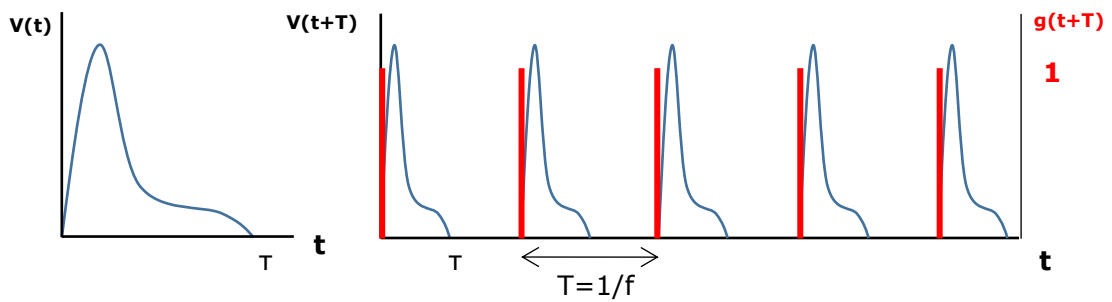


**Figure 47 – Example laser control output voltage  $V(t)$  pulse shape and pulse train**

### 5.1.6 Instantaneous spatial energy distribution of the beam

To expand the calculation of fluence for a single laser spot to a fluence field over the whole workpiece, the location of the beam  $(x_i, y_i)$  and the beam diameter  $\varphi_z$  at a surface height  $z$  away from the focal plane of the laser are needed. These can be applied using the energy density distribution behaviour of the beam (in this case Gaussian) to any point  $(x_i + \delta x, y_i + \delta y)$  on the workpiece surface. Radial ( $r$ ) positions away from the beam centre have intensity  $I'$  defined in the distribution:

$$I'(r, \varphi_z, (x_i, y_i)) \quad (4.8)$$

Normalising this intensity, and expressing it in terms of Cartesian coordinates results as in an expression (Eq. 4.9) which can easily be applied to the workpiece coordinate system. Re-scaling of this normalised field (for the whole work piece surface) to reflect the maximum fluence which is assumed to be at the centroid of the beam  $(x_i, y_i)$ , the fluence field can be derived;

$$I'(r, \varphi_z, x_i, y_i) \Rightarrow I(x_i, y_i, \varphi_z) \quad (4.9)$$

$$\Phi_z(x, y) = \Phi_{max} \cdot I(x_i, y_i, \varphi_z) \quad (4.10)$$

### 5.1.7 Laser divergence and depth of field

Due to the nature of how laser beams are focused, at a plane which is not within the focal plane, the laser spot diameter ( $\varphi_z$ ) is increased. On the focal plane ( $\mathbf{z}=\mathbf{0}$ ) the laser spot has a theoretical minimum diameter  $\varphi_0$ . For an 'F-Theta' lens, with planar focus, any work plane which is parallel to, but offset from the focal plane in the direction of the laser radiation propagation (with offset height  $\mathbf{z}$ ), the spot diameter for a beam with Gaussian energy density distribution and wavelength  $\lambda$  is expressed as follows [64]:

$$\varphi_z = \varphi_0 \sqrt{1 + \left(\frac{z}{z_R}\right)^2} \quad \text{Where } z_R = \frac{\pi \varphi_0^2}{\lambda} \quad (4.11)$$

Where  $z_R$  denotes Rayleigh length; the value of offset height  $\mathbf{z}$  at which the laser spot area is doubled (the laser spot diameter is increased by a factor of  $\sqrt{2}$ ).

Laser beams have a theoretical minimum divergence and hence spot size for a given set of optics and wavelength. This theoretical beam behaviour is known as a 'perfect' beam. For real laser beams (with divergence properties greater than the theoretical minimum), a factor  $\mathbf{M}^2$  is used to approximate the divergence behaviour of the beam relative to that of a 'perfect' quality beam [65]. This factor describes the increased divergence of a real beam compared to a theoretical, perfect one. As such, multiplication of the laser spot size by this factor will give the actual laser spot diameter, at any height  $\mathbf{z}$ :

$$\varphi_z = \varphi_0 M^2 \sqrt{1 + \left(\frac{z}{z_R}\right)^2} \quad (4.12)$$

The maximum fluence at any height (Eq. 4.13) and in the focal plane (Eq. 4.14), i.e. absolute maximum, can be obtained as follows:

$$\Phi_{z,max} = \frac{8P}{\pi f \varphi_z^2} \quad (4.13)$$

$$\Phi_{0,max} = \frac{8P_{max}}{\pi f_0 \varphi_0^2} \quad (4.14)$$

To express the change in laser spot diameter at a plane with height  $\mathbf{z}$  with regards to the minimum spot diameter (on focus), the fluence at the work surface can be calculated proportionally to the square of spot sizes at height  $\mathbf{z}$  and focal plane. Based on Eq. 4.10, this can be used to express the fluence field, corrected for change in laser spot size due to surface height, at any point on the work piece surface.

$$\Phi_z(x, y) = \frac{8P}{\pi f \phi_0^2} \cdot \left(\frac{\phi_0}{\phi_z}\right)^2 \cdot I(x, y, \phi_z, \bar{x}_l, \bar{y}_l) \quad (4.15)$$

### 5.1.8 Variability in irradiated surface area per pulse

Throughout the ablation process, the laser beam incidents the target surface in non-orthogonal conditions. This is not only related to the macro-geometry of the surface but also at the micro-geometry level when the laser beam could impact on micro-features of similar dimensional order as the laser spot size (<50um).

For a completely flat target workpiece, the fluence can be accurately calculated with all equations up to Eq. 4.15. However, if there is a surface gradient at any point, then the effective surface area over which the energy is distributed (Figure 45) increases compared with the situation when a flat plane is targeted by the laser beam.

Obtaining the gradient in x and y of the surface  $h$ ,  $\frac{\partial h}{\partial x}$  and  $\frac{\partial h}{\partial y}$  respectively, allows the calculation of the area of a surface element (Eq. 4.16) and a factor of increased area for a point as  $\delta x$  and  $\delta y$  tend towards to 0 (Eq. 4.17) as follows;

$$dS' = \iint \sqrt{\left(\left(\frac{\partial h}{\partial x}\right)^2 + \left(\frac{\partial h}{\partial y}\right)^2 + 1\right)} dA \quad (4.16)$$

$$dS = \sqrt{\left(\frac{\partial h}{\partial x}\right)^2 + \left(\frac{\partial h}{\partial y}\right)^2 + 1} \quad (4.17)$$

This increase in area reduces the laser fluence incident on any location on the workpiece. The ratio of Eq. 4.17 and the size of an element  $dA$  in the laser view plane will describe the ratio of fluence that is on a non-flat surface;

$$\Phi_{z,non-flat}(x, y) = \Phi_{z,flat}(x, y) \cdot \frac{dA}{dS} \quad (4.18a)$$

$$= \left[ \Phi_{z,flat}(x, y) \cdot \frac{1}{\sqrt{\left(\frac{\partial h}{\partial x}\right)^2 + \left(\frac{\partial h}{\partial y}\right)^2 + 1}} \right] \quad (4.18b)$$

## 5.2 Compounded material removal function

Consideration of all of the effects described, the fluence for any location  $(\mathbf{x}, \mathbf{y})$ , at any point in time  $\mathbf{t}$ , can be used, with knowledge of the antecedent surface data  $h(\mathbf{x}, \mathbf{y}, \mathbf{t} - \delta \mathbf{t})$ , to calculate the change in height (if any). Iterative evaluation of this formula at time steps  $\delta \mathbf{t}$  will therefore describe the evolution of a workpiece surface throughout a laser machining process.

$$\delta h(x, y, t) = -a \log \left[ \frac{g\left(t+\frac{1}{f}\right) \cdot \frac{8P}{\pi f \phi_0^2} \cdot \left(\frac{\phi_0}{\phi_z}\right)^2 \cdot I(x, y, \phi_z, \bar{x}_i, \bar{y}_i)}{\frac{8P_{max}}{\pi f_0 \phi_0^2} \sqrt{\left(\frac{\partial h}{\partial x}\right)^2 + \left(\frac{\partial h}{\partial y}\right)^2 + 1}} \right] + b \quad (4.19)$$

For a process containing N pulses taking a total time  $t = \frac{N}{f}$  with a time step of  $\delta t = \frac{1}{f}$ ,

$$h(x, y, t) = h(x, y, t - \delta t) + \delta h(x, y, t) \quad (4.20a)$$

$$h_N(x, y, t) = h(x, y, t_0) + \sum_{t=0}^{\frac{t=N}{f}} \delta h(x, y, t) \quad (4.20b)$$

$$= h(x, y, t_0) - \sum_{t=0}^{\frac{t=N}{f}} a \log \left[ \frac{g\left(t+\frac{1}{f}\right) \cdot \frac{8P}{\pi f \phi_0^2} \cdot \left(\frac{\phi_0}{\phi_z}\right)^2 \cdot I(x, y, \phi_z, \bar{x}_i, \bar{y}_i)}{\frac{8P_{max}}{\pi f_0 \phi_0^2} \sqrt{\left(\frac{\partial h}{\partial x}\right)^2 + \left(\frac{\partial h}{\partial y}\right)^2 + 1}} \right] + b \quad (4.21)$$

Figure 48 shows a step by step combination of the above functions, resulting in the workpiece surface texture simulation. These steps are shown below.

- 1) Define input constants to the model, and the initial workpiece surface texture data.
- 2) Calculate the energy density (equation 9) at each point (x,y) on the workpiece.
- 3) Correct fluence field (Eq. 4.18) for increase in laser spot size, due to surface area (Eq. 4.17) and depth of field (Eq. 4.13) effects, at every location in the workpiece.
- 4) Using experimentally defined logarithmic equation (Eq. 4.1), output resultant surface texture (micro-topography) using corrected fluence field (Eq. 4.21).

5) Increment time index and repeat steps 2 onwards until simulation is complete

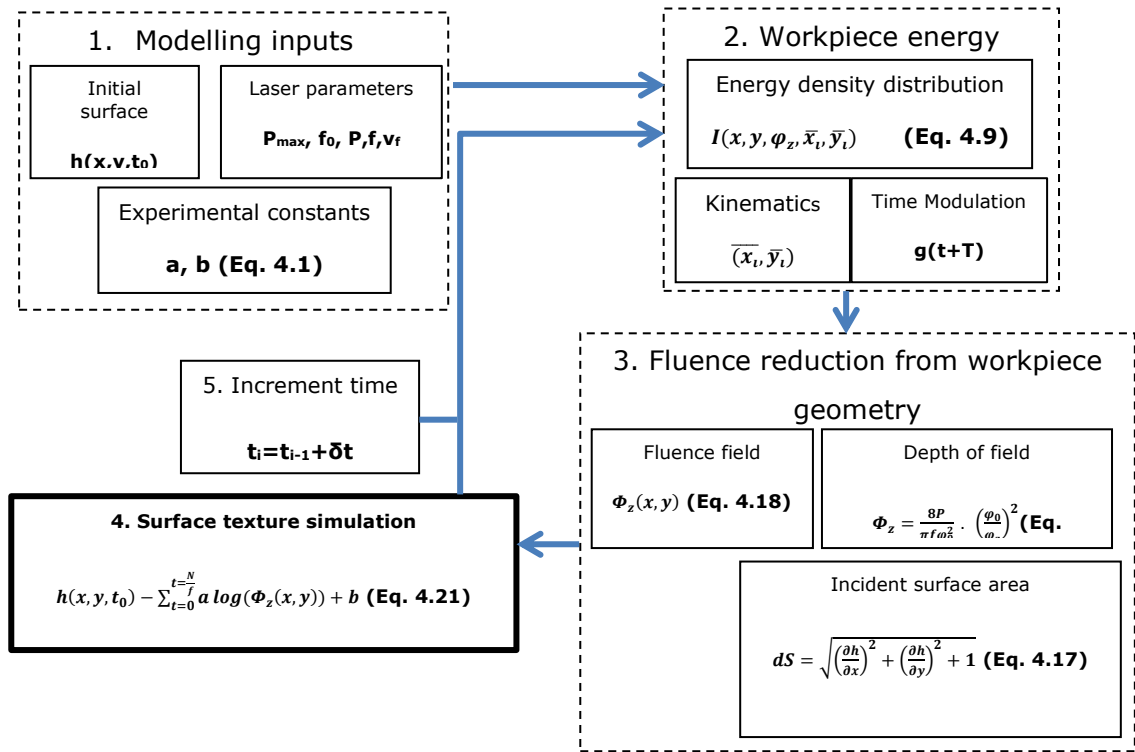


Figure 48 – Compounded material removal functions (Eq. 4.1-4.21) flowchart based on discrete time increments  $\delta t$

$h$  = Surface height (m)

$P$  = Average power output (W)

$t$  = Time (s)

$P_{\max}$  = Maximum power output (W)

$f$  = Pulse Repetition Frequency (Hz)

$\varphi$  = Laser spot diameter (m)

$f_0$  = Attenuating Pulse Repetition Frequency (Hz)

$a, b$  = Constant (m)

### 5.2.1 Surface prediction in the presence of material redeposition

If the chosen material exhibits redeposition at the edges of ablated craters within the fluence range considered, then large errors may occur in prediction if there is no quantification and modelling included for this phenomenon.

For previous models of surface texture prediction under pulsed laser ablation, simplistic methods were used, if any, to model redeposition. Rims of constant height (no variation/undulation) have been considered [26], [66], [67], however it is clear from observation that this is not highly accurate as material is deposited in localised mounds [68], leading to an undulating rim around the crater.

To improve on this aspect of modelling a three stages process for describing the redeposition around the crater is considered.

Firstly, the height and width of the rim are determined in accordance with experimental data. These values are used to describe a parabola, whose equation also includes the radial position of the rim (how far away it lies from the crater centre).

This parabolic section is then rotated in 3D to give a raised 'rim' around the crater, of the prescribed width and height. This will generate a rim of constant height and width around the crater, which imitates the height and width of the redeposition observed on the real craters.

Lastly, from frequency analysis of experimentally generated redeposition rims, a number of undulations are applied to the rim. This is done by scaling the rim to heights varying between maximum and minimum observed values. This undulation occurs at a set angular period, determined by the frequency analysis carried out previously. The undulation is also given a 'randomised' orientation, such that consecutive craters will not 'redeposit' material in the exact same place when simulated.

In summary, the model proposed in this chapter is comprised of an analytical approach for calibrating and predicting ablated depths of craters and their profile, and an empirical method for approximating the redistribution of material around the edge of a crater.

### 5.3 Methodology and experimental design for model calibration and validation

To evaluate the validity of the proposed model an extensive set of experiments was conducted. The proposed methodology relates the instantaneous fluence level at any (x,y) location on the workpiece in terms of laser energetic (e.g. power) and kinematic (e.g. scanning speed) parameters, and hence a simulated ablated certain , to experimental measurements of craters ablated with the same energetic and kinematic parameters ablated sample surfaces..

The validity of the model was tested on two materials with different responses, i.e. Ni-based superalloy, INCONEL® 718 (showing material redeposition) and CVD diamond (without material redeposition), to the laser type used (Yb:YAG). The choice of CVD diamond, as a control experiment free of significant secondary effects (e.g. material redeposition), was based on its unique thermal properties

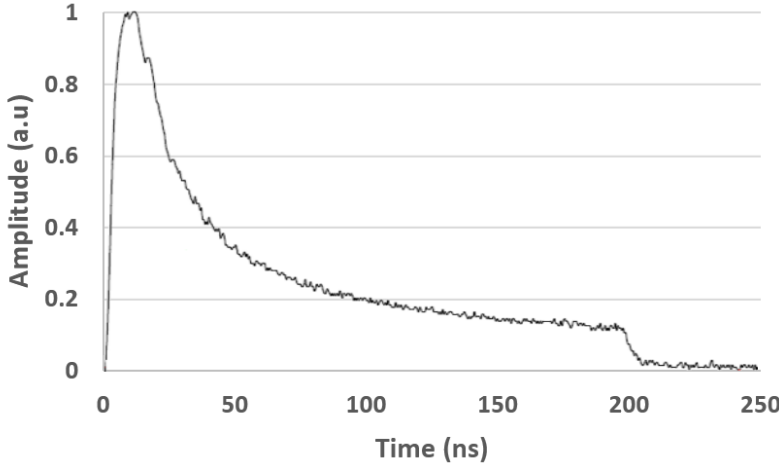
characterised by its abrupt phase change - from solid diamond to either plasma in the vapour phase, or non-ablated diamond to amorphous carbon/graphite in the solid phase - allows laser machining at low fluences without redeposition characteristics. INCONEL<sup>®</sup> 718, a Ni-based superalloy displaying more complex ablation mechanism characteristics due to the relatively protracted (liquid to solid) phase change of its constituents, was used in relevance to an industrial application where laser ablation of this material was likely to be employed.

Two lasers were used in this experiment. The first was an SPI G3.0, which had a maximum average output power of 20W and had a pulse duration range of 9 to 200ns, with a wavelength of 1064nm. It could be operated between 1 and 500 kHz. The beam quality had been classified as  $M^2 = 1.8$  by the manufacturer.

The second was an EWAG LaserLine, which had a maximum average output power of 50W and a pulse duration of 10ps. It had a wavelength of 1064nm operating between 50kHz – 8.2mHz, with a beam quality of  $<1.1$ . This laser was only used for calibration and validation of the model on CVD diamond material.

In order to validate the model, the logarithmic relationship (Eq. 4.1) between fluence and crater depth for the CVD diamond and INCONEL<sup>®</sup> 718 is needed. Experiments had been set up to create sets of craters on both materials with decreasing average power while keeping the rest of the dynamic and energetic parameters constant (no overlap between the pulses). For INCONEL<sup>®</sup> 718 power was decreased from 20 W down to 6.5 W in steps of 1.5 W, while for CVD diamond the same had been done from 20 W down to 12 W in steps of 2 W. The whole range of parameters can be found in Table 1. The pulse shape shown in table 1 was chosen for experiments as it gave the largest possible pulse energy (0.8mJ) from the laser thus allowing greater ablated depths per crater with the measurement itself having a better signal-to-noise ratio.

**Table 6 - Calibration (Single pulse) Trials Parameters**

Parameter	Value
Power	INCONEL <sup>®</sup> 718: 20-6.5 W (1.5 W increment) Diamond: 20-12 W (2 W increment)
Waveform	
Scan speed	2500 mm/s
Frequency	25 kHz
Off focus	0 mm
M2	1.8
Wavelength	1064± 2 nm
Spot diameter	39.5 μm

Using a white light interferometer (Bruker Contour GT) the INCONEL<sup>®</sup> 718 and CVD diamond craters were been measured and filtered. To increase the quality and usability of data harvested from experimental trials, two post-measurement operations were carried out. Removal of modal tilt was performed to rotate the measured surface, to a plane as flat as possible in the z direction. This did not change local values of the data (e.g. crater depths with respect to neighbouring surface); instead, all points on the data field are translated with respect to one-another to give a flatter surface. Data filtering was done utilising the built-in metrology software (Bruker Vision64) of the white light interferometer.

Figure 49a shows a 3-D trace of a selected crater after processing using a Gaussian filter, using band pass filter constants within the range (wavelength cut-off wavelength cut-off ranges  $0.015\text{mm} \pm 0.01$  to  $0.5\text{mm} \pm 0.4$ ) along with the sectional (X-Y profile) measurements of a single crater. Maximum crater depth and diameter were been measured to allow the calculation of the estimated fluence level of the pulse by taking a 2D cross section in the middle of a crater (in a plane orthogonal to the scan direction and workpiece surface). Due to the reflective nature of INCONEL® 718 the white light interferometer was deemed suitable to supply valid data (Figure 49b). In some cases, measurements on CVD diamond were done using a 3D profilometer (Talysurf CLi1000) due to its unreflective nature where excessive graphitisation was present.

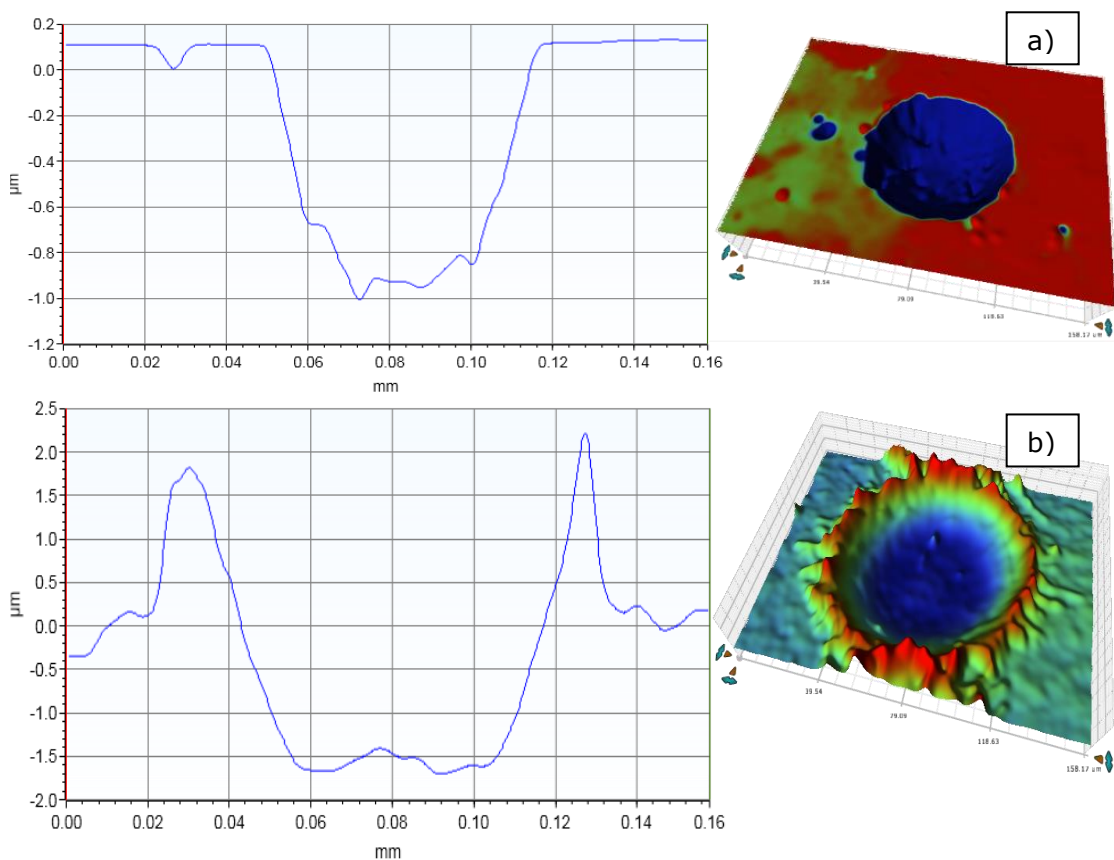


**Figure 49 – Example of filtered cross section profile of the 3D crater on a) CVD diamond and b) INCONEL® 718 craters ablated at  $31.5\text{J}/\text{cm}^2$**

**Table 7 - Validation parameters for trials on overlapping pulses**

<b>Parameter</b>	<b>Value</b>
Power (P)	16 Watt
Pulse duration	200ns
Scan speed ( $v_f$ )	1250-350 mm/s in steps of 100 mm/s
Frequency (f)	25 kHz
Off focus (z)	0 mm
Beam quality ( $M^2$ )	1.8
Wavelength	1064±2 nm
Spot diameter ( $\varphi_0$ )	39.5 $\mu$ m

To validate the capabilities of the model, tracks with progressively increasing overlapped craters were machined. Parameters used are listed in Table 7, and both materials were validated using the same parameter set. After applying the same measurement procedures as previously described, 2D cross-section of the tracks (i.e. overlapped craters) were created in the scan direction. The 2D cross-sections have been overlaid by the generated surface micro-geometry using the model. For the INCONEL<sup>®</sup> 718 trials the rim of redeposited material was included into the model using the established relationship following the methodology mentioned later, and shown in Figure 53. However, in the first step the predictions of the model were compared with the experimental results from the ablation of CVD diamond and in this way the model was validated by excluding the material redeposition phenomena. Then, considering the modelling of the redeposited rim, the overall modelling approach (ablation and redeposition) has been validated on INCONEL<sup>®</sup> 718.

Figure 50 shows an example set of craters ablated on INCONEL<sup>®</sup> 718 at a frequency of 25 kHz, and scan speeds of 950 mm/s (left), 1050mm/s (middle) and 1150 mm/s right). For an 80 $\mu$ m diameter crater these scan speeds correspond to crater overlaps of 47.5% (38 $\mu$ m), 52.5% (42 $\mu$ m), and 57.5% (46 $\mu$ m) respectively.

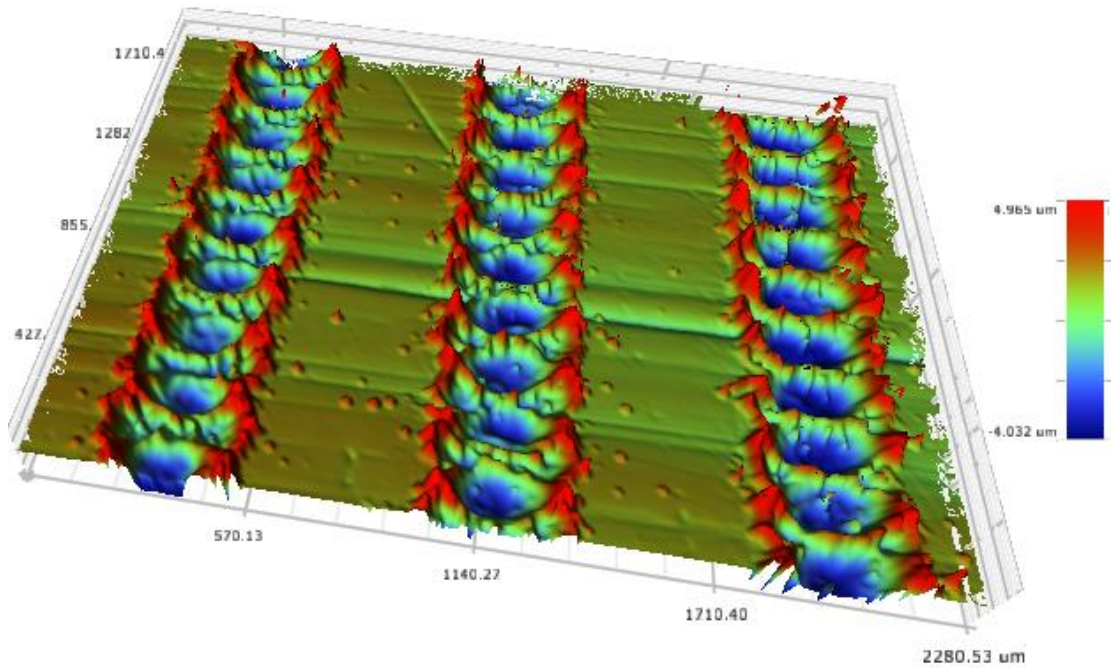


**Figure 50 – Example sets of overlapped craters ablated on INCONEL® 718.  $\Phi = 31.5$  J/cm<sup>2</sup>**

## 5.4 Mathematical model validation and discussion on ns and ps laser systems

A procedure was set up in order to capture and evaluate workpiece response to laser parameters to calibrate the model for the prediction of ablated surface profiles/textures. The procedure then extends to generate series of progressively overlapping craters. This is to evaluate the model’s predictive power on non-flat surfaces, by pulsing the laser partially on top of a crater generated from a previous pulse.

### 5.4.1 Experimental data for calibration of material response

#### 5.4.1.1 Material response equation

To set up the model for use and validation, calibration between laser energetic parameters and material response must first be carried out. This calibration determines values of the constants ‘a’ and ‘b’ used in Eq. 4.1.

This process was carried out for both materials; on diamond to assess the analytical part of the modelling approach where material redeposition is not present, and on INCONEL® 718 to demonstrate the model’s use on a commonly used ‘hard-to-machine’ materials.

Figure 51 shows calibration data used to define the logarithmic relationship, as described in the literature review, between normalised laser fluence and ablated depth (Eq. 4.1) on both materials. Figure 49a and b show examples of the craters used in calibration. Note that on a crater created in INCONEL<sup>®</sup> 718 (Figure 49b) redeposition is present whereas the crater created in CVD diamond (Figure 49a) there is no redeposition. Model calibration performed in the way described in this chapter only characterizes material response on a macro/micro scale. Material substructures such as crystal grains and/or other material phases, which may introduce different material response characteristics, are not considered. Therefore, errors may be present due to this at a typically sub-micron level.

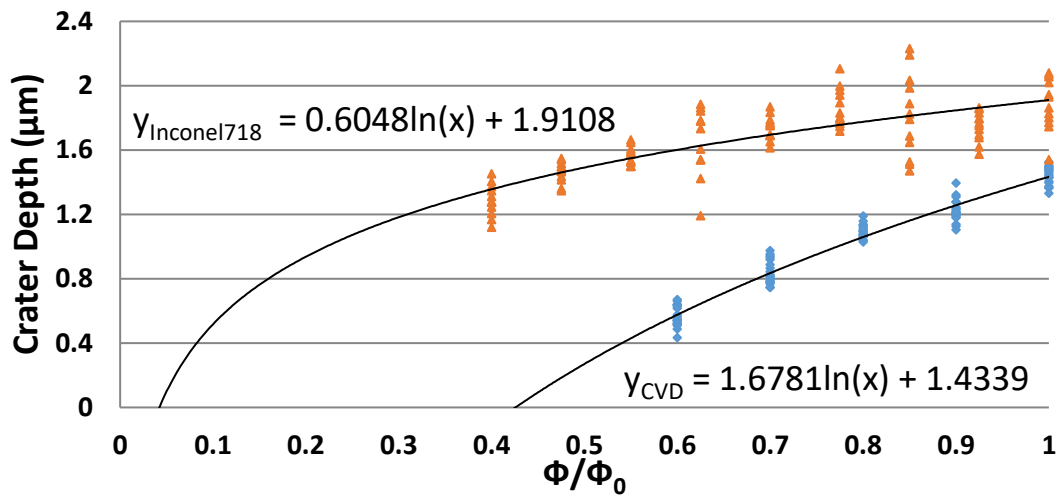


**Figure 51 – Calibration of response of CVD diamond and INCONEL<sup>®</sup> 718 workpieces to pulsed laser ablation ( $\Phi = 15\text{-}40 \text{ J/cm}^2$ )**

#### 5.4.1.2 Experimental characterisation of material redeposition

To approximate the profile of the redeposition the measurements shown in Figure 52 were used. This data was then used to fit a quadratic cross sectional rim around the crater. The height of the rim at any radial position  $r$  from the centre of the crater, for all positive values of  $h_{rim}$ , is given by;

$$h_{rim} = n(|r - c|)^2 + h_0 \quad (4.22)$$

Where;  $n$  is a shaping factor which will affect the steepness of the rim;  $c$  is the radial distance from the centre of the crater to the centre of the rim, and  $h_0$  is the observed average height of the rim. Following the methodology described at the end of section 3, a randomly oriented and rim with undulations imitating observations was generated. Each rim was given a randomised angular orientation with respect to the scan direction, and a nominal number of undulations to imitate observations. Undulations had maximum (grey triangles) and minimum (orange squares) heights between the limits shown in Figure 52a.

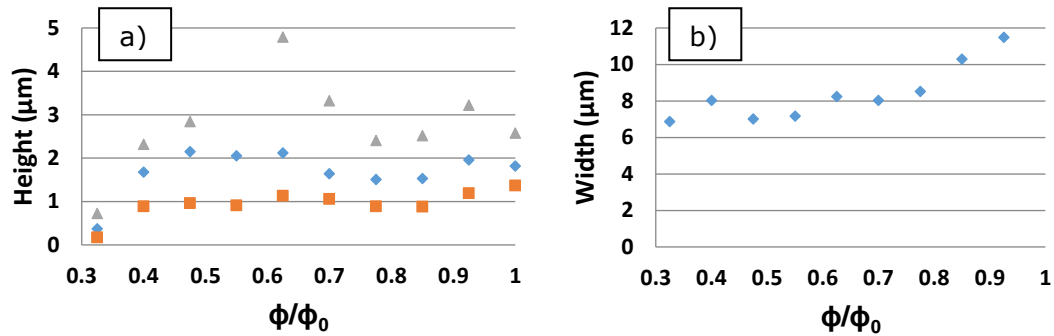


**Figure 52 - An example of the geometrical characteristics of material redeposition when laser ablating INCONEL® 718 ( $P \leq 20\text{W}$ ,  $f = 25\text{kHz}$ ,  $\tau = 200\text{ns}$ ): a) height, and b) width of the rim**

#### 5.4.1.3 Selection of craters and tracks for model validation for 200 nanosecond pulses

Model validation was carried out on a range of parameter sets, and presented in this section is validation for a laser power setting of 16 W at a pulse repetition frequency of 25kHz produced by the SPI G3.0 laser. Validation for the model was carried out both on tracks ablated in INCONEL® 718 and CVD polycrystalline diamond.

Figure 53 shows an example comparison of predicted vs. actual cross sections of crater lines. A maximum difference of 9.39% was found in the validation trials on CVD polycrystalline diamond (Figure 53a), with some differences as low as 0.72% for higher percentage overlap lines. Depth prediction showed good agreement with experimental results, and as such a successful validation of the model was performed for depth prediction. However, where redeposition was concerned, without an accurate multi-physics model in place large errors were observed. Redeposition of melt expulsion apparent in the laser ablation of some materials [28], [66], adds extra errors in surface prediction. Figure 53b-c shows the comparisons of cross sections taken from experimental data and a modelling prediction on INCONEL® 718 with and without redeposition included. To characterise the rim around the crater approximates were made from data harvested from the calibration trials, where redeposition is present and measurable

through the same methodology as crater depth measurements. Whilst this approach to approximate the redeposition effect in the process is a step forward, the randomised nature of its orientation does not guarantee accuracy. Therefore, the model is validated with no redeposition, on a material without redeposition when ablated (diamond). Prediction on CVD diamond was found to have an average error ranging from 0.72 to 9.29%. Similar predictions on INCONEL® 718 displayed average errors as low as 1.3% (over a set of 10 simulations with the same parameter set shown in Figure 53c). It should be noted that this error was variable due to the randomised nature of redeposition orientation during the simulation.

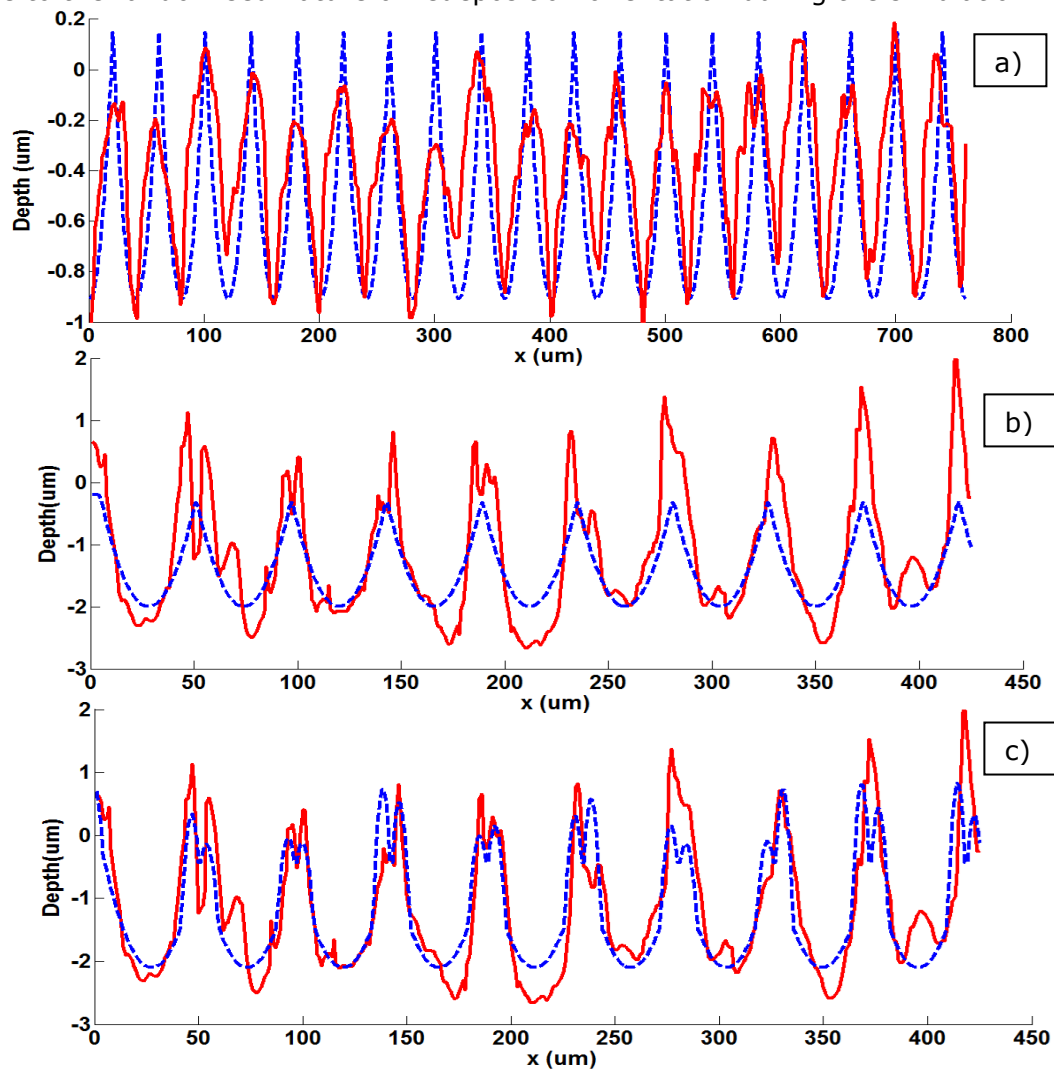


**Figure 53 – Comparison of simulated (dashed blue) and experimental (solid red) cross sections from lines of overlapped craters, where  $P=16W$ ,  $f=25$  kHz. a) CVD diamond,  $v_f = 800\text{mm/s}$ . b) INCONEL® 718,  $v_f = 1150\text{mm/s}$  (no redeposition modelling). c) INCONEL® 718,  $v_f = 1150\text{mm/s}$  (redeposition modelling included).**

## 5.5 MATLAB GUI for simulation of surface texture under PLA

To take this model to a higher level of utilisation, a MATLAB based simulation tool was written and built into a user-friendly GUI for simulation of PLA processes as shown in Figure 54. Categorical parameters are presented to the user and can be changed to simulate a wide range of pulsed laser ablation strategies, allowing versatile application of the model presented. Outputs of the GUI include various 3D micro-topographies of laser ablated surfaces starting from given initial surfaces. The process can be viewed pulse-by-pulse and any calculations can be saved in libraries, including all input parameters used for that simulation. 2D cross sections are given to further evaluate the output data.

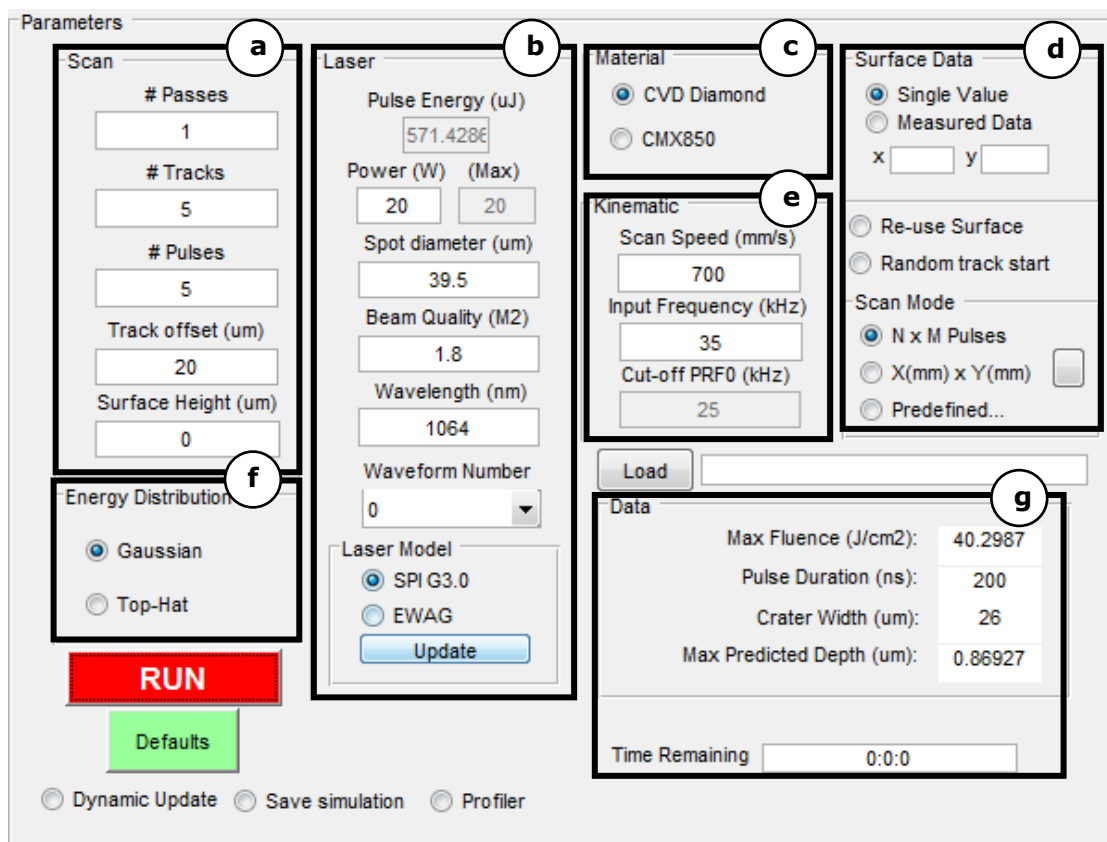


**Figure 54 – MATLAB computer simulation GUI and outputs; (a) Scan Parameters, (b) Laser Parameters, (c) Material Selection, (d) Initial Surface data settings, (e) Kinematic Parameters, (f) Energy Distribution Settings, (g) Output data field**

Nevertheless, apart from the errors stemming from random nature of the material redeposition phenomena and the inherent variability of craters, the following assumptions, to be dealt with by further research in situations to make them relevant, could also have an influence on the outcome of simulations:

- By assuming a Gaussian energy distribution the intensity of the beam at a radial position 'r' may be a source of error. This will manifest most noticeably when craters are overlapped and ablated depths calculated from incorrect intensities are summed cumulatively over a larger number of overlapping pulses.
- Through assuming instantaneous ablation the effects of kinematics on crater dimensions and form are affected. However, at machined process parameters likely to be used for a real process e.g. scan speed 1000 mm/s this source of error is negligible.

Figure 55a shows a simulated ablated surface, with a cross section of the ablated surface shown in Figure 55b.

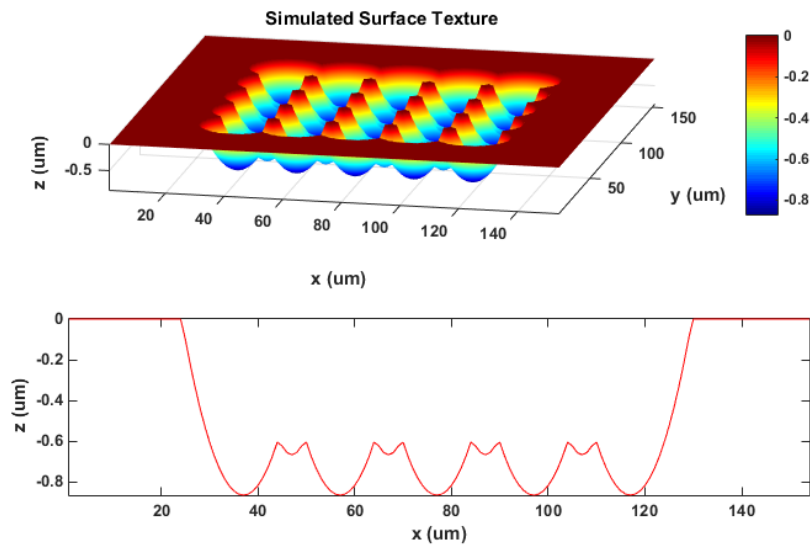


**Figure 55 - Simulated ablated surface shown in a) 3D and b) cross section**

## 5.6 Optimised parameters selection

Selection of KPVs to produce a blend with minimal recast was done by considering the effects of each KPV, in an order described in Chapter 3. Figure 56 shows how recast layer thickness measured in Chapter 3 (shown in Table 5) varies with pulse energy and material removal rate, at different power settings (shown by dotted lines). Estimated material removal rate was calculated using a mathematical MATLAB based modelling technique, validated on INCONEL® 718 [69]. Therefore, the highest possible material removal rate could be chosen where the lowest possible recast occurs. In this case, it can be seen to occur at a pulse energy of  $\sim 0.6$  mJ, where the power setting is 15W and the pulse repetition frequency is 25kHz.

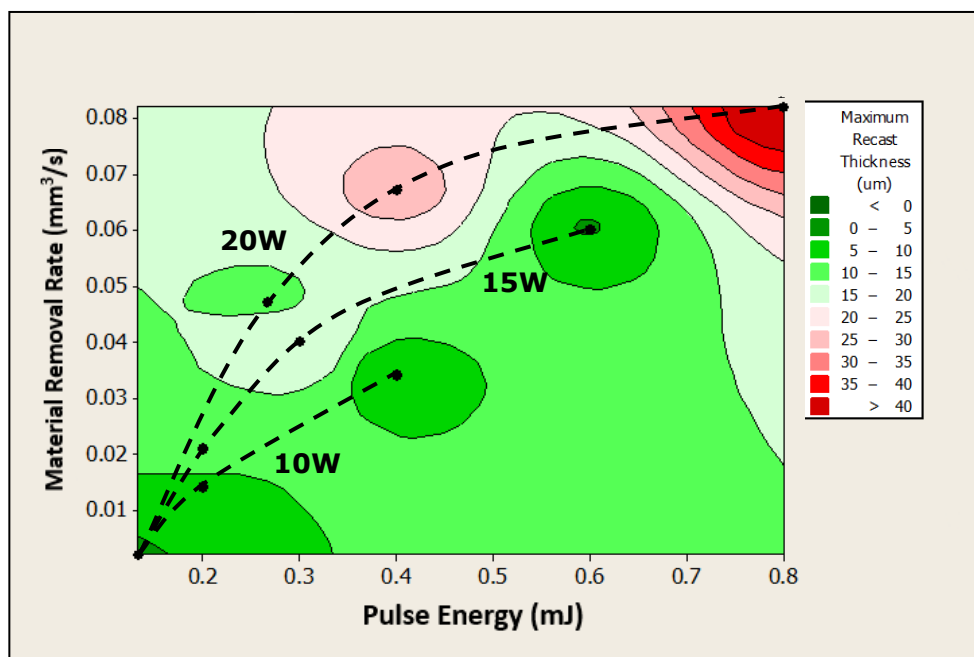


**Figure 56 - Contour plot of maximum recast thickness against material removal rate and pulse energy**

Once a pulse energy and power have been chosen to produce minimal recast thickness, a frequency must be selected. Figure 57a shows the frequency that must be used to produce pulse energies at a given power level. In tandem with selection of the frequency, an appropriate scan speed can also be determined. Figure 57b shows how recast thickness will vary with scan speed at a given predetermined pulse energy. As there is minimal variation in recast thickness when changing scan speed, other than for high pulse energies as can be seen, this KPV can be selected in accordance with process quality aims such as surface roughness.

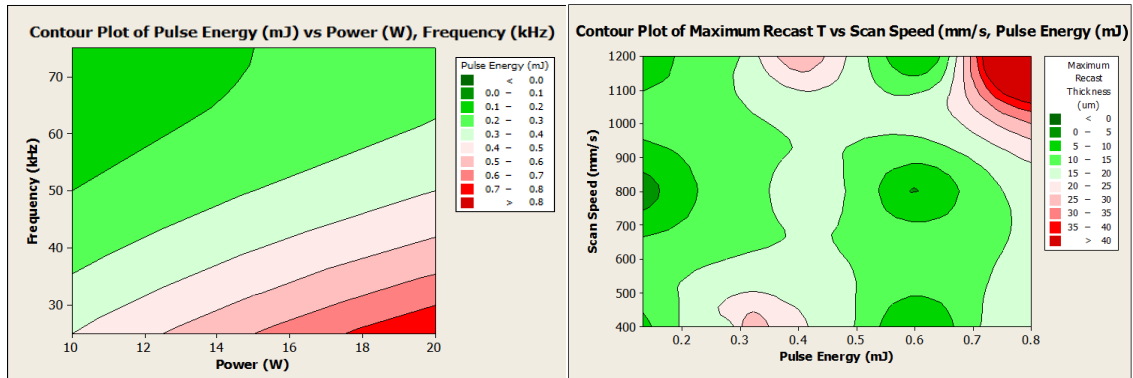


Figure 57 - a) Frequency (left) and b) Scan Speed (right) selection charts

Figure 58 shows a simple flow chart for selection of optimised parameters, based upon desired material removal rates and recast thicknesses. It also takes into account any topographical requirements for the blend surface such as roughness or undulations, which will affect the scan speed selection.

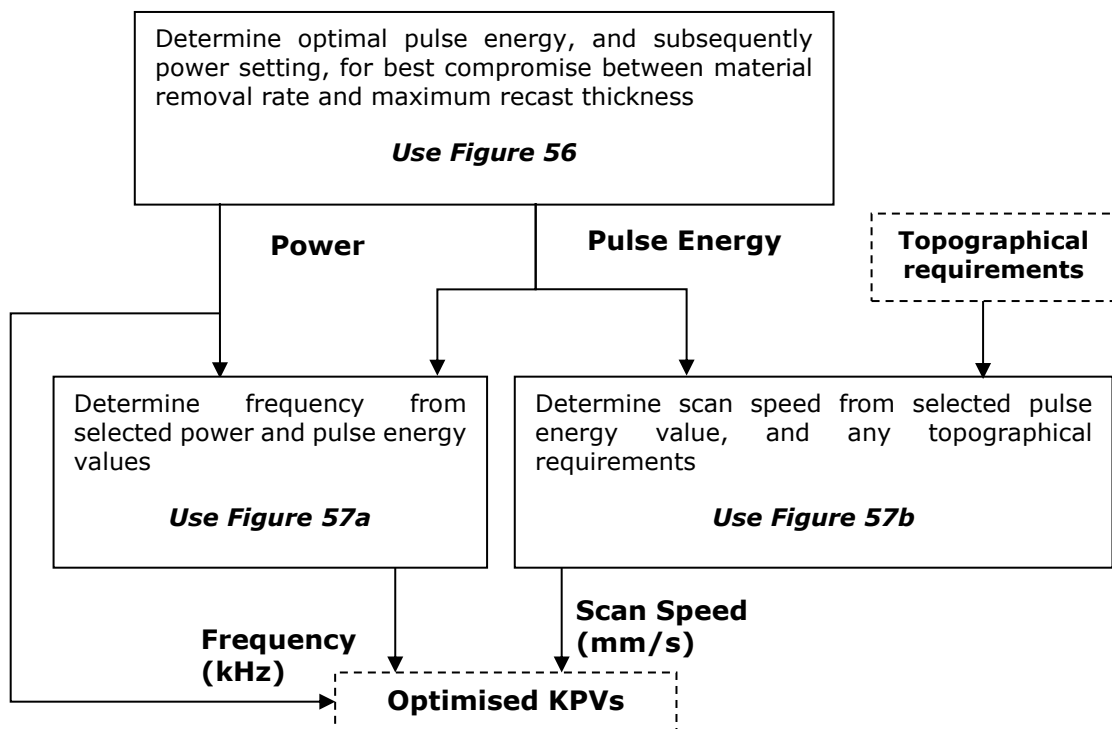


Figure 58 - Flow chart for parameter selection

## 5.7 Summary

The model developed and described in this chapter has shown good predictive capabilities for surface topography modelling in two materials, using two laser systems. Through initial calibration between a chosen material and laser system, a logarithmic dependency between laser machining parameters and depth of material ablation was established. Additional work was also carried out to provide some

predictive capabilities in situations where material redeposition was present in INCONEL® 718 ablation with nanosecond pulse durations.

The following validation exercises were carried out on results using the SPI G3.0 laser system (200ns pulse duration);

- CVD diamond targets with no material redeposition
- INCONEL® 718 targets with no material redeposition
- INCONEL® 718 targets with material redeposition

The model presented good accuracy on predicting topographies in the above scenarios, however irregular errors were seen in modelling INCONEL® 718 targets with no redeposition. As such the third scenario was included for validation, taking into account this material redeposition. Errors when predicting ablated surface height on CVD diamond modelling were equal to or less than 9.39%, and 1.3% for INCONEL® 718 targets where redeposition was included.

The technique used for modelling redeposition on INCONEL® 718 had limitations for complex or deep features, as accurate prediction of material redeposition is difficult without a comprehensive multi-physics approach. As such, further work was required to properly evaluate the model's predictive capabilities on INCONEL® 718 ablation in scenarios with complex or large features.

By using the model to predict material removal rates (based upon modelled feature volumes) and estimating process times from the values of each process variables, process optimisation can be performed when combined with metallurgical results obtained in Chapter 3. It was found relatively high material removal rates ( $0.06\text{mm}^3/\text{s}$  out of a simulated maximum of  $0.08\text{mm}^3/\text{s}$ ) was achieved whilst also generating minimal amounts of material recast when using a laser power of 15W, pulse frequency of 25kHz, and a scan speed of 400mm/s.

This model has shown that given appropriate laser-material calibration, an accurate prediction of surface topography can be made in terms of volume of material removed. Furthermore when this model is used alongside metallurgical data across a range of laser parameters for the given laser and material selection, some process optimisation can also be achieved to improve process times whilst reducing negative metallurgical effects.

# Chapter 6. Micro and Macro Scale Validation for Mathematical Modelling

## 6.1 Validation of mathematical model

The model presented in Chapter 3 gives accurate prediction of laser ablated surfaces where laser power, pulse frequency and scanning speed are varied. Both scenarios where no material redeposition is present (CVD diamond target) and material redeposition is considered (INCONEL® 718 target) were modelled with good accuracy. However, the model had limitations when modelling material redeposition on the micro scale with INCONEL® 718 targets given the difficulties of modelling this redeposition accurately in a scientific manner. Due to this limitation, model validation on INCONEL® 718 was performed on much larger macro-scale features, where the effect of material redeposition on the overall volume of removed material was lower and accurate mass removal predictions are feasible. Additionally, further micro-scale validation was performed to validate the model's predictive capabilities on complex geometries. This involved CVD diamond ablation using picosecond pulse durations, in features with multiple scan passes and varied scan track offsets.

Use of a femtosecond laser would allow for validation of the model against INCONEL® 718 on small geometries with complex features, as no material redeposition is seen when ablating this material with such short pulses. Without this equipment complex micro-feature geometry validation is limited to diamond targets ablated using picosecond ablation.

Given these extra validation requirements the following experiments were proposed to further assess the model's predictive capabilities;

- Complex micro feature generation using a picosecond duration pulsed laser ablation on CVD diamond targets where in addition to varying laser power, frequency and scan speed, laser scan path repetitions (passes) and laser scan track offsets are also varied.
- Large macro feature generation using nanosecond duration pulsed laser ablation on INCONEL® 718 targets, where target mass removal is performed as part of an On-The-Fly balancing process. This will not consider the

topography of the ablated features, but instead the overall dimensions (and hence mass) of the removed material.

## 6.2 Validation requirements for Chapter 5 Model

The mathematical model for the prediction of surface topography under pulsed laser ablation presented in Chapter 5 has shown accuracy in calculating the depth of ablated craters in INCONEL® 718. This model has predictive power when considering a known material and laser ablation system when initial calibration work is performed.

In order to make use of the model it must be shown that it has predictive power beyond simple crater depth prediction; where pulse overlap, track step-over, and number of scan passes are all varied. This must include more complex feature generation in the micro-scale, and larger features where mass removal is a consideration. Therefore, in addition to the initial validation performed in Chapter 5 on both diamond and INCONEL® targets using a nanosecond laser, further model validation was carried out with a picosecond laser and a diamond target material for micro-features, and macro geometry validation using a nanosecond laser on an INCONEL® target. As discussed in Chapter 5, diamond does not present the same recast characteristics that metals do when ablated using pulsed lasers. Therefore, diamond is an ideal material to validate the mathematical model with as it does not introduce secondary effects which further complicates modelling and validation on the micro scale. These effects are less impactful when simply removing a target mass from a component, and as such macro scale validation was carried out on an INCONEL® 718 target.

As the ablated topographies seen in Chapter 5 are not entirely uniform or consistent, understanding and methods are also developed to filter and characterise measured ablated surfaces. In creating incremental stages of validation, confidence in the mathematical model's predictive power can be gained and it can be used to predict resultant topographies or more complex features generated using a known laser system and target material.

An additional MATLAB programme and user interface was created to automatically import, filter and compare measured laser ablated samples with predicted topographies in accordance with known key process variables (power, frequency, scan speed).

## 6.3 Methodology for Micro-Scale feature validation on CVD

### Diamond targets

#### 6.3.1 Ablation Trial 1 - Mathematical Model Calibration

Calibration was done by the same methods as those used in Chapter 5, where material response in terms of ablation depth was measured over a range of pulse energies. This stage's purpose is to provide a foundation upon which to generate predictions of material topographies for comparison against measured data.

Figure 59 shows the layout of the CVD diamond sample and test craters ablated upon it.

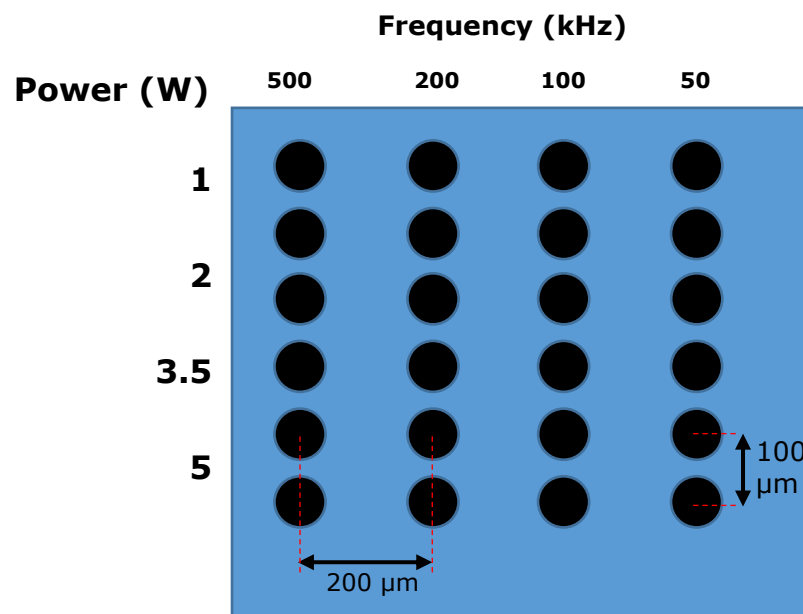


**Figure 59 - Ablation pattern for calibration of mathematical model**

Each crater was ablated by 50 pulses to obtain an accurate average depth per pulse. Each pulse was created with the sample and laser machine stage being held static. The sample was moved by fixed increments in the X and Y plane (200 $\mu$ m and 100 $\mu$ m respectively) to ensure no interaction between neighbouring pulses. To obtain exactly 50 pulses, an external gating module was used to block laser control signals and only allow them through for a pre-defined window of time, calculated by the reciprocal of the pulse repetition frequency such that during the gate opening time, 50 separate pulse signals would have been let through the control module. The pulse energies used in this experiment ranged from 2 $\mu$ J (1W @ 500kHz) to 160  $\mu$ J (8W @ 50kHz), and the entire experiment was conducted twice to gain more data for accuracy of results. The laser system used to generate the pulses was an EWAG Laserline, with a 10picosecond pulse duration. Fluence values used in this

experiment can be calculated by dividing area of the laser beam spot at focus by the pulse energy used.

### 6.3.2 Ablation Trials 2 & 3 – Mathematical Model Validation

Two trials were carried out for validation of the model calibration performed in trial 1. Each trial took one parameter set from the previous trial and extends it with further considerations:

- Trial 2 – Varied crater overlap; 70%, 80%, 85%, 90%, 95%, where overlap is a percentage of crater measured crater diameter. Pulse energy was kept at a constant  $53\mu\text{J}$ . Pulse repetition frequency kept at a constant 100 kHz, scan speed was varied (1080, 720, 540, 360, 180mm/s) to achieve differing degrees of crater overlap.
- Trial 3 – Varied track step over; 10%, 50%, 90%. Pulse energy, repetition frequency, and scan speed were all kept constant resulting in a 90% crater overlap (100 kHz @ 360mm/s).

Figure 60 shows the ablation patterns used for the validation trials 2 and 3. Similarly to the ablation carried out for calibration, each of trial 2 and 3 scan paths were repeated 50 times to allow calculation of an accurate average depth per pass (repetition).

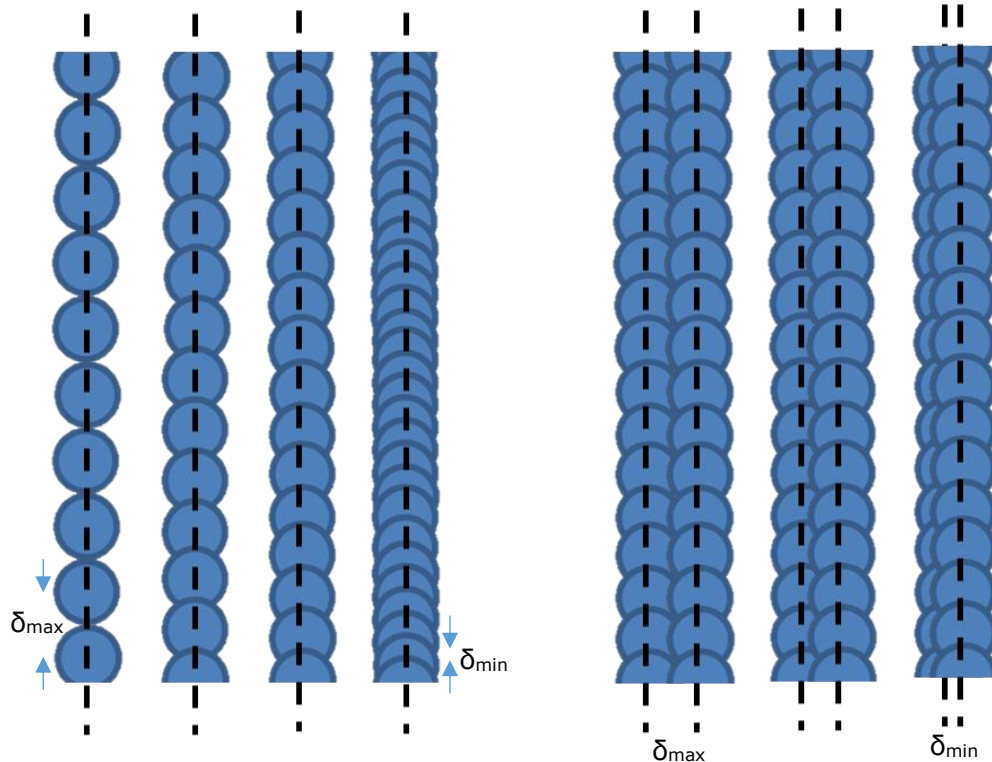


Figure 60 – Representative ablation scan paths for a) Trial 2 and b) Trial 3

### 6.3.3 Measurement of ablated samples

Ablated samples created in trials 1, 2 and 3 were measured using white light interferometry, performed on a Bruker Contour GT. Samples were cleaned with an air duster and placed underneath the measurement lens of the machine. Samples were tilted to be as flat as possible with respect to the focal plane of the measurement equipment. Minimal data filtering and modification was performed within the Bruker software, as any necessary data operations were carried out within the custom made MATLAB script. This was done as to avoid introducing any unknown or ambiguous operations to the data handling process that may affect results.

### 6.3.4 Data import and handling

Data from measured surfaces of ablated samples was imported into MATLAB as XYZ triplets, with units of  $\mu\text{m}$ . Figure 61 shows the layout of the MATLAB tool used in this validation exercise. The features and functions of each of the four subsections labelled in Figure 61 are explained in further detail in the following sections.

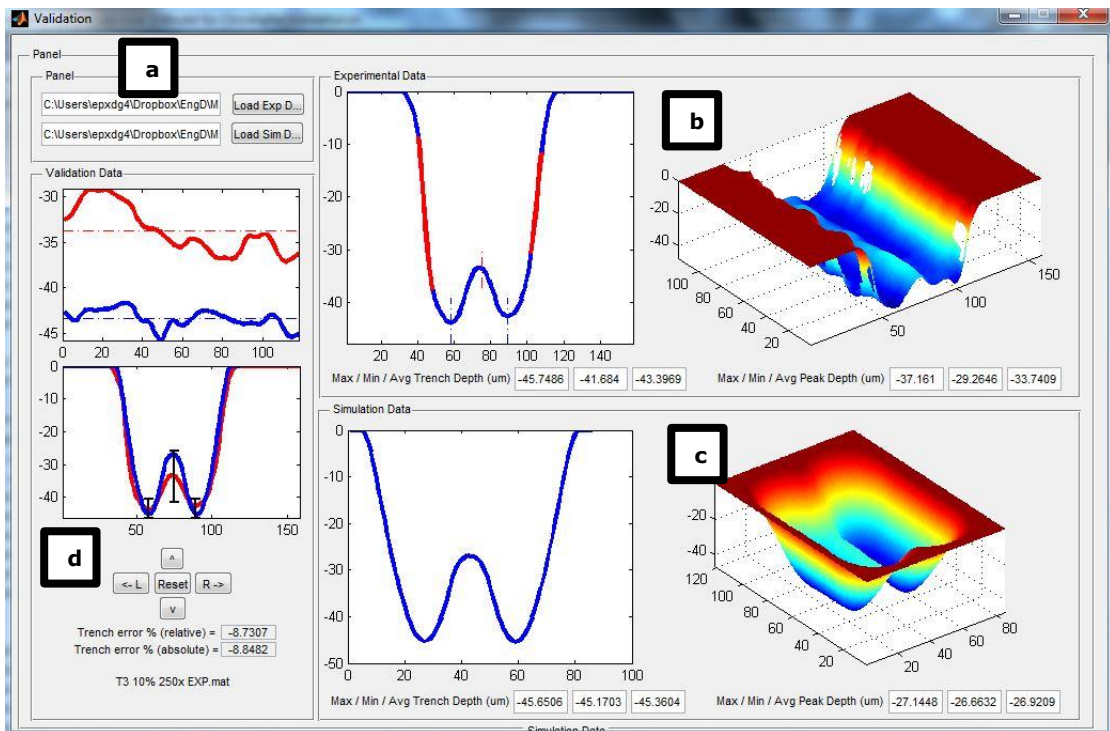


Figure 61 - MATLAB Validation GUI

#### a) Experimental / Simulation data Import

Buttons for loading experimental and simulation data sets. These data sets are in the format of XYZ triplets, and in both cases are automatically translated into 3D surfaces (shown in sections b and c of Figure 61).

## b) Experimental data graphs

2D Plot (left) showing an average cross section of the 3D data (averaged along the direction of the laser beam scan). Non-filtered parts of the section are shown in blue, and filtered parts are shown in red. A 3D plot of the surface is also shown in the right side of section b. Data points in the cross section are either coloured red or blue, dependent on the data in the complete 3D scan.

- Blue data points (non-filtered data): Each row in the 3D data array (slice taken **perpendicular** to scan direction) is summed, and divided by the number of rows.
- Red data points (filtered data): Each column (slice taken **parallel** to scan direction) is summed, and divided by the number of 'real' (non-NaN) values in the column. Each 'filtered' column is then assembled into a single 1 x n array (n = number of columns), giving a 'filtered' cross section of the trench. This allows the in-filling of data points where there is not a complete set of data for the column (line parallel to scan direction) in the measured data.

Both experimental and simulated data contain an  $m \times n$  array of surface height (z) data in micron. The array sizing is also in micron, where the number of rows and columns is equivalent to the length and width of the surface in question (in micron). An average cross section of a track's 3D data is calculated by summing the  $i^{\text{th}}$  element of each column, and dividing by the number of rows.

This process is necessary to ensure that the cross section taken across (perpendicular) to the track is representative of the results of the ablation process and its parameters, regardless of where the section is taken. Given the undulating nature of the track topography at its centre, averaging of the data must be used.

Figure 62 shows an example of a track centre cross section, where isolated maxima and minima may be found (either through physical process which are not accounted for, or through measurement anomalies). Should perpendicular cross sections of the path be taken at these points, the resulting depth and volume of ablation would not be representative of the actual ablated trench. As such, an average depth (dotted red line) is used to calculate depth and volume of ablation.

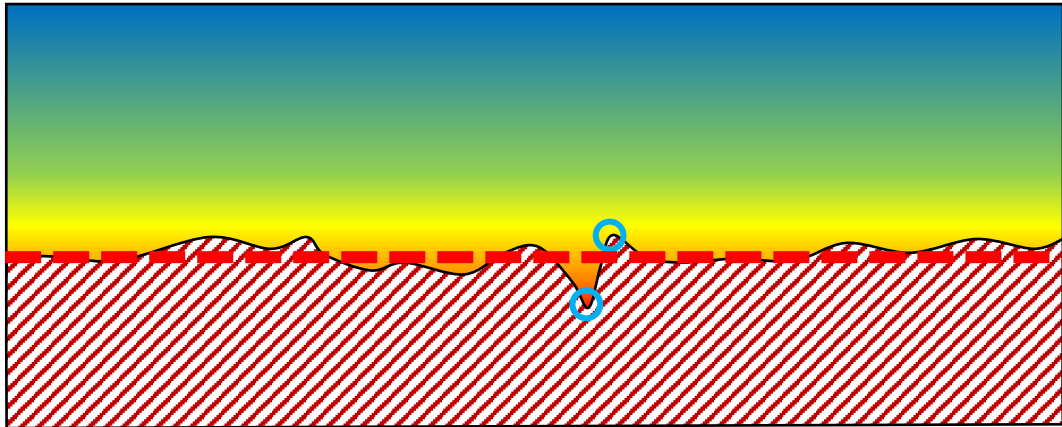


**Figure 62 - Track cross section in direction of scan**

Figure 63a shows a 3D array before averaging, with columns 1 to n being averaged as shown in the array shown in Figure 63b. If there are any 'NaN' values in the 3D array, where bad measurements have taken place resulting in voids in the data, these indices are not included in any averaging of the data. For example, if there are 100 elements in the n<sup>th</sup> column, and 10 elements have no z value assigned due to bad measurement, the average z value in that column will be calculated by;

$$z_{avg} = \frac{\sum_1^n z}{(100-10)} \quad (5.1)$$

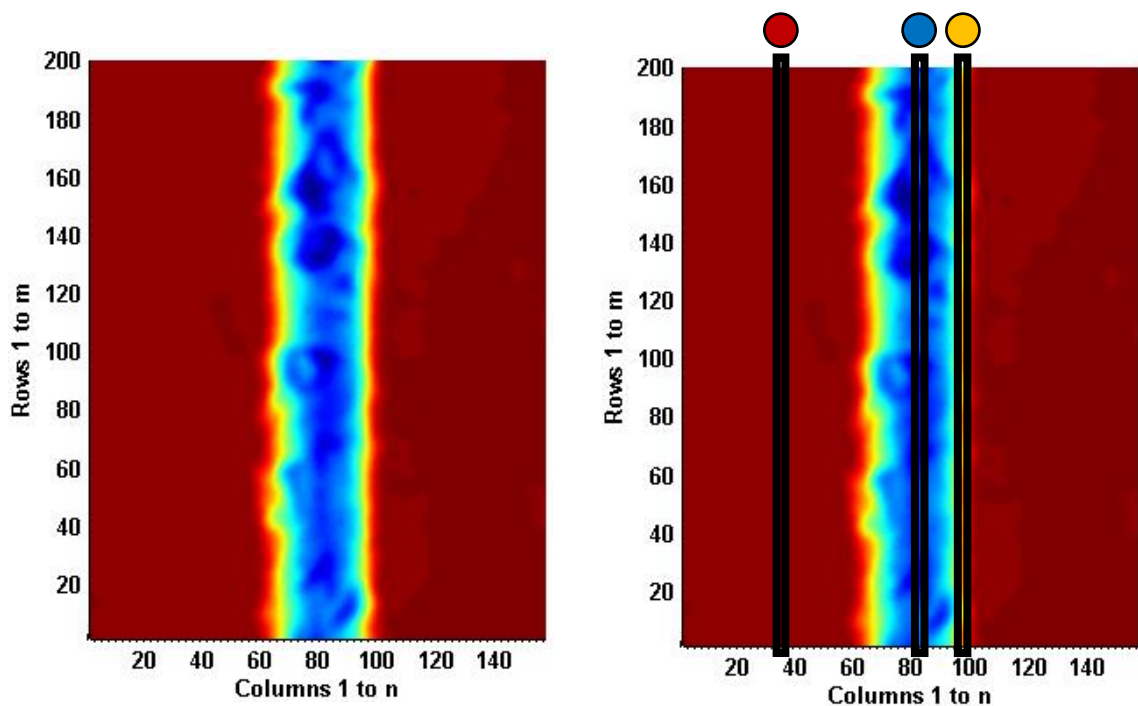


**Figure 63 – a) 90% overlapped pulses track data before averaging, b) Columnar averaging along direction of scanning, shown by colour**

Figure 64 shows a comparison between an averaged experimental track (left) having been processed by methods explained previously, and a raw simulated track (right) of the same dimensions.

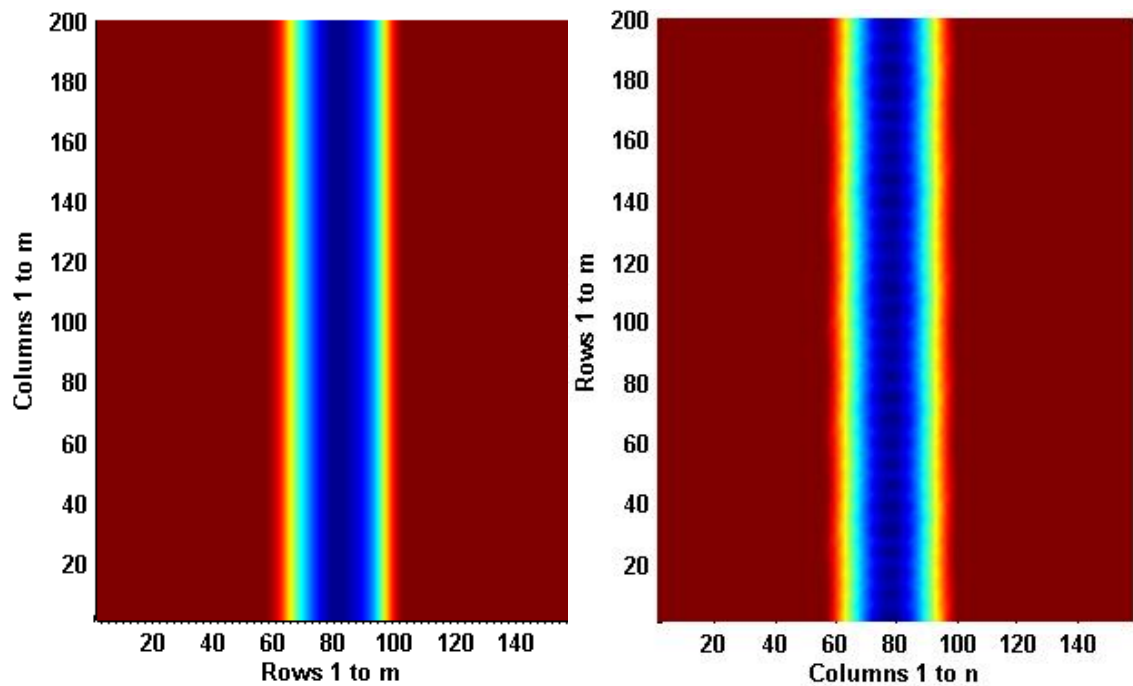


**Figure 64 – a) Averaged experimental data, b) Simulated data for 90% overlapped pulses**

Both datasets are constructed such that the track is positioned close to the centre of the array (in the x direction) and runs as parallel as possible to the y direction. For simulated data, both of these are easy to achieve as the track can be placed wherever it is required within the simulation field. However, for experimentally captured data, whilst the array can be trimmed to place the track centrally in the x direction, the degree to which the track is truly parallel within the dataset depends on how well aligned the experimental sample is placed within the measurement equipment before data capture. There has been no correction of any datasets taken with regards to verticality (how parallel the track is to the y direction), as measurement methodologies resulted in very good datasets in this regard as can be seen in Figure 64a. It is worth noting however that any angular deviation from the y direction that the track makes from misalignment during measurement, will result in the average track cross section to be wider and shallower than the true average. This is due to the averaging of the rows in the 3D array in the y direction, not in a direction parallel to the track itself which would be mathematically and computationally more demanding. A cross section of each of these tracks is taken for use in subsequent validation processes by simply extracting the first row of data (as all rows are now identical).

### c) Simulated data graphs

Within section c of Figure 61, the 2D plot (left) showing cross section at mid-point of 3D array (no averaging of trench necessary due to much more uniform profile). 3D surface plot (right) showing predicted surface. There is no need for data filtering in this section as the surface is generated mathematically and each location in the 3D data array is specifically calculated.

No averaging process as described in section 0 is used on simulated data. This is valid for high-overlap between subsequent pulses, as there are only small undulations in the track depth. However, for low-overlap, average depth should be employed, or a different comparison technique between simulated and experimental tracks should be used.

### d) Validation of simulated surface data against measured surface data

After being imported and filtered, peak and trench locations are detected within both simulated and measured surface data. Cross sections of the trenches at the position of peaks and troughs are extracted along the scan direction. The mean value, and standard deviation of these profiles are calculated and used to display  $\pm 3$  sigma bounds around the mean value of the peaks/trenches in a section. The identification of peaks and troughs in the 3D data is done as follows;

- Identify the lowest z height in the averaged cross section of the experimental track.
- Determine whether there is a single valley, or 2 valleys and a peak
  - If the lowest value's index (position along the x axis) is close to halfway across the axis, then there is likely to be only one valley. If not, there are likely to be two valleys and a peak
  - If the latter is the case, determine the location of the peak. This is done by finding the highest z value within a certain range of the previously identified valley location.
  - If the valley is located 30 $\mu$ m to the left of the centre of the x axis, then the peak will be defined as the highest point within the range  $X_{\text{valley}}$  to  $(X_{\text{valley}} + 60)$ , where one would expect to find the second valley.

- Lastly, the true location of the second valley is located as the lowest z value in the opposite direction from the centre of the track to the direction of the first valley.

Profiles for the scan cross sections at the locations of the trenches and peaks is extracted (i.e. columns at x locations corresponding to maxima/minima within the ablated track). These profiles are displayed in Figure 61d at the top of the UI panel labelled "Validation Data", where red lines correspond to peak profiles and blue lines correspond to trench profiles. Additionally, mean depths for these profiles are overlaid as dotted lines on the relevant sections.

A cross section overlay (Figure 61d, bottom) shows filtered experimental data (red) and predicted data (blue) cross sections. Included are  $\pm 3$  sigma bounds around the mean experimental peak/trench depths, shown with black bars.

There are 4-way 'nudge' buttons with reset option to move the simulated (blue) section relative to the experimental section (red) for alignment, however most of the alignment is done during the main validation script.

Volumetric trench errors are shown for the difference between the 1um thick (remembering that the averaged cross section is really an averaged 1um slice along the length of the trench) cross sections.

- Relative error is the percentage difference between the sum of all the elements in each array. By summing all of the elements in an array, a rough estimate of the 'volume' of that 1um slice is obtained (effectively integrating the 'curve' of the section). Relative error will sum an array that has been 'nudged' up or down by taking the 'nudged' depth values. This is important to take note of, as a section that has been moved upwards by a significant amount may have a 'zero' volume, as elements above zero have a 'positive' height, and those below have a 'negative height', which when summed will cancel out.
- For means of comparison, absolute volume is used, where the volume considered is independent of 'nudge' amounts, i.e. no matter where the sections are relative to each other, each is summed as if its maximum values were zero and every other value in the array was measured from zero.

An example of the validation carried out with this MATLAB tool is shown in Figure 65, with a high degree of accuracy both in terms of percentage error and a qualitative comparison. In the 2D plot for simulated data there are obvious

“shoulders” either side of the maximum depth of the cross section. These shoulders are also present in the simulated cross section directly below.

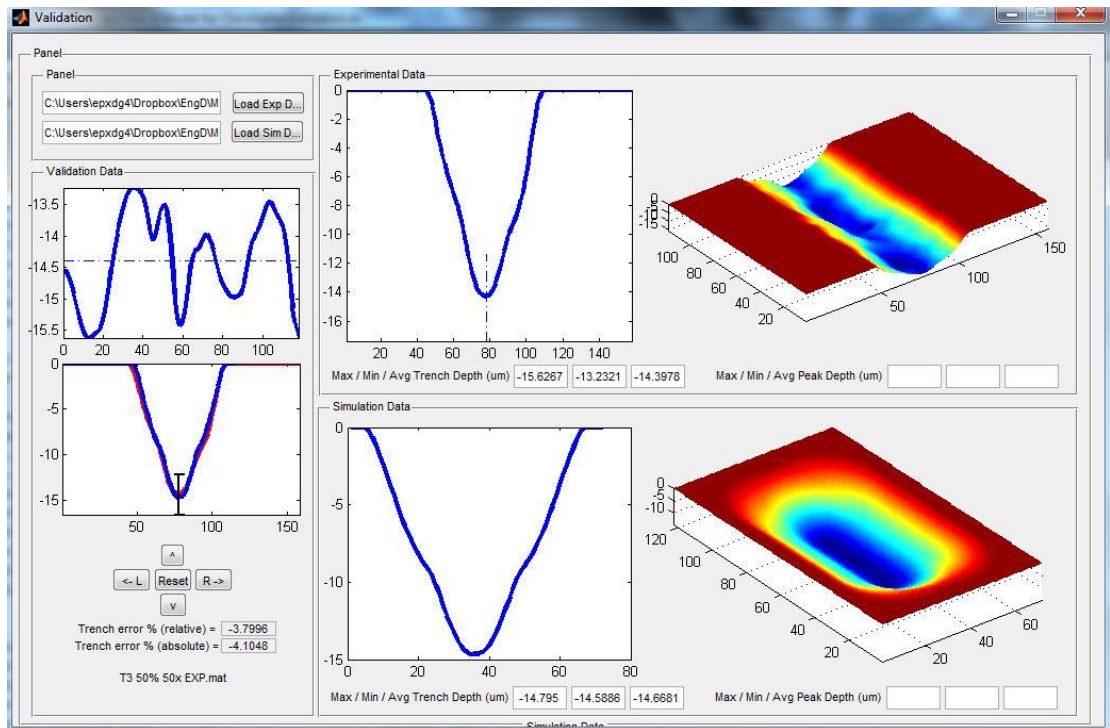
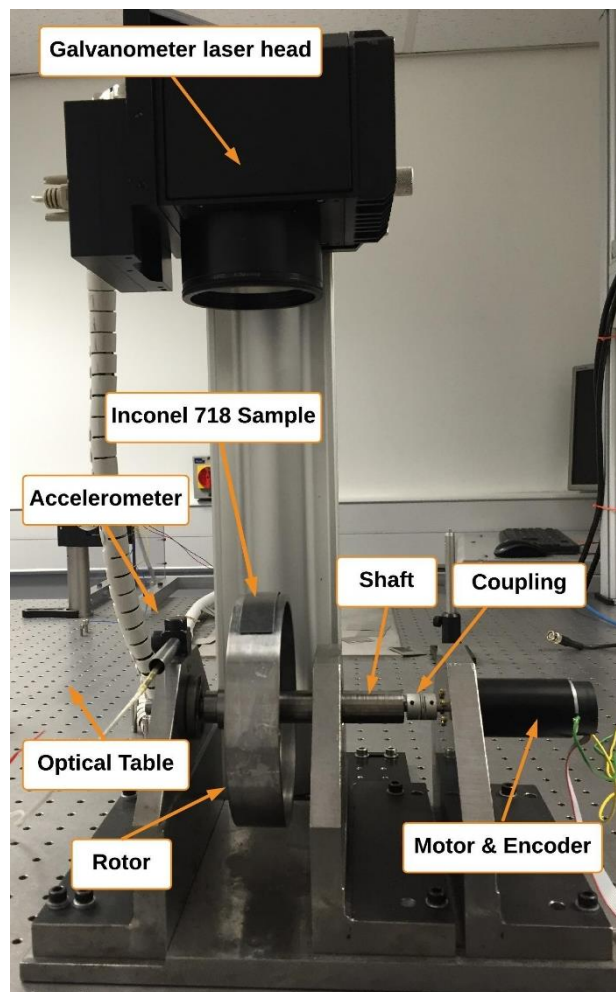


Figure 65 - Example of high accuracy of simulated surface data when compared with experimental data (Trial 3, 50% Track overlap, 50 passes)

## 6.4 Methodology for Macro-Scale feature validation on INCONEL® 718 targets

In order to demonstrate the value of the model proposed in Chapter 5, a validation exercise was carried out on laser machining of components being balanced on-the-fly. Rotating components were given an imbalance at a known location, and automated imbalance detection and removal was applied. Imbalance detection was performed using axial accelerometers, which were read in real-time alongside rotary encoders measuring component rotation. Once imbalance locations were determined, laser pulsing was initiated to remove material from the location, reducing the overall imbalance. This set-up is shown in Figure 66.



**Figure 66 - Imbalance detection and removal set-up [70]**

Imbalance machining was a 2 stage process, where machining parameters were first calculated using the mathematical model from Chapter 5. After these parameters had been determined, imbalance removal was performed. An artificial neural network training program was used to take input data including material properties, laser-material interaction calibration data, target mass removal and

more, and then output a set of processing parameter values; laser power (P), frequency (f), pulse spacing ( $d_{x,y}$ ) and scan passes ( $n_z$ ). An in depth explanation of this process is given in a published report on this work [70].

Figure 67 shows a summary of this process through a flowchart. After inputting mass removal and machined geometry size targets ( $D_x$ ,  $D_y$ ) an iterative process is used to determine optimal machine parameter values; f, P,  $n_z$ ,  $d_{x,y}$ . These values are used to simulate machined geometries using the mathematical model in Chapter 5, and then estimated machining times required to reach the target mass removal are outputted.

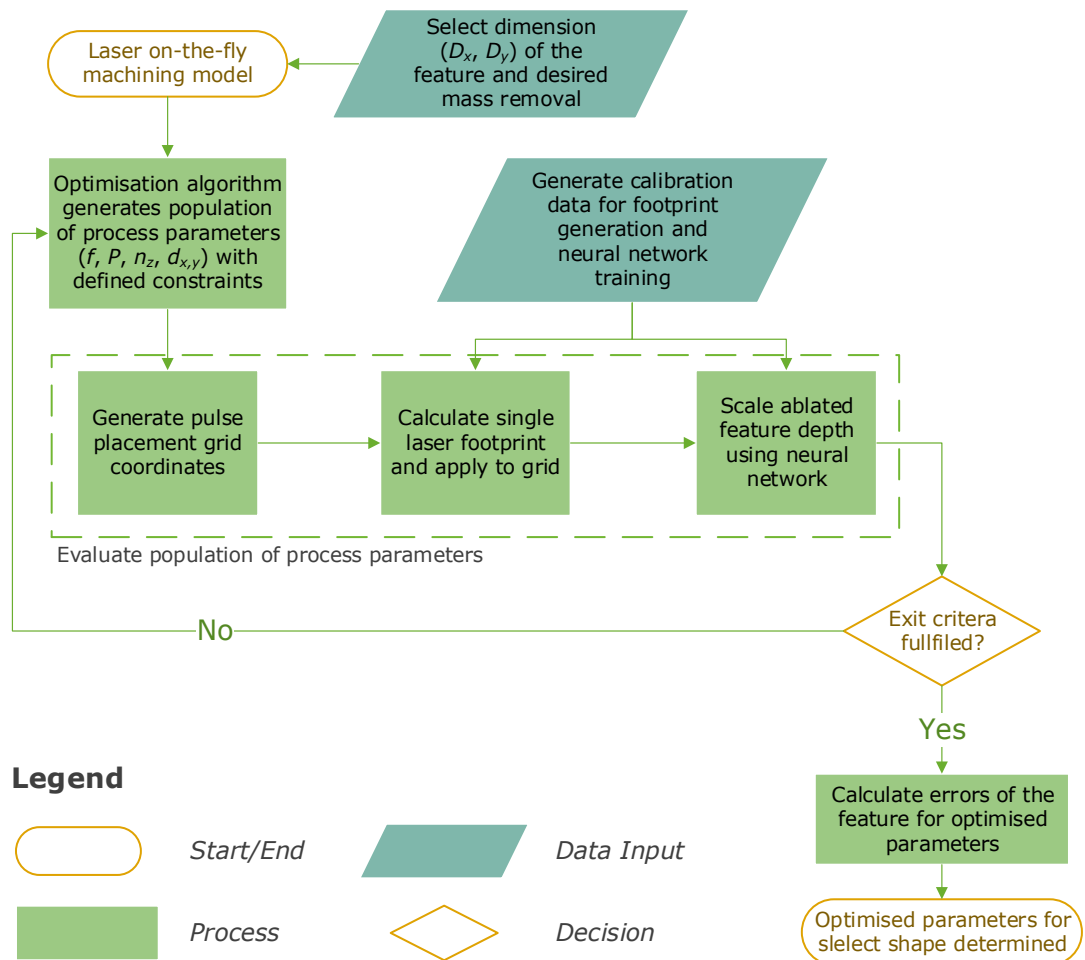


**Figure 67 - Flowchart for generating process parameters [70]**

As this validation exercise was carried out on rotating components, the amount of time spent ablating the INCONEL® sample was a fraction of the total process time. This was due to the fact that ablation of the sample is possible for only a part of each component revolution. Given that machining time was a consideration when determining optimal process parameters, maximising the ablation time per

revolution of the component was considered. To assess the importance of this effect, geometries that offered both “high” and “low” ablation time per revolution were generated. These are shown in Figure 68 as features A and B respectively.

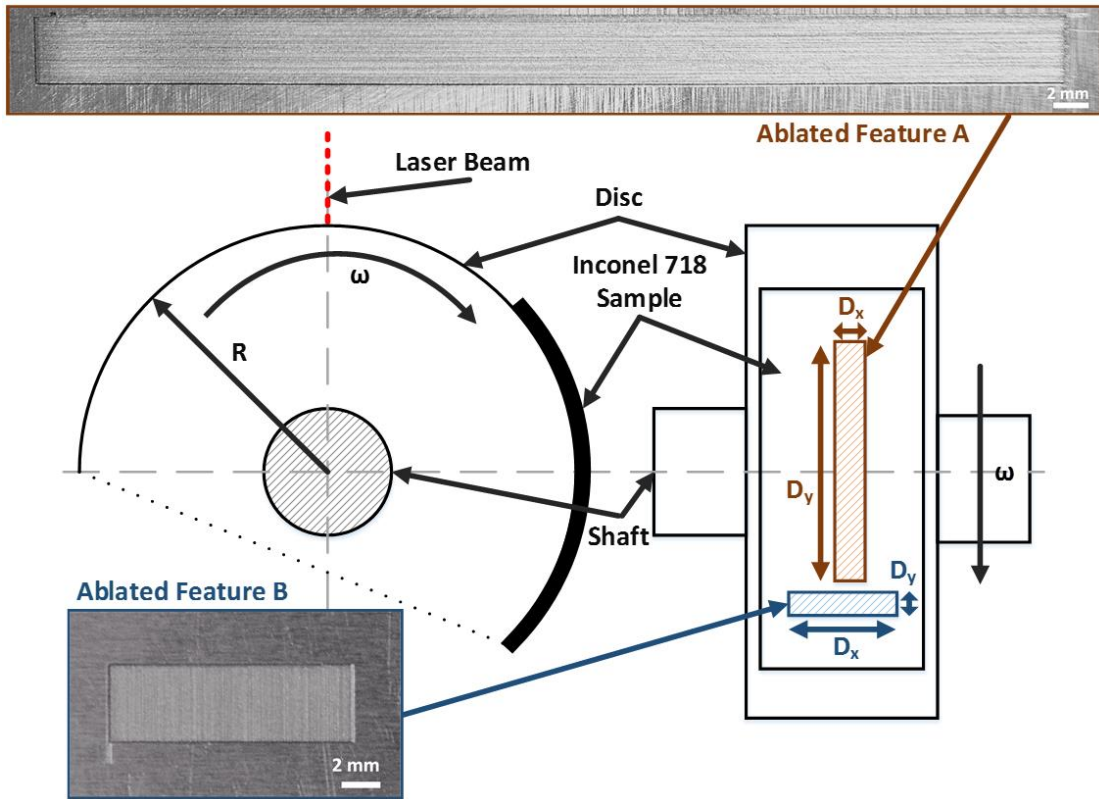


Figure 68 - Ablated geometries used for validation [68]

The dimensions of the two features A and B shown in Figure 68 are given in Table 8.

Table 8 - Long and short feature dimensions for validation experiments		
Ablated features	$D_x$ (mm)	$D_y$ (mm)
A - Long feature	4	60
B - Wide feature	12	4

Given the large number of possible process parameter values, pulse energy was kept constant at 400mJ. As such, laser power output was directly defined by whatever pulse frequency was used for a given trial, given by;

$$P = E \cdot f = 400 [mJ] \cdot f [kHz] \quad (5.2)$$

The ranges for each of the process parameters are given in Table 9

Table 9 - Process parameter values for INCONEL® 718 ablation		
Input Parameter	Minimum	Maximum
Frequency ( $f$ )	28 kHz	50 kHz
Pulse Spacing ( $d_{x,y}$ )	10 $\mu$ m	40 $\mu$ m
No of Layers ( $n_z$ )	1	222
Critical Dimension $D_y$	2 mm	60 mm
Critical Dimension $D_x$	2 mm	60 mm

INCONEL® 718 samples were weighed before and after ablation. The difference in these weights was compared against the target weight inputted into the neural network during its training.

## 6.5 Results and discussion

### 6.5.1 Results from micro-scale picosecond ablation of CVD Diamond targets

Shown in Figure 69 are the results from the first trial, where calibration data was obtained. Ablation constants **a** and **b** are shown (0.0045 and 0.0288 respectively) which are used as inputs to the mathematical model described in Chapter 5. The normalised fluence is calculated from the fluence values used in trial 1, and the maximum fluence identified for the equipment used (58.9 J/cm<sup>2</sup>, operating at 15W @ 50 kHz).

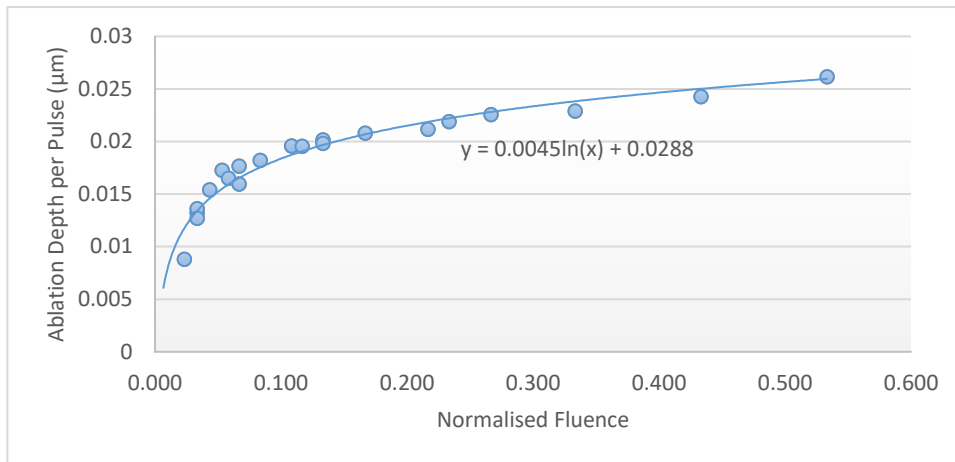


**Figure 69 - Calibration results for validation trial 1**

Using the calibration constants, validation was carried out on the range of parameter sets detailed in trials 2 and 3. A full range of comparisons between predicted and measured parameter sets has also been provided. Errors are measured in terms of percentage differences between predicted and measured ablated depths/volumes. Table 10 and Table 11 shows average depth/volume errors for trials 2 and 3. It should be noted that track overlap validation experiments (Trial 3) where the track stepover was 50% displayed no intra-track peaks, and as such these values are marked as 'N/A' in Table 11.

**Table 10 - Measurement results for crater overlap validation (Trial 2)**

Crater Overlap %	Average Depth Error (%)	Average Volume Error (%)
70	-3.49	-9.77
80	4.40	-0.34
85	4.72	-0.14
90	19.28	10.78
95	12.52	4.47

**Table 11 - Measurement results for track overlap validation (Trial 3)**

Track Stepover %	Repetitions	Avg Trench Depth Error (%)	Avg Peak Depth Error (%)	Absolute Volume Error (%)
10	50	28.56	29.29	21.91
10	100	5.64	-6.21	-6.18
10	150	5.74	-5.52	-6.94
10	250	4.33	-25.33	-8.85
50	50	1.84	N/A	-4.1
50	100	9.91		5.83
50	150	11.08		-2.62

### 6.5.2 Results from macro-scale nanosecond ablation of INCONEL® 718 targets

INCONEL® 718 samples were measured before and after ablation, and mass removal was recorded. The successful iterations of the neural network evaluation of the mathematical modelling were recorded, and the best ones were chosen for validation. Table 12 shows the machining parameters which resulted in the desired mass removal, at the shortest machining time.

**Table 12 - Optimised process parameters from neural network analysis**

Feature	Pulse offset $d_{x,y}$ ( $\mu\text{m}$ )	Pulse frequency $f$ (kHz)	Laser Power $P$ (W)	Width (pulses) $n_x$	Length (pulses) $n_y$	Passes $n_z$	Rotational Speed $\omega$ (rpm)	Total Time $t$ (min)
A	15	48	18	262	3996	56	100	146.72
B	14	45	17	852	281	30	86	297.21

The samples machined with the parameters in Table 12 were weighed, and these results are shown in Table 13.

**Table 13 - Sample mass removal and associated errors**

Feature	Total Time $t$ (min)	Measured mass removal $m_p$ (mg)	Target mass removal $m$ (mg)	Error (%)
A	146.72	83.84	85±2	1.38
B	297.21	16.25	13±2	20.00

### 6.5.3 Observations from results on Picosecond – CVD Diamond target ablation

Accuracy in predicting secondary features of the track such as peak heights (for 10% step over trials), mid-track shoulders (50%-90%) and track width shows modelling capability beyond the initial scope of the algorithm i.e. accurate track depth prediction. In comparing predicted vs. experimental cross sections and seeing good agreements between the two where these features occur, it can be asserted that modelling assumptions are valid in terms of fluence reduction on non-flat surfaces, and depth accumulation for overlapping pulses (across the entire cross section of the beam).

A possible explanation for inaccuracy at high overlap, high repetition e.g. 90%, 250 repetitions, may be due to increased energy absorption in plasma/reflection off steep walls. As the track depth increases, the efficiency of ablation seemingly decreases. Steeper track walls and 'pockets' of plasma may absorb/reflect more and more of the laser pulse energy. This will result in progressively reduced ablation

efficiency on a pulse by pulse basis, eventually having insufficient pulse energy absorption into the material for ablation.

It should be noted that all of the depth predictions for high overlap and high repetition tracks are overestimates, suggesting that <100% of energy is used for ablation in reality, whereas simulation assumes 100% of the laser energy is used for ablation.

A 90% overlap will result in any given location on a track receiving 10 pulses of laser radiation, with 6-8 of these being at high intensity areas of the beam (the first and last pulses will only overlap this location with the edge of the beam, which is at low intensity). If this highly overlapped track is then succeeded by another track with 90% step over (i.e. 90% of the width of the track is coincident with a second track), this figure is doubled. Lastly, when repeated 250 times, there will be approximately 4000 (8 pulses, 2 tracks, 250 repetitions) pulses on one location, which is many more than the single pass from the SPI G3.0 system. As such, the diminishing returns achieved by successive pulses will be more noticeable due to steeper track walls, energy absorption in ablated plasma, and reflection. Figure 70 shows this cumulative error in track depth and volume prediction.

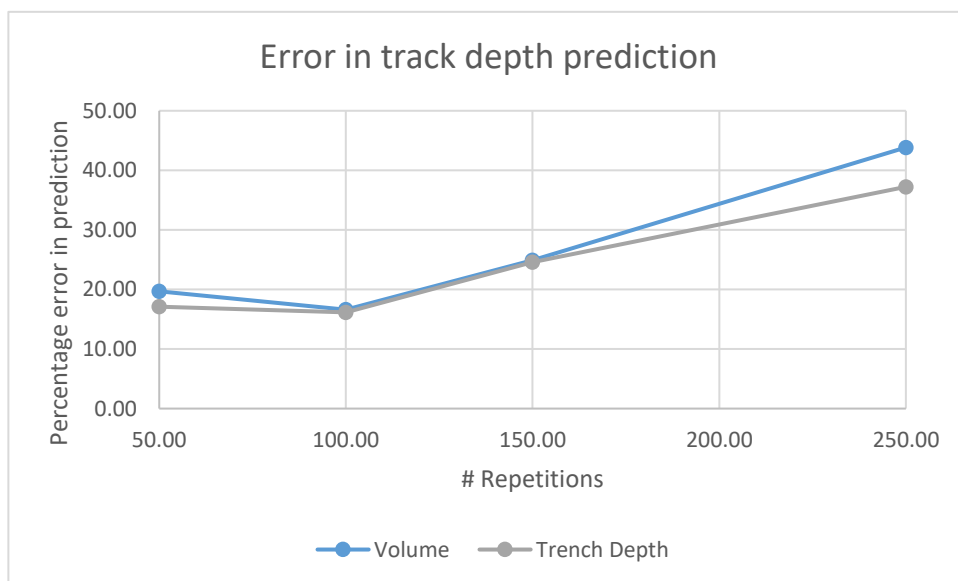


**Figure 70 - Error in track depth prediction for 90% overlapped pulses on EWAG Laserline**

Given the accuracy of prediction for 10/50/90% step over, one can assume modelling accuracy of a similar degree for larger volumetric ablation trials, e.g. 100 tracks at 10/50/90% step over. Two tracks with a defined step-over can be seen as a 'building block' for larger volume ablations with similar step-over for multiple

tracks, and as such the cross section of these predictions will just repeat as more tracks are added.

#### 6.5.4 Observations from results on Nanosecond – INCONEL<sup>®</sup> 718 target ablation

The model shows predictive capability when being used to remove a large mass of material from a target, where a large number of laser pulses are simulated, e.g 58.6 million pulses in feature A as described in Figure 68 and Table 8. Mass removal was found to be accurate to within 1.38% when using long and narrow features, which are those most likely to be used in practice when balancing rotating components, the scenario used in this validation exercise. This error increased to 20% when machining short and wide features, the reason for which lies within positioning errors induced from computer latency and target cooling when such low proportions of each rotation are used for ablation.

## 6.6 Summary

The mathematical model presented in Chapter 5 was validated using comparisons of predicted micro-scale ablated surfaces and measurements of topographies generated experimentally. Simulated surfaces were generated for laser crater overlaps ranging from 70 to 95%, and track overlaps at 10, 50, and 90% with a 90% crater overlap. A high degree of accuracy (approximately 10% or lower error in crater depth) was seen between predicted and measured topographies for tracks of varied crater overlap. Good agreement was also seen for predictions of tracks overlapped at 10 and 50%. Errors rose in predictions for 90% overlapped tracks at high numbers of passes, and this was likely due to nonlinearities between numbers of passes and laser radiation absorption within ablated material plasma trapped in the steep trenches.

Macro-scale validation was also carried out on predicting volumes of ablation of a large number (millions) of pulses, to generate representative repair geometries for a component balancing scenario. With the integration of the validated model into a trained artificial neural network, laser processing parameters were calculated which would prove to generate repairs with measured mass removals as low as 1.38% under predicted mass removal.

# Chapter 7. Blend Generation and High Cycle Fatigue Testing

## 7.1 Introduction

After laser machining parameters have been optimised as described in Chapter 4, repair blends can be generated and tested for fatigue performance changes induced by the processing method employed. For means of validation of the process, it can also be compared against an alternative to laser machining, being mechanical boreblending. For this comparison, blends of a set geometry and location were machined into blades by laser and mechanical processing. The fatigue life of blades treated with these methods were compared against each other. Acceptance of the laser based repair method was dependent on the repairs generated to perform as well as, or better than, mechanically repaired samples. In addition to this, the time to create laser-processed repairs must not exceed the time taken for mechanical ones.

All results and analysis of high cycle fatigue testing presented in this chapter, as well as the management and performance of the tests themselves, are courtesy of Rolls-Royce and Element Materials Technology.

## 7.2 Blending Processes and their implications

This chapter highlights some of the major differences between the effects of both mechanical and laser machining methods used for repairing the components considered in this project, and therefore which method may be more appropriate for the proposed application. Whilst one repair method may be more appropriate than the other, it is worth noting that using either repair method will result in a component with higher fatigue strength than those left with un-treated foreign object damage. In addition it will aim to provide some guidance as to an approach to achieve optimal results with the 'best' machining method. Both machining methods will have their ability to produce pre-defined stress relieving features assessed and compared. Repair geometries are described in the methodology in detail. Surface quality and geometric characteristics of the repairs generated by each method will be analysed, both of which have implications for the stress relieving capabilities of the repair. To achieve a quantitative analysis fatigue life of repaired components will be measured and compared to each other, giving an indication of fatigue life change induced by the repairs.

### 7.2.1 Mechanical Boreblending

This method uses an abrasive tool such as a ceramic or diamond coated form (sometimes assisted with a diamond abrasive paste), which is rotated at high speed (up to 5000RPM) and applied tangentially to the part. This tool can be brought to the component work surface via borescope access ports, and hence is referred to as boreblending. The abrasive surface will remove material mechanically, and in so doing a geometric feature can be created within the component material.

### 7.2.2 Laser Boreblending

A secondary set of advantages when using PLA over mechanical blending are those not directly concerned with the metallurgical implications of machining, as mentioned within the literature review section of this thesis. These include the absence of mechanical loading on the component/tool during processing and the possibility for partial/full automation of the process. Automation offers a potentially faster process time, and much lower technical skill requirements from the operator when compared to mechanical blending.

## 7.3 Repair location and geometry

Finite element analysis was performed by a Rolls-Royce Compressor Stress analysis team to identify the lowest vibration mode where the peak stress in the representative component is located on the leading edge of the blade [71]. The first 7 vibration modes were analysed, and a suitable leading edge mode was selected for testing. This location was used for comparison of the repair methods, as it presented a "worst case" scenario for post-repair stresses experienced by the component. Repairs of the same type in other locations on the blade would therefore result in lower component stresses, and present better fatigue performances. The size and location of the proposed repair was held constant across both repair methods. The relative dimensions of the repair were then prescribed by the Rolls-Royce compressor stress analysis team, shown in Figure 71, where the width of the repair sufficiently long as to not exacerbate existing, or create new, stress raising features. In both repair cases, this geometry is a 2.5D feature where the repair profile is constant throughout the depth of the component.

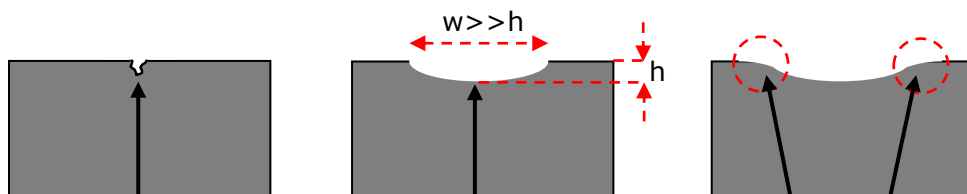


**Figure 71 – Example of Component damage and the relative dimensions of repair geometries**

To validate the performance of the laser ablated blends, trials were undertaken to investigate the fatigue life loss from the repair process. To find the full extent of this, a mode shape resulting in 'worst' principal stresses was identified, and the location of the peak stress was to be the location for the centre of the blend. As such, this worst-case scenario would identify the shortest possible failure life, and failure mode, for a nominal width to depth repair as described earlier. 10 of these blends were performed on engine-run, Trent XWB HPC blade leading edges. As a comparison, 10 mechanically boreblended blades were prepared, with the blend in the same location.

## 7.4 Optical Head Considerations

To extend this study to real-world equipment that would be used to perform these types of repairs in-situ, an additional set of repairs for various blend types was necessary. There were two major considerations when extending these repairs to the optical head proposed for in-situ repairs.

Figure 72 demonstrates the first of these considerations, being that of a difference in optical depth of field between the laboratory and in-situ repair equipment to be used for generating repairs. The figure shows a laboratory beam (blue) and an optical head laser beam (red) drawn to scale. The optical head equipment necessitates having as wide a beam as possible on the mirror such that thermal loading on the mirror and its supporting mechanisms is minimised. Development of the laser system showed that thermal loading to these parts was a major failure mechanism of early design iterations. As noted in the figure, both beams have a similar diameter at focus, however largely disparate focal lengths. This results in a linear relationship between both spot sizes as they vary with distance away from the focal plane of the respective beams. As shown in Figure 72, at focus both beams have the same diameter.

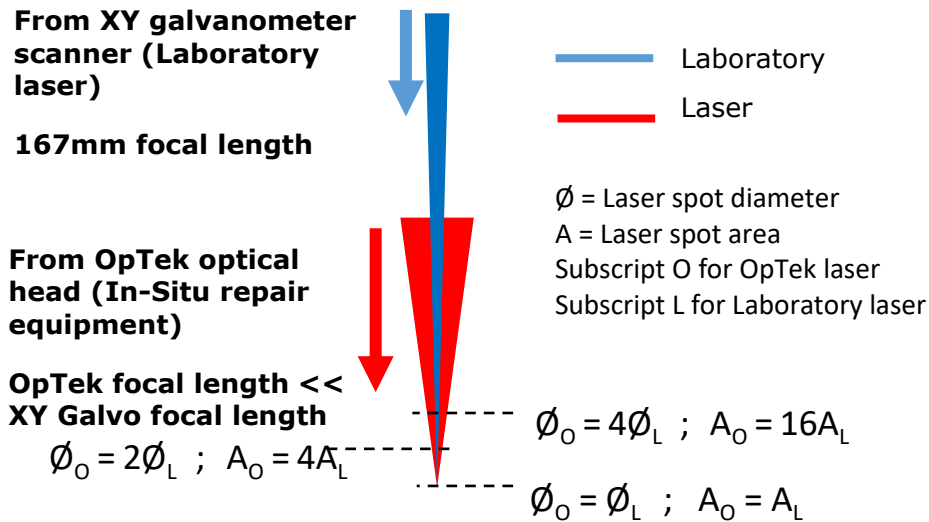


**Figure 72 - Depth of field comparison of both laboratory and In-Situ repair laser systems**

As beam area is a quadratic function of beam diameter, laser beam area (and hence laser fluence) will be reduced by a factor of 4 on the optical head laser compared to the laboratory laser, when moving to a working surface twice as far away from focus as any other given work surface. As such, any stray from the focal plane will have a much more severe effect on machining efficiency when using the optical head over a laboratory set up. The useable depth-of-field of the laboratory laser was approximately 5 times deeper than the OpTek optical head's.

A secondary consideration was the structural tolerance of the smaller, OpTek produced optical head to be used for performing the in-situ repairs. Given strict spatial restrictions on the equipment that can enter the engine through inspection

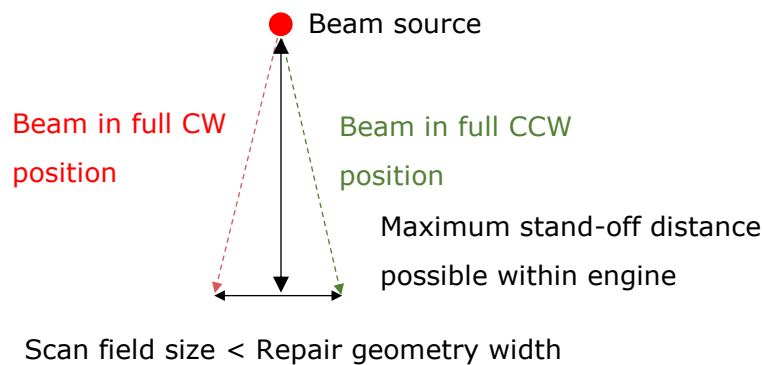


**Figure 73 - Scan field size limitations due to mirror movement limits**

ports, and the components it must navigate past to reach the target components, the system as a whole is very small relative to those commonly used for component machining. The space within which the optics guiding the laser can move dictates the size of the scan field, as shown in Figure 73.

The total angular range of the beam source and the focal length of the laser can be used to calculate the scan field size. Therefore, if the maximum scan field size achievable by the optics being used is smaller than the required repair geometry, then multiple scan paths must be used to complete the repair as shown in Figure 74.

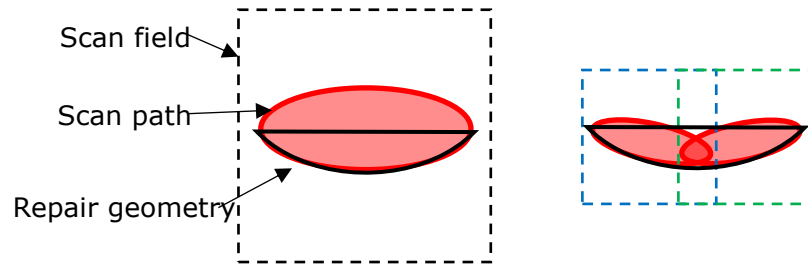


**Figure 74 – Example of scan path fitting to repair geometry for a) single scan path and b) multiple scan paths**

It is worth noting that using multiple scan paths will result in a minor (yet potentially important) feature being present in the repair geometry - localised peaks on the blend surface.

Figure 75 below shows scan paths and resultant geometries for using one, two and three ellipses to generate the repair. The dotted black line shows a 'guide' line for the geometry, with rounded shoulders included for comparison to raster scan created repairs. Circled in red dotted lines are the localised peaks along the blend surface, where material is not removed as the two or three smaller scan paths cannot cover the entirety of the profile drawn by the black dotted line. It should be noted that in Figure 75d, the location of this peak is very close to the area of highest stress in the component.

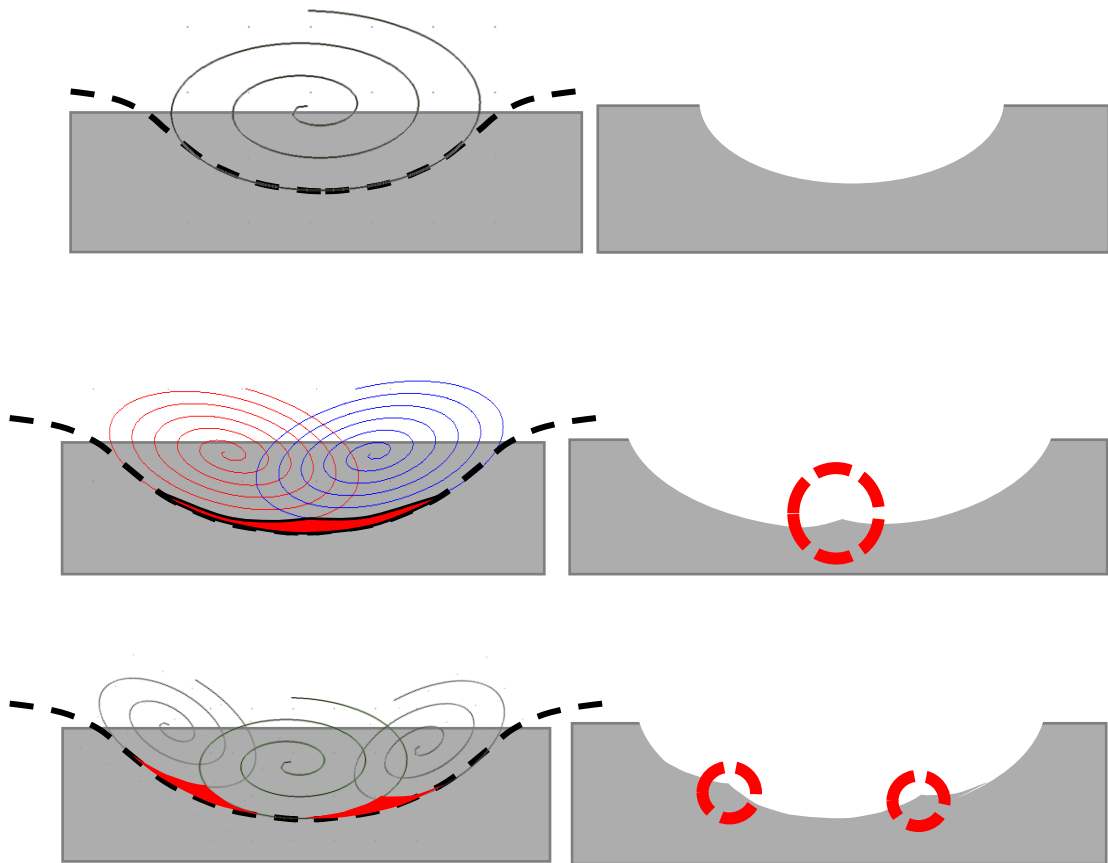


**Figure 75 - a) Single ellipse scan path, b) Single ellipse repair geometry, c) Double ellipse scan path, d) Double ellipse repair geometry, e) Triple ellipse scan path, f) Triple ellipse repair geometry**

## 7.5 Scan path adaptation from laboratory to optical miniature head laser.

For this study, two different scan path methods have been employed; elliptical spiral scans and raster scans. Figure 76 shows a basic diagram of each of these scans, with an a) elliptical scan path and b) raster scan.

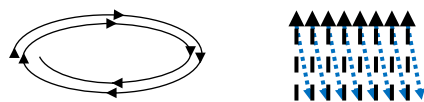


**Figure 76 – a) Elliptical spiral scan path, b) Raster scan path**

Within the raster scan diagram, black dashed lines are parts of the scan path where the laser is firing, and blue dotted lines are parts where the laser is not firing but simply traversing to the next fire location. In reality, the lines where the laser is firing would be much more closely packed to achieve a good coverage of material removal on the workpiece surface. This results in sharp angular changes in direction ( $\sim 180^\circ$ ). Assuming constant velocity along steady state proportions of the straight

lines within the raster scan, acceleration is only present at the very ends of the scan lines. This is where the guiding optics have to slow down to zero velocity, and then traverse back at  $\sim 180^\circ$  to the previous line. It is in this scan regime that the guiding optics are effectively mechanically oscillating around one axis.

In a galvanometer mirror set up, only one mirror (e.g. Y direction mirror) will be oscillating, as the vast majority of beam displacement is in only one direction. The second mirror, which simply 'steps' the scan path over onto the next line, will be under much lower stress due to only having to move comparatively negligible distances (e.g.  $10\mu\text{m}$  vs  $1000\mu\text{m}$ ), and having to do so intermittently (only on return path to next laser firing line) for approximately 50% of the total scan time, resulting in fewer stress inducing cycles that the primary mirror is subjected to. If a single guiding optic is being used for both X and Y scanning directions, stress is increased over that of a galvanometer mirror arrangement, however the secondary mirror's stresses are negligible compared to those of the primary mirror.

In a raster scan therefore, the heavy components within the guiding optics system will endure the highest stress inducing forces, as high accelerations are present. To reduce stresses incurred, lower mass, and fewer/smaller moving parts are ideal for the system, in addition to the stress reduction of using a continuous spiral scan path.

The elliptical scan paths have their maximum acceleration at the tightest radii on the ellipse (left and right side of the elliptical scan path). This is shown below in Figure 77 with magnitudes of acceleration which the guiding optics system is subjected to. The orange line shows the acceleration of a raster scan, with intermittent, sharp changes ( $\sim 180^\circ$ ) in direction resulting in high spikes of acceleration between adjacent raster scan tracks. The blue line shows a much lower peak acceleration magnitude, representing the forces subjected to a guiding optic in an elliptical scan path. Peak accelerations are seen at the smallest radii of the ellipse (left and right edges as shown in the figure), but as these are not such sharp changes in direction as those in a raster scan, acceleration is lower.

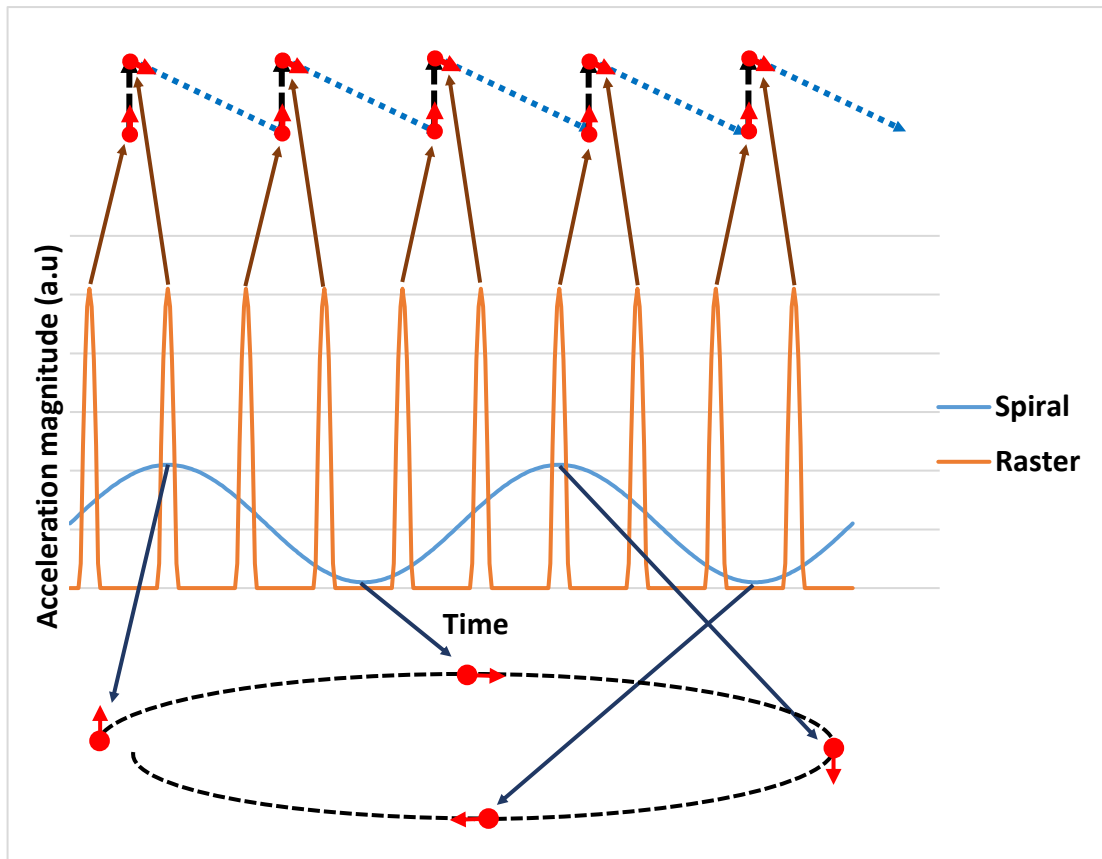


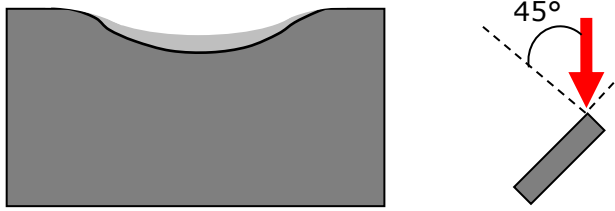
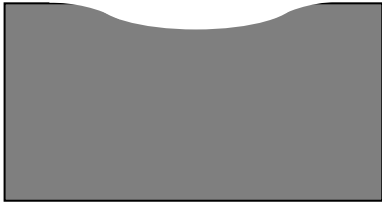
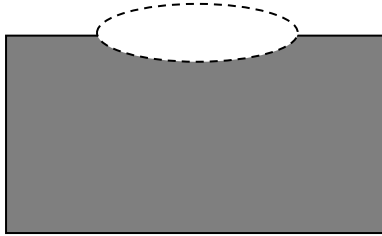
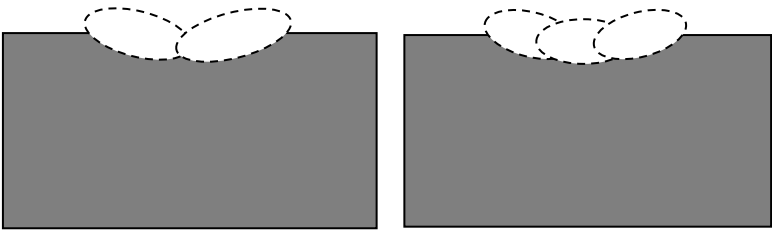
Figure 77 - Relative magnitudes of acceleration in raster vs. elliptical scan paths

## 7.6 Methodology

### 7.6.1 Blend Generation

Blends were generated with a range of scan paths and techniques, to characterise how the end-user blending equipment will perform compared to mechanically blended components. Table 14 below shows the geometries and description for all of the blended samples included in the high cycle fatigue testing carried out in this project. Included are samples emulating repairs with the proposed blending equipment during an early design iteration, with the angle of attack being  $45^\circ$  to the blade edge (Trial number 2 in Table 14). The rest of the blends are representative of the latest design iteration, with a  $90^\circ$  angle of attack. For each blend geometry, 10 samples were created in as much of a repeatable and controllable manner as possible. Mechanically blended samples were performed by specialists at Rolls-Royce.

**Table 14 - Blend geometries for high cycle fatigue testing**

Trial Number	Diagram
1) Sharp 'Knife Edge' angle following geometries used in HCF Tests #1	
2) Mechanical blending to existing RR standards and practices	
3) 90° Blend without rounded shoulders (laser only)	
4) Blend generated from multiple scan paths (no shoulders, laser only)	

### 7.6.2 Mechanical Boreblending

Boreblending was performed using off-the-shelf blending probes and grinding tips, which are used for repairs on components as per FRSB551. The axis of rotation of the grinding tip was perpendicular to the component, as shown in Figure 78.

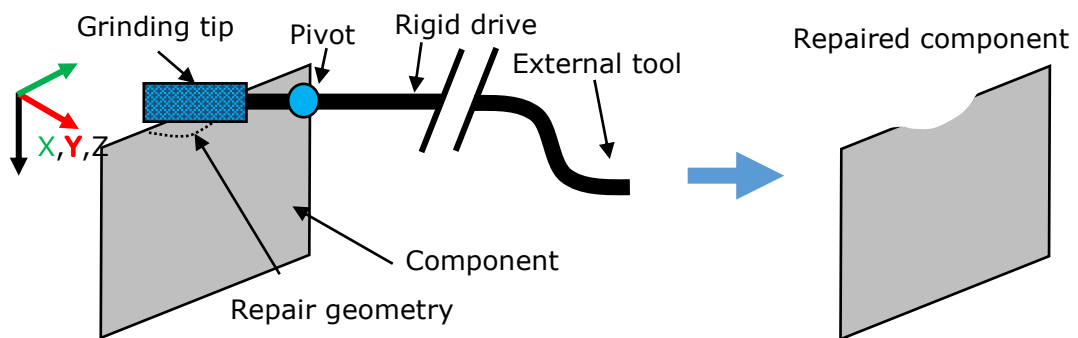


**Figure 78 - Boreblending equipment and tool alignment**

The mechanical boreblending tool was also used to polish the surface of the repair, using a finer grit head, after the main repair geometry had been created. Machining parameters for both of these processes (bulk cut and polishing) were taken from best practice for the component in question and the tool being used.

### 7.6.3 Laser Boreblending

Using the same repair geometry as the mechanical boreblend, a selection of laser blends was generated. Optimal laser processing parameters were defined from a full factorial metallurgical study covering 3 key laser processing variables; average power output (W), pulse repetition frequency (kHz), and laser scan speed (mm/s). Each factor was evaluated at three different levels; those which would be considered low, medium, and high for this application. The optimal values chosen were those that produced the least surface damage and microstructural change within the material after processing.

Laser repaired components were aligned at 45° to the laser beam, as shown in Figure 79. This angle of attack of the laser beam created a sharp knife edge feature, as can be seen above. The reason for creating knife edge features in the components was to present a 'worst case' for the laser repair method. Compared to repairs generated mechanically these knife edges were non-ideal in terms of stress relief, as sharp features are generally stress concentrating geometries. In practice, should angles of attack closer to 90° be employed, it is likely that component fatigue strength will be at least as good as, if not better than, those seen in this study from laser repairs.

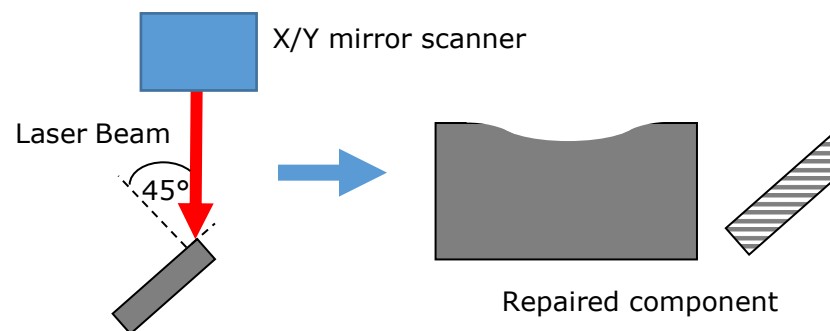


**Figure 79 – Laser/component alignment and repair geometry**

In determining laser machining parameters which should be used for the repair process, the full factorial experiment determined which processing parameters gave a good compromise between preserving the microstructural integrity of the component, and the total time taken for the process.

The repair was generated by a raster scan within successive layers to fully remove any material within the repair geometry. This is a requirement of these repairs, due to the need to avoid any large chunks of component material falling into the engine. As such, the entirety of the volume of material to be removed must be done so whilst generating little/no debris.

Once a set of optimised parameters had been identified (results and discussion in Chapter 3), these were used to ablate a representative repair in a set of components.

To generate representative repairs, an ellipsoidal section with rounded corners shown below in Figure 80a) was used. On the figure is shown the direction of laser pulse tracks scanned from one side of the geometry to the other. This shape was projected top-down onto a blade (shown Figure 80b). A brief investigation into optimal track step-over distance (the horizontal distance between vertical tracks in Figure 80a) was carried out using the optimal parameters identified in Chapter 4.

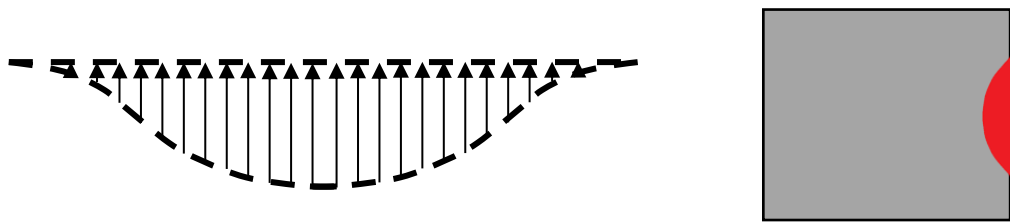


**Figure 80 - a) Blend geometry scan path and b) Top-down scan path projection onto sample**

The first generation of the equipment proposed to perform this repair offered a  $45^\circ$  angle of incidence between the laser and the blade edge tangential plane. As such, blends were generated also at  $45^\circ$  for validation of the laser repair process as it was defined at the time of this first experiment. Figure 81 shows how a sharp 'knife-edge' feature will be generated.

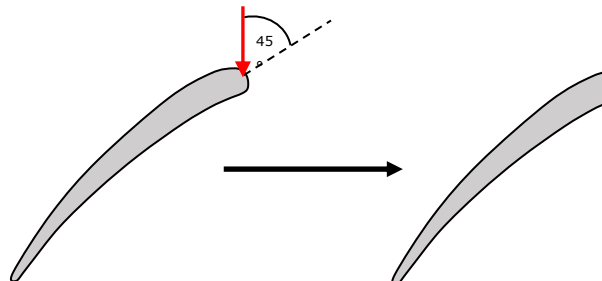


**Figure 81 - Resultant blend geometry including sharp edge from angled blending (Trial 1)**

It should be noted that blends exhibiting features such as the knife edge described above are undesirable in practice, as any sharp features act as stress concentrators

and potential crack initiation sites. However these repairs were used as a benchmark for HCF testing as, at this point in the project progression, 45° angle of incidence was the planned approach. In addition, work on rounding off the laser side edge, being the sharp knife edge, had not been carried out.

To produce repeatable laser ablated blends at the prescribed location, a jig was used to hold the blade in a known orientation with respect to the laser optics. A high temperature resistant epoxy putty was used, such that minimal distortion was seen as the component heated up, and hence heated the jig, during machining.

Using multiple passes of the geometry described in this chapter, with each pass taking approximately 1 to 1.5 seconds dependant on blend geometry. It is worth noting that during machining the blade did get very hot to the touch, however this was not quantified. Thermal expansion may be a consideration when designing scan paths such that a more even distribution of expansion-induced stresses is achieved.

During processing, the resin mount used to hold the component was damaged and had a small area of degradation where the laser beam fell after ablating through the blade material. This should not be cause for concern with regards to the laser damaging components behind the blade to be repaired. This is because the depth of field (and hence effective machining field) used in the experimental set up is far greater than that which would be deployed to repairs in service. As such, any components even a few millimetres behind the blade will be unaffected by the in-service system. It should also be noted that the putty is likely to have a much lower ablation threshold energy. As such even a small amount of laser radiation (which would have little to no effect on aerospace alloys) is still able to burn the epoxy putty as seen.

#### 7.6.4 High Cycle Fatigue testing

High Cycle Fatigue (HCF) testing was used to evaluate the effects of the different repair methods on the service life of the components. Finite Element Analysis (FEA) methods were used to calculate a vibration mode at which a large alternating stress would occur in an area of the component in which failures could more likely occur in service. Each component was then placed in a piezo-electric shaker, and vibrated at a fixed frequency, with increasing alternating stress. Stress was increased at a fixed time interval, until a change component vibration frequency was detected, indicating component failure.

Figure 82 shows a diagram representing the loading and measurement set-up used in the HCF testing part of this study. Components were loaded in a fixed-free arrangement, with a 30Nm clamping load at the fixed end.

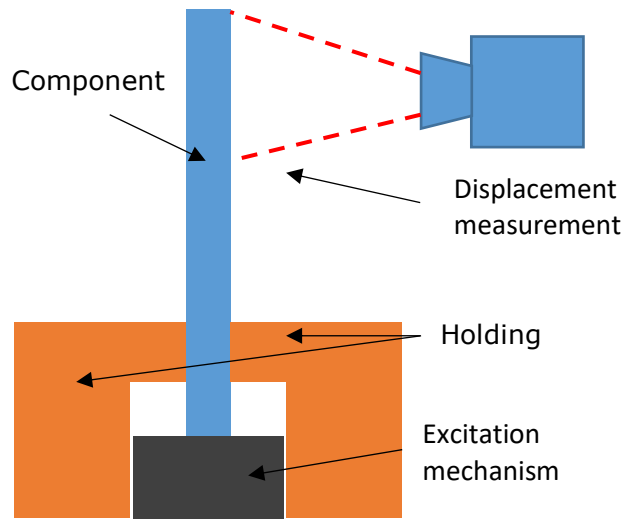


**Figure 82 - High cycle fatigue test set-up**

The loadings scheme for the two component repair types (laser boreblended, mechanical boreblend) are given in Table 15. All of the vibration frequencies shown in Table 15 are normalised to the theoretical vibration frequency for a mechanically boreblended component.

**Table 15 – High Cycle Fatigue testing parameters**

Repair Method	Initial Load (MPa)	Incremental Load (MPa)	Increment period (minutes)	Normalised Vibration Frequencies (Hz)			
				Theoretical	Experimental determined from HCF testing		
					Min	Mean	Max
<b>Laser boreblended</b>	$\sigma_i$	$\frac{\sigma_i}{4}$	12	1.009	0.911	0.926	0.940
<b>Mechanically boreblended</b>	$\sigma_i$	$\frac{\sigma_i}{4}$	12	1.000	0.900	0.911	0.926

Each individual component had a separate vibration frequency calculated such that it would vibrate at the pre-selected mode. The experimentally determined HCF frequencies were within 10% of the theoretical frequencies for each of three blade sets for the chosen vibration mode.

The fatigue strength for a component at a high number of stress cycles, typically  $10^7$ , can be estimated from measurement of component surface displacement and alternating stresses during high-cycle fatigue testing [72],[73].

AF failure strength at  $10^7$  cycles, and material confidence factor (MCF) at failure for each component were recorded and used to compare repair types. These are two metrics used within Rolls-Royce internal reports for comparing different component/manufacturing method fatigue strengths, and for quantifying the performance of a component or manufacturing method against expected values [71]. These values are shown in the results section. MCF is defined as the ratio between observed and expected failure strengths. AF calculations are taken from Rolls-Royce documentation [71], and they are given by;

$$AF [mHz] = \frac{a}{1000} \times \left( \frac{S_{c20^0C}}{\sigma_{ac}} \right) \times f \quad (6.1)$$

Where a = peak modal displacement (mm/mHz)

$S_c$  = Typical  $10^7$  cycle fatigue strength for sample material at 20°C (MPa)

$\sigma_{ac}$  = Peak modal alternating stress (MPa/mHz)

f = Modal frequency (Hz)

Peak modal displacement (a) is obtained through optical measurements during testing, shown in Figure 82.

MCF is calculated as;

$$MCF = \frac{AF_{Experimental}}{AF_{Theoretical}} \quad (6.2)$$

These analysis techniques and values can be related to the Goodman analysis method, where fatigue limits are related to alternating stresses.

#### 7.6.5 Fracture surface inspection

Surfaces of the fractures in the tested components were examined to learn more about the failure mechanisms involved. To determine the location and size of cracks, UV-responsive penetrative dye was used, as well as visual inspection of the component surfaces with optical microscopes in and around the repair site. Once located, crack tips were marked with pen to ensure crack surfaces were not damaged when components were split to reveal the cracks.

Components were split such that both sides of the fracture could be preserved and studied. This was done by removing a section of un-affected component material using an ATM Brilliant-250 cutting disc machine. After a wedge of material had been removed from the component, it was held securely in a vice and a corner of the material was tapped with a hammer to open up the crack, in such a way that the

fracture surfaces moved directly away from each other and no excess rubbing occurred.

Separated component halves were then cleaned to remove any machining fluid residue or dust from the fracture surfaces. This was done by immersing component halves in propanol and placing them in an ultrasonic bath at room temperature for 10 minutes.

Sample fracture surfaces were then examined using optical microscopy, a Bruker Contour GT white light interferometer, and a Philips XL30 SEM. Three analytical methods were chosen to give a range of data on the fracture surfaces, from low-magnification qualitative characterisation of the surfaces using optical microscopy, to quantitative 2D (fracture plane) and 3D (fracture topography) characterisation using SEM and interferometric analysis respectively.

Figure 83 shows the process of fracture surface opening, with a fully closed component opened up by successive hammer taps to separate both halves of the component.

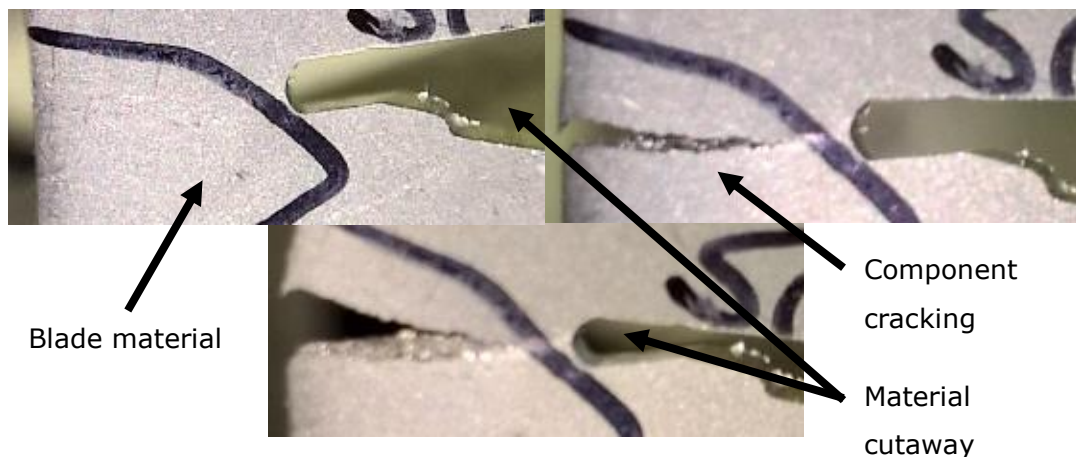


**Figure 83 - a) Closed, b) Opened, c) Separated crack surfaces in components**

## 7.7 Results

### 7.7.1 High Cycle Fatigue Results

High cycle fatigue testing was carried out in two stages, with initial tests being performed on samples shown in Table 14 under trials 1 and 2 - 45° knife edge laser blends, and 90° best practice boreblends. Further testing was performed on the remaining trials 4 and 5 - Single and multiple ellipses, generated both on laboratory and OpTek laser equipment. Throughout this testing, frequency and mode shape analysis checks were performed. This was done to ensure that blades were vibrating in the desired mode to create the peak stress at the location intended for testing.

Each of the laser boreblended and mechanically blended samples were put through a high-cycle fatigue testing regime as described in section 7.6.4. Table 15 shows the incremental stress levels generated in the component through piezo-electric excitation. All of the vibration frequencies shown in Table 15 are normalised to the theoretical vibration frequency for a mechanically boreblended component. Component failure was defined as the moment when a 1% shift in component vibration frequency was detected. The majority of the samples failed in the expected location: at the highest stress region for the blades, and within the repaired region of the component for the laser and mechanical boreblended blades. Those that didn't, were removed from results and analysis, as the reason for failure in other locations was the unintentional excitation of a neighbouring excitation mode due to the narrow gap in frequency between these modes. Failure criteria are quantified with two metrics AF and MCF as previously described. Ten HCF specimens were tested (to provide statistically meaningful results), and an S/N curve with a slope that is commonly used in aerospace for these components was applied to the raw AF values. Using this S/N curve, the AF values at  $10^7$  cycles were determined.

MCF is a confidence factor for each repair method, expressed as a ratio between predicted and observed AF strength at  $10^7$  cycles. Predicted AF at  $10^7$  cycle values were calculated from Finite Element Analysis used 3D scans (GOM) of the components. These scans are performed optically using a single light source and two light sensors, and triangulating the measured data to generate an XYZ data point cloud describing the component surface being analysed. It should be noted that when calculating MCF values for the repaired components, AF values calculated from GOM data of the blades was used. This was because the geometries of the laser and mechanically repaired components were not equivalent due to the knife edge present in laser repairs. As such, a higher confidence in MCF values can be gained by comparing experimental and theoretical (GOM) failure AF loads through knowing the exact geometry of each repaired component.

**Table 16 –AF failure levels and material confidence factors (MCF) for three sample sets (Trials 1, 2)**

Trial	Normalised AF $10^7$ cycle fatigue strength (mHz)		MCF
	Theoretical	Experimental	
Laser boreblended (Trial 2)	0.83	1.31	1.59
Mechanically boreblended (Trial 3)	1.00	1.45	1.45

Table 16 shows the failure load criteria (AF) of the components used in the first round of testing described (Trials 1 and 2). Mechanically repaired components had a mean normalised  $10^7$  cycle fatigue strength of 1.45 mHz. Laser repaired components had a slightly lower mean  $10^7$  cycle fatigue strength of 1.31 mHz, 9.7% less than the mean failure strength after  $10^7$  cycles for mechanically repaired components. The spread of fatigue strength for laser repaired components was higher than that of mechanically repaired components. This is possibly due to the variation in blend placement upon the leading edge of the blade. As all blades in this experiment had been engine run, any variation in blade geometry resulting from historical loading cycles will cause blend placement to be inconsistent, as blades are placed in a jig with a fixed location with respect to the laser optics. Boreblended components however were all done manually and repaired were aligned by eye.

The normalised failure strengths at  $10^7$  cycles are also given in Figure 84. High-cycle fatigue performance is accepted when the MCF is greater than or equal a pre-defined Rolls-Royce acceptance value, ' $n$ ', for components undergoing high-cycle stresses after repair. As a minimum AF  $10^7$  strength, this is equivalent to  $n \times 1.00$  mHz (the normalised theoretical  $10^7$  failure strength of mechanically repaired blades). Therefore, as long as the mean failure strength of the various repair methods is above  $n \times 1.00$  mHz, it can be stated that the MCF for each method is greater than the minimum acceptable value. The laser and mechanical boreblend repair methods have MCF values of 1.59 and 1.45 respectively, which implies that the component and the repair method used has performed at least as well as, if not better than, theoretically predicted. Given the worst-case nature of the laser repairs arising from the knife edge in the repair geometry, the fatigue performance of these repairs is the minimum that can be expected, and as such the confidence (MCF) is the most conservative value. The normalised mean failure strengths at  $10^7$  cycles calculated from experimental data are shown in the graph below in Figure 84.

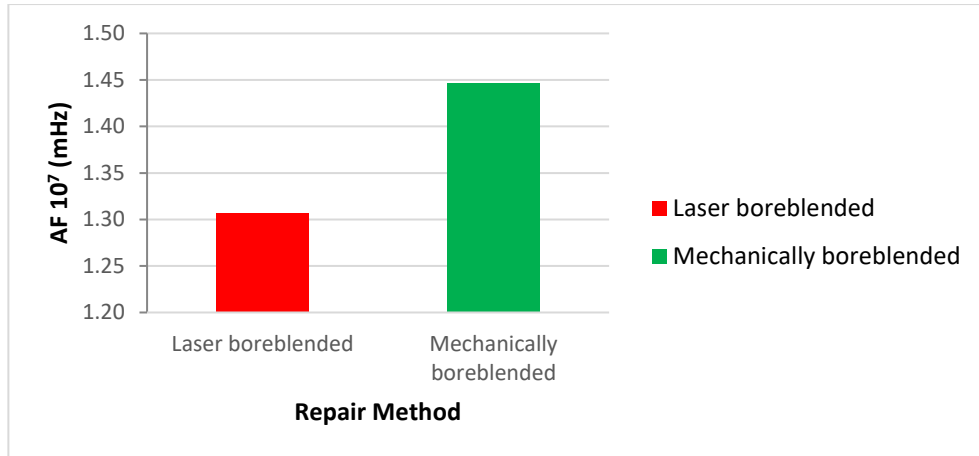


**Figure 84 – Mean normalised AF 10<sup>7</sup> cycle failure strengths for each sample type in Trials 1 (Laser bore) and 2 (Boreblend)**

**Table 17 –AF failure levels and material confidence factors (MCF) for two sample sets (Trials 4,5)**

Trial	Normalised AF 10 <sup>7</sup> cycle fatigue strength (mHz)		MCF
	Theoretical	Experimental	
<b>Boreblended (Trial 2)</b>	1.00	1.78	1.78
<b>1x Laser blended ellipse (Trial 3)</b>	1.00	1.71	1.71
<b>2x Laser blended ellipse (Trial 4)</b>	1.00	1.90	1.90
<b>3x Laser blended ellipse (Trial 4)</b>	1.00	1.84	1.84
<b>3x Laser blended ellipse with OpTek head (Trial 4)</b>	1.00	1.51	1.51

Further testing was then conducted on a second round of samples and blend types, detailed in Table 14 as trials 3 and 4. As with the previous set of tests, boreblended samples (Trial 2) and un-repaired samples were also included. This was done as the blades were from a different engine run batch, so benchmark testing was required to compare results against the two separate HCF testing regimes. Fatigue performance against boreblended samples was used to assess laser repair quality and performance.

Figure 85 shows results for the second round of HCF tests. Fatigue life deficits in components with foreign object damage (FOD) undergoing cyclic stress is well understood [74]–[76]. As such it can be stated with confidence that the introduction

of a repair geometry will improve the fatigue life of a component with FOD beyond the fatigue life of an unrepaired component with FOD.

As seen in Figure 85, the laser repaired components performed similarly to those repaired mechanically, as expected and confirming results shown in Figure 84 for the initial HCF trials. Further agreement is found with the initial HCF trials in that a single laser blended ellipse performs slightly worse than a boreblended repair, however improvements over boreblended repairs are seen when multiple ellipses are used. This is likely due to the lower amount of mass being removed, where the 'pips' between blends described in Figure 75 are left and may act as stress relieving features. There is a difference in fatigue strength for laser blends generated with 3 ellipses on the laboratory laser system and on the OpTek system, likely attributable to the difference in surface quality of the blends.

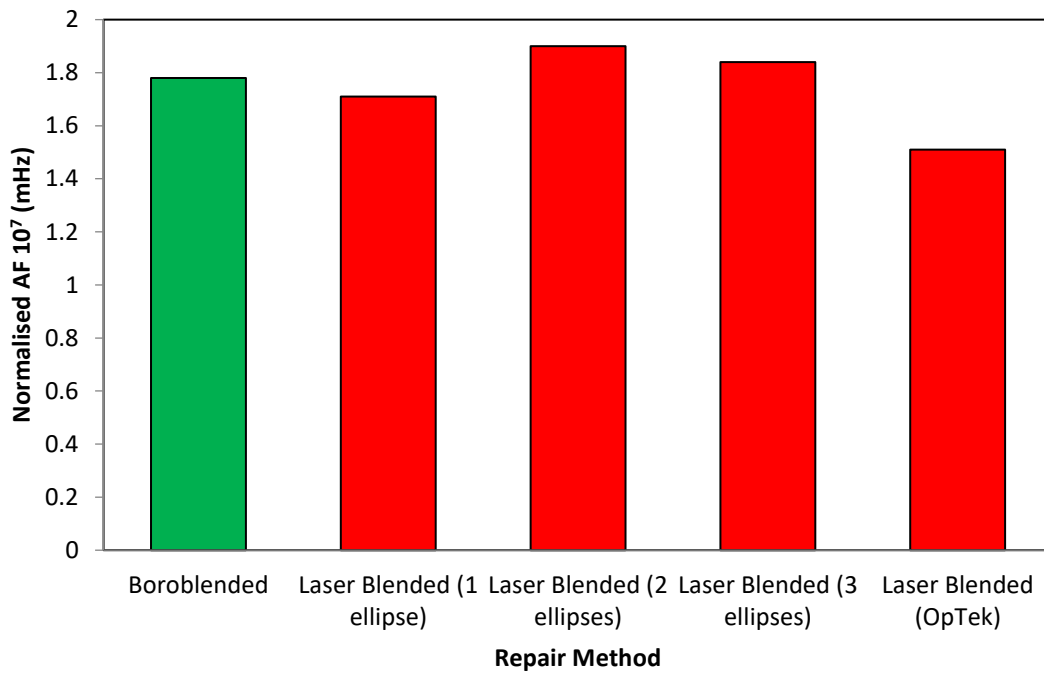
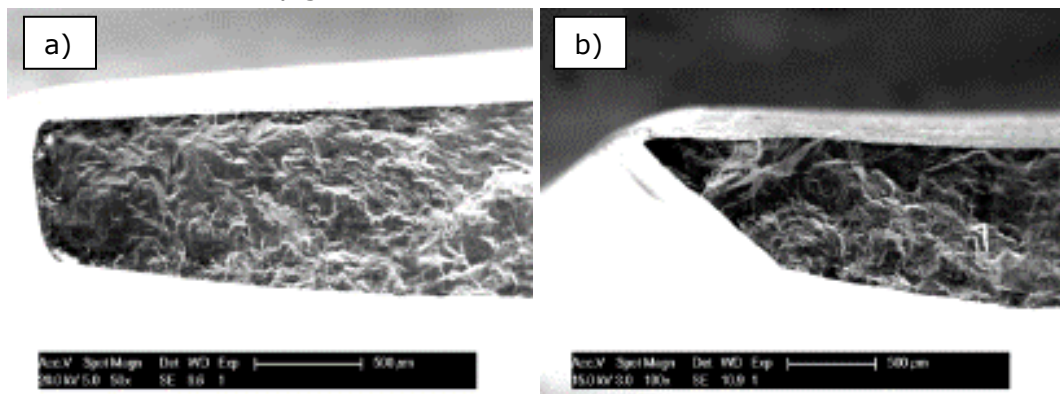


Figure 85 - Mean AF failure strengths at  $10^7$  cycles for each sample type in Trials 3 and 4

### 7.7.2 Fracture surface inspection

Figure 86 shows fracture surfaces from three samples from the fracture study. A random mechanically repaired and laser repaired component were chosen as examples of fracture surfaces. From all three analytical techniques, no discernible difference could be seen in the fracture surfaces of any of the components in terms of topography, direction of crack propagation or repair surface crack initiation. Higher magnification equipment could be used to see more detail at crack initiation sites, however at magnifications up to 5000-10000x, where image quality was still acceptable, there were no obvious differences between these repair methods and the crack surfaces they generated.



**Figure 86 - a) mechanically repaired (6B), and b) laser repaired (7L) component fracture surface**

All samples shown in Figure 86 showed very similar fracture surfaces; with rough, brittle fracture surfaces being consistent from a short distance within the sample tip ( $\sim 100 \mu\text{m}$ ) to rest of the sample surface. Crack initiation sites were not obviously identifiable.

Figure 87 shows the knife-edge of the repair performed on sample 7L, as well as some of the larger grain structures visible within the crack. The fracture surface was consistent in topography from the crack tip to the crack end: large, flat grain facets with no obvious areas of crack growth as seen in Figure 87b. This suggests intergranular cracking, indicating the strengthening phases in the  $\gamma$  have remained largely unaffected by the repair process.

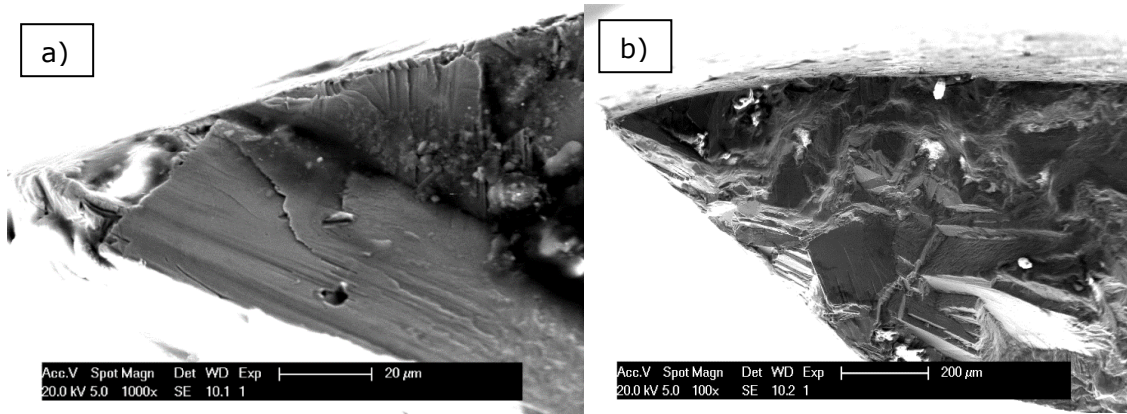


**Figure 87 - Fracture surface of sample 7L showing a) the blend knife edge, b) larger grain facets within the crack surface**

Boreblended samples showed similar fracture phenomenon to those seen in the laser ablated samples in previous images. Large flat fracture surfaces with varying heights were observed in crack tips of some components. By varying the working distance of the SEM detector, an estimate on crack feature height can be made by obtaining a focused image at different areas on the crack surface. For example, when two focussed images are taken at working distances of 10.6mm and 10.1mm, this gives a 500µm depth of crack feature.

Figure 88 shows a surface scan of component 7L. 3D data scans of the fracture surfaces were performed to characterise their topography. Fracture surfaces ranged from approximately  $\pm 350\mu\text{m}$  either side of a mean surface height. More severe undulations were seen towards the repair surface,

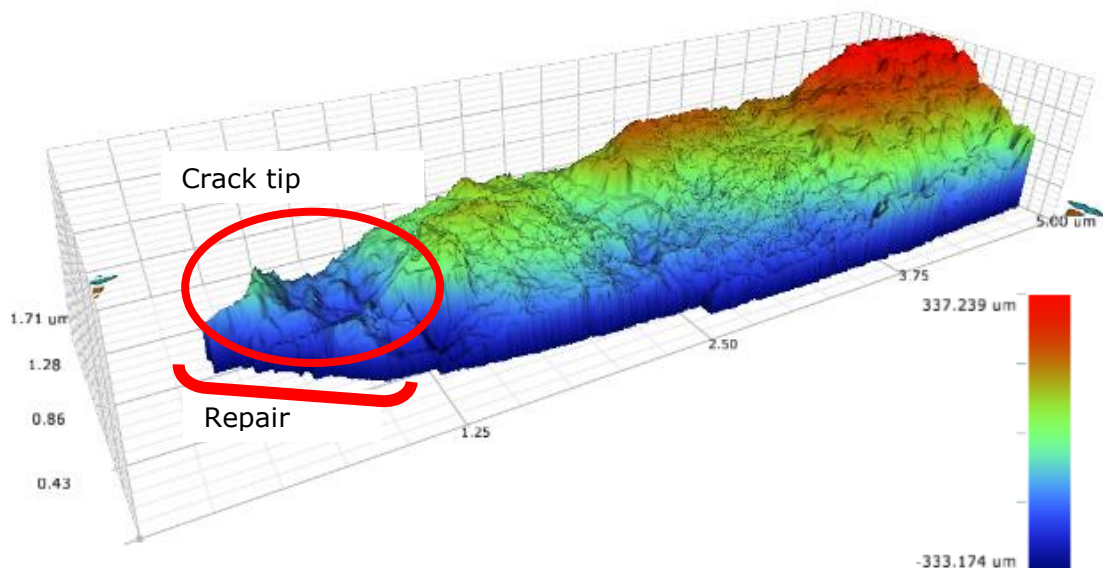


**Figure 88 - 3D surface data of laser repaired component 7L. X and Y axes scaled at  $1 \times 10^3 \mu\text{m}$**

## 7.8 Discussion

### 7.8.1 First set of HCF tests

- Material microstructure remains largely unchanged when laser processing is used, when compared to mechanically repaired components. The only easily observable change is material recast, and this falls within acceptable limits as defined in Rolls-Royce laser machining standards in every case. Fracture surface inspection confirms results seen in the metallurgical study.
- Performance of laser repaired components versus boreblended components generated in this experiment was comparable. Average fatigue performance (AF at  $10^7$  cycles) of components repaired with each method being 9.7% lower than those of mechanically repaired components.
- All fatigue samples performed at least as well as they were predicted to, with the poorest performing component (lowest AF  $10^7$  performance for laser components) still performing better than a laser repaired component was theoretically predicted to perform.
- MCF values for each repair type within the first set of HCF tests give the following conclusions
  - Mechanically repaired – A mean normalised MCF of 1.446 indicates that the repair process does not excessively reduce the failure strength of the component.
  - Laser repaired – A mean normalised MCF of 1.585 is higher than the minimum acceptable value defined by Rolls-Royce, and also higher than the mean MCF of mechanically repaired components. It should be noted however that direct comparison between laser and mechanically repaired components is not applicable due to their different geometries. Nonetheless, when comparing absolute failure levels (AF  $10^7$  strengths as opposed to MCF values), laser repaired components performed slightly worse than mechanically repaired components, but still more than the minimum acceptable value.
  - Larger spread in the fatigue life of laser repaired components was observed, and this is likely due to the nature of the laser repairs compared to the mechanically blended components. This may arise from the knife-edge feature of laser generated repairs, and the susceptibility of the repair surface to stress concentrators from

surface roughness. Variability in recast layer morphology and topography will also contribute to this spread, as recast generation is not directly controlled as a part of this process, but simply recast thickness is minimised.

### 7.8.2 Second set of HCF tests

- Samples from the second set of HCF tests showed similar results to those in the first set, where both repair methods resulted similar fatigue performance, but with AF  $10^7$  failure strengths higher than the minimum acceptable MCF value defined by Rolls-Royce, when compared to theoretical, failure strengths.
- Samples from trial 4 where 2 and 3 ellipses were created using the laboratory laser performed better than boreblended samples, with an increase in AF fatigue strength at  $10^7$  cycles between 2.8 and 6.1%.
- Blends created using the OpTek head with 3 laser ablated ellipses performed the worst, with a 14.8% reduction in fatigue strength compared to boreblended components. Compared to the most similar repair (3 ellipses blended using the laboratory laser), a 6.1% increase in fatigue strength was seen versus mechanically repaired components. Given the similarity between the repair geometries, the difference in fatigue performance is likely due to the processing method and the surface quality arising from these differences in equipment used to repair the components.

## 7.9 Fracture mechanics

Fracture surface analysis of all two component sets (laser and mechanically boreblended) showed similar crack behaviours. These include; crack initiation at the repair/leading edge of the blade, large undulations near the crack tip, marks caused by crack surface rubbing during testing, small and isolated areas of visible crack growth, and large flat grain facets indicating inter-granular crack growth. As these behaviours were consistent across all repair types, it can be safely assumed that there is no major effect on fracture mechanics by the repair method itself.

The few samples that failed in locations other than those expected were analysed to provide explanation for the difference in fracture behaviour. Due to the narrow bandwidth between neighbouring excitation modes, it was entirely possible that throughout the HCF test for some samples both modes may have been excited.

Repeatability of the geometry used in laser repairs was susceptible to variations in the geometry of the samples. As all the blades were engine-run, loading cycles and the stresses associated may have deformed the samples. As such when loaded into a machining jig for laser repairs, despite the very high repeatability in positioning of the laser scan path between repairs with respect to the machining jig, the leading edge of the blade may have been in a slightly different position each time.

GOM scans of components were performed to quantify variations in component geometry after being engine run. In comparisons of the scans for two blades used in this study, the geometry and relative position of the root of the blade is largely unchanged. However further away from the root, at certain places on the base and over the aerofoil larger deviations were seen. Specifically, the leading edge, where repairs are carried out, showed deviation in the order of half the blade width between the two blades. This is significant as deviation is coincident with the repair location, and as such significant variation in repair placement can occur.

## 7.10 Summary of HCF testing on repaired components

Sample repairs were successfully carried out using both laser ablation and abrasive boreblending. Laser scanning strategies from previous chapters were adapted to be performed by prototype equipment intended for in-situ repairs of components.

High cycle fatigue (HCF) testing of engine-run Trent XWB HPC blades repaired by laser ablation and mechanical boreblending, demonstrated the effect of various repair methods on the fatigue performance of components. Repeatability of the repair techniques affected the fatigue performance of the components, with variations in fatigue strength seen for similar repairs. This was likely brought about by geometric variations in engine-run components.

Laser and mechanically repaired components had similar fatigue strengths at  $10^7$  cycles, when repairs were placed in a location of high alternating stress at a pre-selected vibration frequency. Both repair methods produced components with fatigue strengths which were well above minimum strengths required by Rolls-Royce acceptance limits.

# Chapter 8. Sample blending with In-Situ Prototype Equipment

## 8.1 Introduction

In order to progress this project within Rolls-Royce, there must be a demonstration of the equipment intended for repair being used to generate acceptable repairs. This involves ablating real components with the pre-defined optimal machining parameters, and then testing them in high-cycle fatigue tests. The results of these tests are included in the previous chapter. This chapter will describe the process of repair using the prototype equipment produced by OpTek Systems, based in Oxfordshire UK. In addition, it will address any previously identified issues with the repair process and equipment, and any issues that arose in testing.

## 8.2 Spatial restrictions on repair equipment

Given the nature of In-Situ repair processes, repair equipment must be designed to fit in and around the machinery being repaired. As such the repair equipment to repair High-Pressure Compressor (HPC) components within the Rolls-Royce Trent XWB must be able to reach this area of the engine whilst it remains installed on the plane wing. All of the necessary technology must be delivered to the target area to effect the repairs. For this application, the most important requirement is the delivery of a steerable, focused infra-red laser beam to the area. The intended solution from the project's inception, was for the repair equipment to be delivered through external inspection ports, and guided to the target area using a deployment probe built specifically for the target rotor stage within the HPC module. The bespoke deployment probe can be rigidised to support the optical systems with reliable and repeatable positional accuracy. Additional inspection equipment can be used, inserted through other inspection ports or through the front end of the engine to provide an external view of the repair equipment and target component. The inspection port allows for a tool with a maximum diameter of 12mm to be inserted into the engine. A prototype of the deployment probe and optical guidance system is shown positioned within a representative engine assembly in Figure 89 .

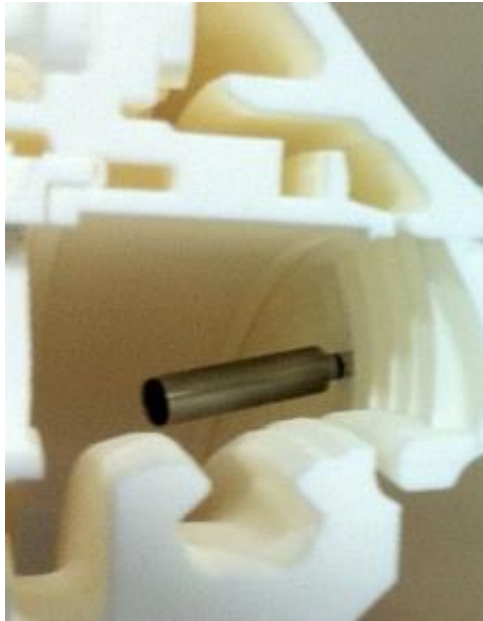


**Figure 89 – Dummy OpTek laser head deployed in representative engine assembly**

### 8.3 Repair geometry

The repair geometry used for generating repairs with the OpTek equipment was the same as that described in Chapter 7. Given the size of the equipment that can be delivered to the target component, there is a restricted optical window available for machining. As such, the repair must be made with multiple machined ellipses as detailed previously.

### 8.4 Side effects of repair

The repair process has implications for the life of both the components being repaired, and the equipment being used to effect these repairs. The previous chapter deals with the effects of repair on the components, through high cycle fatigue testing of a range of repair geometries.

Through machining components, ejected material was identified as a potential cause for additional failure. This may be through larger particles damaging internal mechanical/optical components, or smaller particles obscuring the optical window for laser light passage onto the component reducing machining efficiency. Figure 90 shows this material ejection from the component surface.



**Figure 90 - Material ejecta generated during machining of components**

## 8.5 Methodology

### 8.5.1 Component Alignment

Components were placed in an epoxy resin cast, holding the blade leading edge at a  $90^\circ$  angle to the laser beam. Reference blocks were placed on an optical bench to give a reference for relocation of the epoxy cast with respect to the laser beam for repeatable positioning of the component, shown below in Figure 91. For minor readjustments (due to variation in component geometry explained in Chapter 7), an XYZ micrometre stage was used to move the optical head in three dimensions. Alignment was done by eye, using a red pointer laser fed coaxially through the optical fibre carrying the infra-red machining laser beam. Focal positioning was also done by eye, with test samples being used to confirm focus with the machining laser beam.

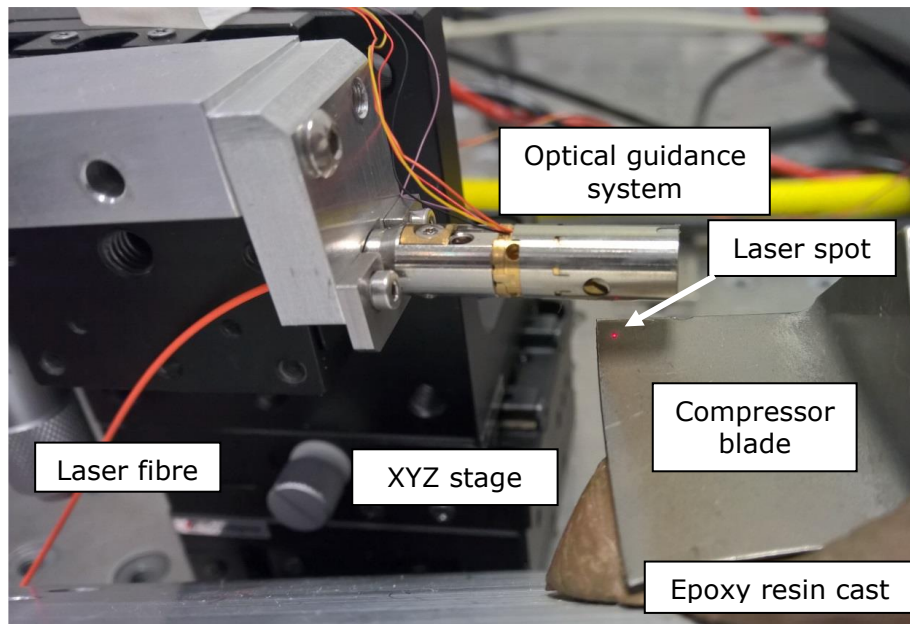


**Figure 91 – HPC blade held in epoxy resin cast for sample alignment underneath optical guidance system for laser beam**

### 8.5.2 Scan path generation

Repair geometries were generated using 3 separate ellipses, each individually programmed into the control system of the beam guidance system and the laser module. Ellipses were machined through the sample completely before moving the optical head to generate the next ellipse. Ellipses were placed in the same location as those detailed in Chapter 7. Marking was done using Vernier callipers and ink markings to indicate the edges of the area to be repaired.

### 8.5.3 Bulk material removal

For the majority of the machining of repair ellipses, a spiral scan path was repeated until a complete 2.5D feature had been machined into the sample. Scan draw times were set to a constant 1 second, with 20 loops per ellipse at a fixed ellipse radius. To protect the optical components from excess thermal build-up, a duty cycle was put in place. The laser beam was set to fire for 5 seconds, with a 2 second pause to dissipate heat within the head. During this time, the scan paths were still traced, however this should have caused no problems with laser beam firing and positioning becoming desynchronised as 5 complete scans were traced with the laser firing per duty cycle.

Ellipses were ablated for a period of time long enough to ensure thorough material removal within the scan area, and consistent blend surface quality across all repairs. Some test samples were also prepared with longer ellipse ablations, up to

3 times the aforementioned blend time, resulting in visible thermal damage to the component. As such the shorter length of time, which resulted in thorough material removal with consistent blend quality, was used for samples submitted for HCF testing. Laser current was adjusted in the OpTek laser control UI such that 13W of power was measured at the laser output (using a CCD power meter) and pulse repetition frequency was 35kHz.

#### 8.5.4 Blend surface polishing

As an additional study, some samples were ablating with varying bulk material removal scan times, and then a polishing scan path using a different set of machining parameters in an attempt to create higher surface qualities on the blend. These were purely speculative trials and were not used for submission to HCF tests. This scan path allowed for a more concentrated ablation of the blend surface, resulting in any excess metal being removed. An epitrochoid shape was used to generate a polishing path.

#### 8.5.5 Capture of ejected materials

To characterise the direction, volume, and size of ejected particles from the component surface onto the equipment optical window, an extra study was conducted. Laser machining parameters used were representative of the blending process, with laser power, frequency and scan speed set as described in section 0. This was performed on the laboratory bench laser to avoid unnecessary damage to the limited number of working optical heads constructed by OpTek. A 3D printed tower was constructed to hold glass cover slips above an INCONEL<sup>®</sup> 718 sample at known Z offsets. An ablation pattern was created on the sample, and ejected material was captured on the glass cover slips for analysis. Figure 92 shows how ejected material was captured from ablating an INCONEL<sup>®</sup> 718 sample. These cover slips were then placed in an SEM for physical and chemical characterisation in the same manner as HCF and metallurgical samples in previous chapters.

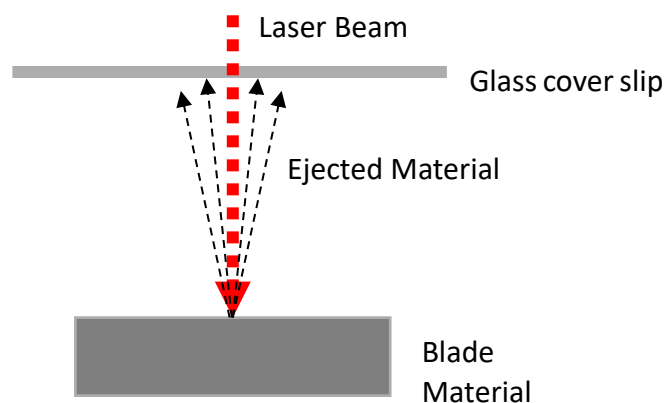
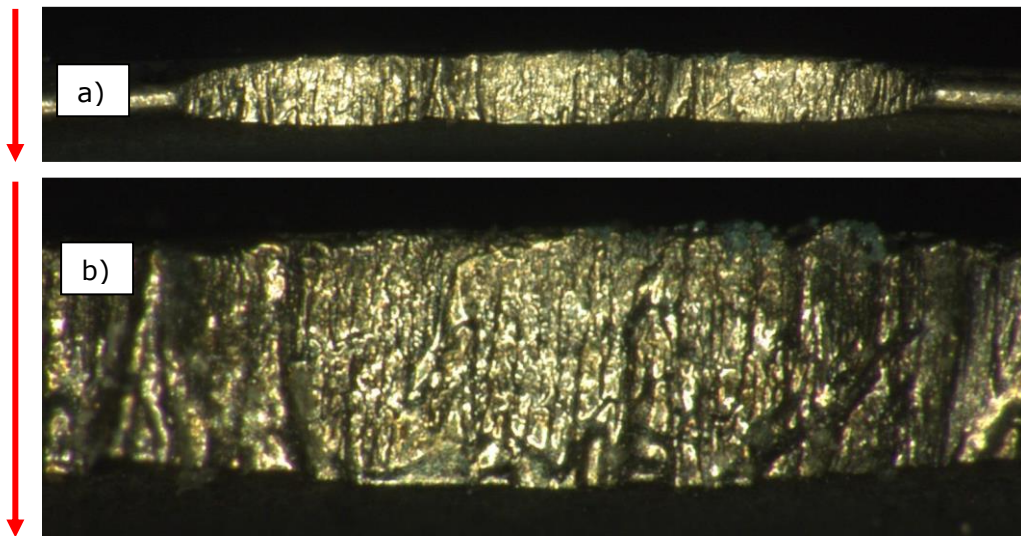


Figure 92 - Glass cover slip capture of ejected material from ablation

## 8.6 Results

### 8.6.1 Repair quality, performance and repeatability

Blend surfaces were examined under an optical microscope immediately after the blending process. In both the whole blend surface and close up images shown in Figure 93, the laser beam was machining through the blade from the top of the image to the bottom as shown with a red arrow. The finished surface was rough with large recast/molten surface structures towards the exit side of the blend (bottom of the images). This surface quality was consistent across all repaired components, with minor variation when different optical heads were used.



**Figure 93 - a) Surface of a 3 ellipse blend, b) Close up of a single ellipse**

Figure 94 shows a range of polished blend surfaces using varied polish scan path times. A rough cut was done on the blades for 1/3 of previously defined bulk blend times sufficient to fully ablate through the blade edge. As can be seen in all images in Figure 94 this was not sufficient to completely machine through the thickness of the blade, and there is a large un-ablated bulk of material at the bottom of the blend surface.

After the bulk material removal scan had been completed, a second laser scan was performed to polish the blend surface. A range of scan path durations were performed for this secondary scan to assess the extent to which the blend surface could be improved. As shown in Figure 94b, even polishing for 1/3 of bulk blend time gave a visually smooth surface when compared to the unpolished cuts shown in Figure 93. Increasing the polish scan time from 1/3 to 2/3 of bulk blend time (Figure 94c) and full bulk blend time (Figure 94d), surface quality does not appear to improve but discolouration starts to occur, especially after polishing for a further amount of time equal to a full bulk removal scan. This is likely oxidation as the

surface is being held at a constant, high temperature for an extended period of time.

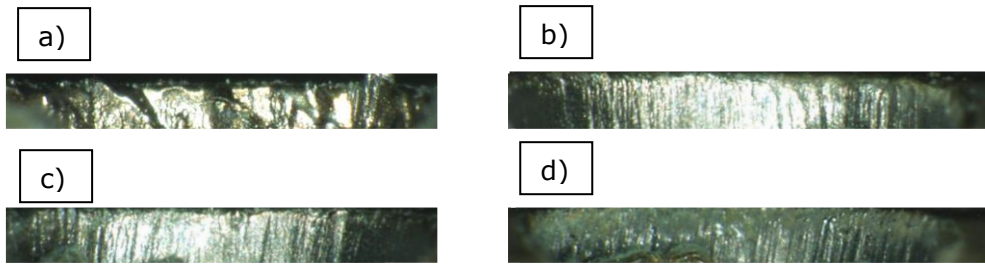


**Figure 94 - Blend surface after a) 1/3 of normal bulk blending time, and 1/3 of bulk blending time followed by polishing for b) 1/3 c) 2/3, d) 1x of bulk blending time**

### 8.6.2 Analysis of ejected materials

Ejecta was captured on glass cover slips held at known distances above the workpiece as shown below in Figure 95. It should be noted that at all capture distances (10, 15, 20, 25mm) ejecta ricochets could be observed. Screen captures of video footage such as Figure 95 show this, where an ejected particle reflects off the plastic component and then the glass slide.

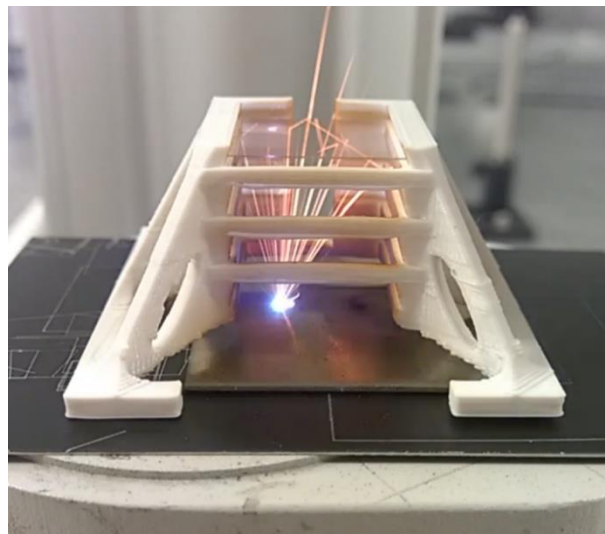


**Figure 95 - Glass cover slip tower capturing ejected material during ablation process**

Figure 96 shows glass slide coverage after constant ablation for a time period discussed in section 0, at normal machining parameters used for the repairs. It should be noted that the volume of air above and around the workpiece was somewhat restricted, with limited airflow due to the walls of the plastic mounting module. The OpTek equipment does not restrict airflow around the sample as much, and as such smaller "soot" like particles, seen particularly in the slide closest to the surface might disperse more readily.

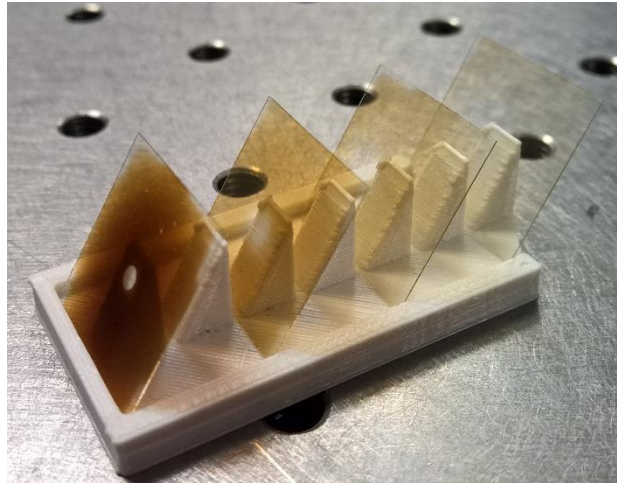


**Figure 96 – Glass cover slip coverage with 10, 15, 20, 25mm workpiece offset from left to right**

Upon inspection of the glass cover slips, it was found that the reddish-brown "soot" like substance that covered the majority of the slide wiped off with ease. In addition, wherever the laser scan path was coming through the glass slip, this substance was either not settling, or being cleared by the laser beam itself. As such, this substance was deemed to pose no threat to the longevity of the equipment or the efficiency of the laser machining process.

Glass cover slips were put under SEM inspection for qualitative analysis, and to identify the chemical composition of ejected material. Larger particles were chosen for analysis as these were the ones that settled on the glass surface, and did not wipe off easily unlike the soot like substance

Figure 97a shows a back-scattered electron image of a typical ejected particle. It has a diameter of approximately 40-50 $\mu\text{m}$ . This is roughly the maximum size of particles found on the glass surface. Embedded within the particular deposition around this larger object are smaller particles, less than 5 $\mu\text{m}$  in diameter. The other images in the figure above show distributions of three chemical elements within the image, Aluminium Nickel and Iron respectively. It can be seen that the large particle itself consist of almost exclusively Aluminium (shown in Figure 97b). It should also

be noted that there are smaller aluminium particles surrounding the larger particle, a few micron in diameter.

Figure 97c and d show some smaller particles of a mixture of both nickel and iron. These particles appear at the same location in both chemical maps, hence it can be assumed that these particles are comprised of a mixture of these 2 metals.

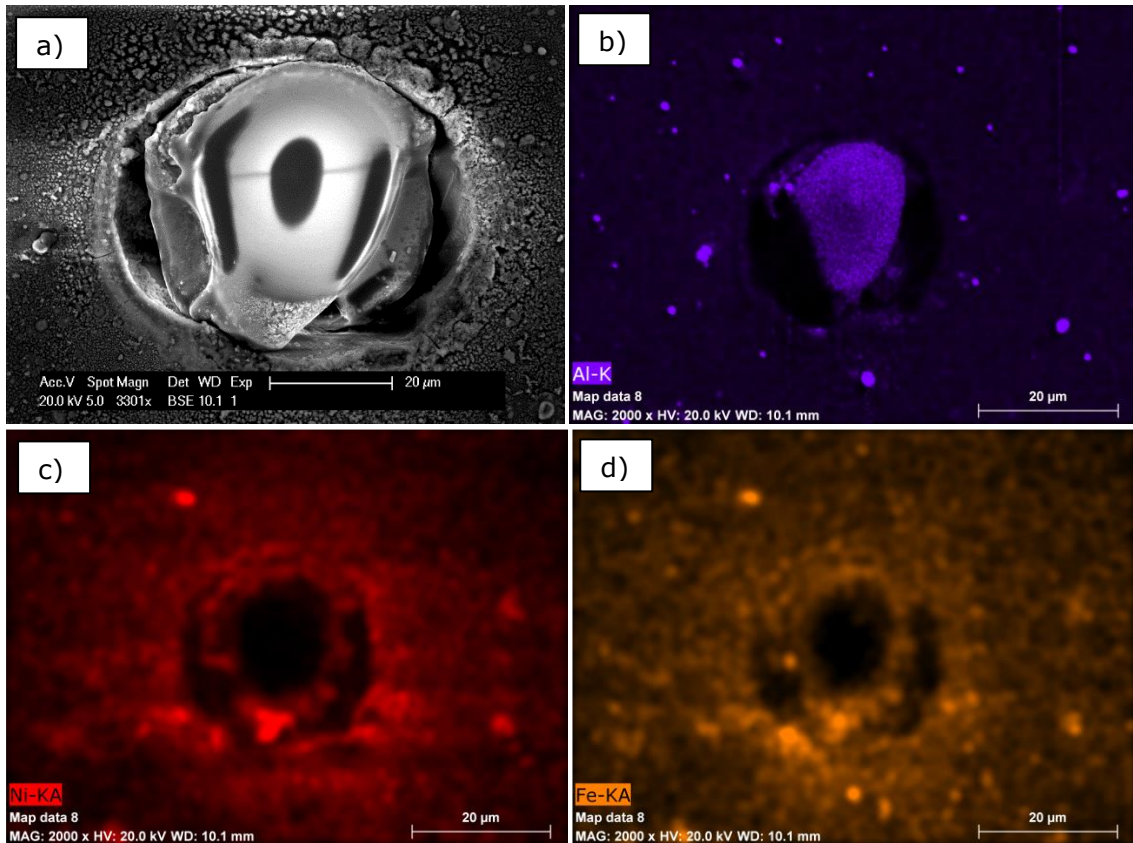


**Figure 97 - SEM Imagery of a) Ejected particle embedded into glass surface, EDX mapping for b) Aluminium, c) Nickel, d) Iron**

Figure 98 shows chemical mapping for the same particle as seen in Figure 97, for three additional elements; Molybdenum, Niobium and Chromium. These three elements have settled in a ring around the particle impact area, with the elements in highest concentration being Molybdenum and Niobium. The mapping for Chromium, shown in Figure 98c is less sharp in the area around the larger particle, and as such it is safe to assume that there is minimal chromium settling here. It should however be noted that the same locations in Figure 97c and d, where Nickel and Iron are shown to have settled together, are also bright spots in the Chromium map, suggesting that these settled particles consist of Iron, Nickel, and Chromium.

- The three distinct patterns of ejecta deposition seem to follow to some extent the atomic numbers (Z) of the settled materials, and their period (row of the period table in which they appear).
- Large particle and smaller particulate spattering; Aluminium (Z = 13), chemical period 3
- Smaller, mixed element particulate spattering; Chromium (Z = 24), Iron (Z = 26), Nickel (Z = 28), all chemical period 4
- Ring settling around the larger particle; Niobium (Z = 41), Molybdenum (Z = 42), chemical period 5.

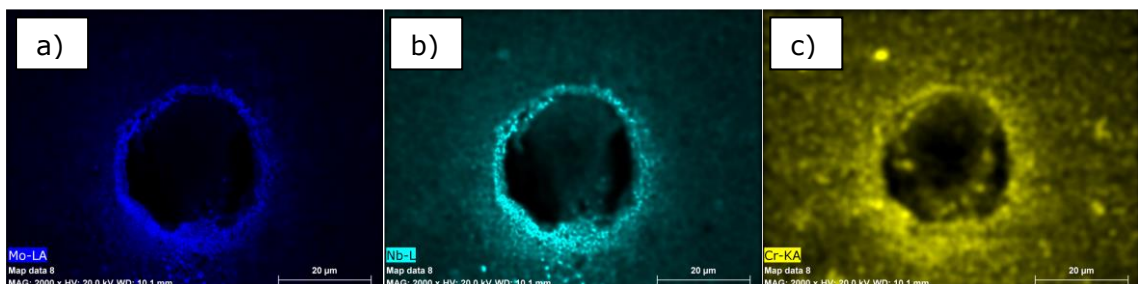


**Figure 98 - EDX mapping for a) Molybdenum, b) Niobium and c) Chromium**

## 8.7 Discussion

### 8.7.1 Blend Surface Quality

Blade inspection showed that there was minimal effect on surface roughness when tripling bulk blend times. 1/3 of bulk blending time was also shown to be insufficient to machine all the way though the blade thickness. Significant surface quality improvement was seen when using a polishing scan path on top of a bulk removal scan. Polishing time equal to 1/3 of bulk blending time was long enough to gain significant improvement, and is speculated to be sufficiently short enough to avoid oxidation of the blend surface.

### 8.7.2 Ejected materials

SEM and EDX analysis showed a distribution of particles up to approximately 50 $\mu$ m in diameter. These particles were found to consist mainly of pure Aluminium, with smaller clusters of particles and spatter around larger impacts consisting of Iron, Nickel, Chromium, Niobium and Molybdenum.

Given the composition of the common phases in the sample material, such as  $\gamma'$  and  $\gamma''$ , the lack of nickel in the observed localised depositions on the slide surfaces suggests separation of Nickel and other elements within the alloy by melting. These strengthening phases are obtained by specific heat treatment strategies [77], [78]. The ejected material particles observed are likely to be solidified re-melted material, due to the thermal processes involved in ablation. This re-melted material is cooled rapidly, when compared to a standard heat-treatment cycle for this alloy (usually performed over many hours). This rapid cooling causes granular precipitates to form which are not gamma phases, but compound phases such as Nb and either Al or Ti [79].

A red-brown soot like covering on the glass cover slips was found in areas where the laser beam was not passing through. In those areas where it did settle, it was easily wiped off with either a paper towel or an air duster.

# Chapter 9. Overall discussion

This chapter will discuss, summarise, and draw conclusions on the observations made throughout this thesis in each chapter, and it will give recommendations and suggestions for further work which could be done to build upon findings and developments made throughout this project.

## 9.1 Discussion of project objectives

The work described in this thesis has addressed one or more of the project objectives as described in Chapter 1. The following points will address how each of the project objectives has been met.

### 9.1.1 Achieving material removal with the proposed laser system

Material removal was achieved on Rolls-Royce compressor components by using a pulsed Yb:YAG laser with a 200ns pulse duration. Laser scan paths were generated to machine repair geometries as described in Chapter 1. By overlaying of successive pulses, complete volumes of material were removed as opposed to simply cutting material away with a resultant blend profile which matches those generated by current mechanical blending practices. By fully removing the repair volume in the component by overlapping laser ablated craters, there is minimal material redistribution onto other components or into the engine gas stream. During ablation, the majority of the removed material was ejected as plasma with a small fraction being ejected as molten material. Some of the removed material was redistributed onto the component surface.

### 9.1.2 Minimise material damage caused by laser machining

A design of experiments approach was used to investigate the effect each key process variable had upon the negative secondary effects either on or near the component surface being ablated. Material recast, oxidation, cracking and metallurgical changes were the effects being investigated in Chapter 4. Each of these secondary effects were quantified and compared with Rolls-Royce documentation to ensure repairs would conform to acceptance standards for laser machining. Negligible cracking and oxidation was seen across almost all trials conducted in this chapter, where significant oxidation was only seen in very small, localised locations across material surfaces where the most aggressive laser machining parameters had been used (high pulse energy and low scan speeds).

With the criteria for laser repairs described in Rolls-Royce CME033/5/E1 [1], values for each of the key process variables were chosen such that each of the secondary effects observed would be within acceptance limits.

- Little to no cracking was seen within recast layers, and no parent material cracking was observed in any of the trials performed.
- Outside of the most aggressive machining parameters, creating high pulse energies and thermal input to the workpiece, the majority of ablated samples had maximum recast thicknesses well within acceptance limits shown above.
- Recast globules were not observed in any significant volume, and almost all detected recast material was attached to the recast layer on the parent material. With recast layer thickness measured at under 20 $\mu\text{m}$  for the majority of cases, any separated recast globules were much smaller than the 65 $\mu\text{m}$  diameter required for repair rejection.
- Surface undulations within trials where low recast was seen were also low, with recast layer thickness itself being lower than the 40 $\mu\text{m}$  rejection criteria.
- Very isolated cases of oxidation were seen in trials with aggressive machining parameters, and as such oxidation was not considered to be of any significant concern within these trials.

In addition to the low incidents of negative secondary effects listed above, there was little to no observed morphological change noted in terms of metallic phases, beyond the isolated cases of oxide phases being generated. In avoiding the generation of weaker delta phases, or changes in grain size through melting and recrystallization, the component was able to maintain much of its metallurgical strength and integrity from before being laser ablated.

Having carried out the experiments described in Chapter 4, there is evidence to show that the laser system chosen can produce repair features in Nickel superalloys whilst the extent of negative secondary effects brought about through the machining process is well below that which would cause concern, or result in immediate rejection.

### 9.1.3 Mathematical modelling of ablated features and surfaces

A mathematical model was developed to predict the evolution of surface topographies on a known target material with processing by a known laser system.

A calibration method was developed to characterise the material response in terms of ablation depth, and this was used to build a pulse-by-pulse representation of the material surface, as various machining phenomenon such as laser beam divergence and material redeposition were also considered. This gave the capability to model in materials where material recast is present, such as Nickel superalloys. Modelling processes where material redeposition is present in metals, and those where it is not present in machining of diamond resulted in good accuracy when the model was validated. Errors below 9.39% were observed in diamond modelling, and as low as 1.3% for modelling nickel alloy ablation where material redeposition was included.

#### 9.1.4 Maximising material removal rate for repair geometries

Through combining findings made in the metallurgy study (Chapter 4) and the mathematical modelling of the surface ablation (Chapter 5/Chapter 6) process optimisation was made possible. In simulating the material removal of the processes which offer the best metallurgical structures and morphologies as found experimentally, a process which will give maximal material removal rates with minimal negative secondary effects can be identified. This was determined to be machining at 15W, 25kHz-35kHz (dependent on whether the SPI G3.0 or a later laser system was used), and 400-700mm/s to maintain a square pulse placement matrix (also dependent on the laser system in use).

#### 9.1.5 Mathematical model validation on diamond and nickel targets

Further development and validation of the model was done in Chapter 6 to extend its predictive capabilities;

- Micro-scale complex geometries were modelled where in addition to varying values for each of the three key process variables (laser power, pulse frequency, and scan speed), scan path variables such as number of scan repetitions and laser track offsets were considered. Errors as low as -0.34% were observed, and secondary features such as ablated track peaks/troughs were modelled with good accuracy.
- Macro-scale large geometries were also modelled and produced experimentally in an On-The-Fly component balancing scenario. This gave the model its validation in a real process, where a target mass was to be removed from the component. When machining an optimised geometry, as calculated with the mathematical model, mass errors as low as 1.38% were observed.

### 9.1.6 Quantify repair-induced fatigue changes

Residual stresses induced by the laser processing was measured and quantified by use of X-Ray diffraction techniques, as described in Chapter 4. No trials produced excessive stresses, with a maximum measured being approximately 900MPa. Surface roughness was also measured as it is known to be an exacerbating factor when fatigue strength loss is considered. Using optimised machining parameters as calculated through work in Chapters 3-5, laser ablated repairs were generated in engine-run components to reflect real life service conditions and repair implications which can be expected in future. Two separate iterations of the prototype repair tooling were considered, where a 45° and 90° angle of incidence onto the blade leading edge was reproduced using both a laboratory setting, and a real prototype optical head for a 90° angle of incidence. For each laser repair being tested, up to 10 identical repairs (in terms of laser parameters and scan paths) were created to compare against mechanically repaired components. Each of these mechanically repaired components also had up to 10 samples submitted for each trial. Fatigue life was measured and extrapolated using industry standard S/N curves to a life of  $10^7$  cycles, and the calculated fatigue strengths were compared.

For 45° repairs created using a bench laser system, laser repairs had a fatigue strength reduction of 9.7% when compared to mechanically repaired components.

For 90° repairs created using a bench laser system, laser repairs had a fatigue strength up to 6.1% higher than those created by mechanical blending.

For 90° repairs created using prototype repair equipment, the lowest fatigue strength was seen at a 15.2% reduction versus mechanically components.

All of the laser blended samples performed better than the minimum acceptable limit as set by Rolls-Royce. As such, confidence can be put in both laser ablation as a machining process, and the proposed equipment for repairs as viable options for In-Situ maintenance of these components.

### 9.1.7 Operation and failure mode investigation of OpTek optical head

Successful operation of prototype repair equipment was described in Chapter 8, with a range of repair geometries and scan path types being generated in aero engine compressor components. Further work was also performed to identify potential improvements to this process, such as polishing of the blend surface to reduce roughness and hence in theory, improve fatigue strength.

Chemical analysis was performed on ejected material from the repairs as a way to address concerns and questions surrounding where the removed material will go, and if it will negatively affect the performance of the repair equipment. Particle sizes were measured and found to be in the order of 10-40 $\mu$ m, with additional settling of a "soot" like substance, most likely condensed material plasma. This material was easily removed with air dusting or wiping with a cloth or tissue.

This work demonstrated the capabilities of the prototype equipment and showed its ability to generate the repair geometries as required. It also served to highlight potential issues and areas for improvement in future design iterations of the equipment.

## 9.2 Future Recommendations

The work carried out throughout this project has contributed to a range of academic and industrial advancements, however there are also lessons that can be learned and used as a basis for future work, where further learning and advancement can be made.

### 9.2.1 Laser system options for reduced material recast

Through the metallurgical experiments performed in this project, as well as with information gathered in the literature review of this thesis, it is clear that using nanosecond pulse durations will result in some degree of material redeposition. Whilst for this project this has not been a major issue, as Rolls-Royce acceptance limits are much higher than the levels of material recast observed experimentally, it may be of concern in future developments of this project, or other projects that arise from it. Minimising material recast as a project objective may involve using another laser system, and as shown in the literature this may be achieved by using shorter pulse duration laser systems. Femtosecond pulses present little to no material recast, and as such would be potential alternative option for this application, however the lower material removal rate may limit the size of features being ablated and as such work would be required in a similar fashion as presented in this thesis, to maximise material removal rate whilst maintaining low material recast and damage. Additionally, these systems would typically cost more than a nanosecond laser system as proposed for use in this system, and as such a business case review would also be necessary to justify this increased cost.

### 9.2.2 Mathematical modelling improvements for material recast characterisation

The mathematical model presented in Chapter 5 demonstrated good accuracy when predicting simple features given initial calibration, whilst varying laser power, pulse frequency and scan speed. There was also promising validation results on the model when taking material redeposition into account, however this was for a single laser scan pass and with only consecutive pulses overlapping and hence only two pulses worth of material redeposition being considered and accumulating. With the approach used to model this redeposition using interpolation on a trend line created from measured material redeposition features in experimentally created craters at a range of laser fluences, there is limited scientific accuracy for modelling this phenomenon in more complex scenarios. In the case where there may be many pulses redistributing material on top of the same location, or where previously redistributed material may be hit by a later pulse whilst it has not fully cooled, additional effects may be present which are not accounted for in the current model. As such, a multi-physics approach using fluid dynamics and thermodynamic properties of the material such as temperature dependent viscosities, latent energies etc., this model would be far more accurate when modelling metal ablation where high degrees of material redeposition is observed.

### 9.2.3 Reducing loss of fracture surface detail during testing and preparation for analysis

Fractured high cycle fatigue samples were separated into halves after testing to allow inspection of the fracture surfaces. This was done in a manner to preserve as much of the fracture surface as possible and prevent any rubbing or grinding of fracture planes/features. Despite this, a noticeable amount of fretting and rubbing artefacts were found during SEM inspection. Upon discussion with experts within Rolls-Royce, it was suggested that this may be due to the vibration mode being used to stress the samples, and the transverse oscillations that this would induce in the component material either side of the fracture surface after the component had cracked. As such, the inherent vibration of the component under loading was causing some loss of fracture surface detail. Therefore investigation into alternative loading schemes where post-fracture component deformations do not cause loss of fracture surface detail may be beneficial.

#### 9.2.4 Increasing the range of data available from high cycle fatigue testing

High cycle fatigue testing was carried out on components with one repair geometry, in one specific location under one specific set of loading conditions. By varying the repair geometry, location and loading frequency and stresses, more information can be gathered on how laser blending affects component performance.

#### 9.2.5 Improving inspection and analysis methods for high cycle fatigue specimens

Fracture surfaces were inspected under FEGSEM equipment, with preparation in an ultrasonic bath prior to inspection. With the training given and the equipment available, it was difficult to obtain clear images of the fracture surfaces at magnifications above 5000x, which is typically too low for resolving small fracture plane details which are sometimes in the nanometer scale. With further training and access to equipment capable of resolving smaller details at higher magnifications, more information about the fracture mechanics present in the failure of high cycle fatigue specimens, such as crack initiation and growth rates, may be attainable.

# Chapter 10. Conclusions

Pulsed laser ablation was identified as a viable machining method for removing material in high-pressure compressor blades made from a nickel superalloy, commonly used in aero engine compressors.

A review of literature regarding laser machining and characterisation of nickel superalloys has identified a number of metallurgical changes that negatively impact upon the mechanical properties of the material, such as generation of weak  $\delta$ -rich phases or oxygen dissolution into the material in the form of nickel or iron oxides.

A design of experiments approach was used to assess the interaction between pulsed laser light and INCONEL<sup>®</sup> 718 (a nickel superalloy) targets, and its effect on both metallurgical changes within the target surface (such as phase change and oxidation), as well as topographical changes (such as surface roughness and material redeposition).

Mathematical modelling was adopted to simulate the surface texture of a material undergoing pulsed laser ablation. CVD diamond was used as a control material as it did not present secondary effects from the ablation process such as material redeposition. Both nanosecond and picosecond pulse durations were considered in this model to cover a range of ablation regimes as described in the literature review. This model was extended to INCONEL<sup>®</sup> 718 ablation, where material redeposition was present. Validation of the model was performed on both individual and overlapped tracks of ablated craters, showing accuracy in ablated depth prediction and intra-track features such as localised peaks and valleys.

Having developed a database of material responses to varying KPV values, prediction of material removal rate using the previously mentioned mathematical model allowed a set of optimised parameters to be determined for the ablation of INCONEL<sup>®</sup> 718 where a compromise between minimised material recasting/oxidation and material removal rate was required. These were an average laser power output (programmed in software) of 15W and a pulse repetition frequency and scan speed of either 25kHz and 400mm/s, or 35kHz or 700mm/s. These KPV values offered a quick repair machining time, whilst generating no significant oxide phase within the surface layer or inducing any significant phase change away from the bulk material microstructure, and minimal material recasting

to a thickness well within Rolls-Royce's acceptance limits for laser machining of nickel superalloy components.

These process parameters were used to generate blends in engine-run components, and then these repaired components were assessed through high cycle fatigue testing for changes in fatigue strength in comparison to mechanically repaired components machined according to best-practice standards. All of the work leading up to this point resulted in a set of repaired components which demonstrated that pulsed laser ablation could be used to produce blends in high stress areas of components, that would not detrimentally affect the integrity of the component in terms of chemical or stress-concentrating features, and that it could produce these repairs in a time much faster than those performed with mechanical boreblending. Furthermore, these repairs had fatigue strengths comparable to those performed with mechanical boreblending, and well above a minimum acceptable fatigue strength as defined by Rolls-Royce.

Through adaptation of laser blending scan paths, this system was used to generate repairs in engine-run components, and has shown successful repair generation in this respect. These components were also assessed with HCF testing, and demonstrated a fatigue strength comparable to blends produced using the laboratory laser equipment.

As such, this project has delivered a knowledge base and set of processing parameters that demonstrate the viability of pulsed laser ablation for use in in-situ repair of nickel superalloy compressor components. Not only has the process of pulsed laser ablation been validated against a set of acceptance criteria set by Rolls-Royce with regards to metallurgical changes, but it has also been demonstrated to produce repairs with fatigue strengths comparable to best-practice mechanically blended components. To this end, pulsed laser ablation has been demonstrated as a viable accompaniment to mechanical boreblending, expanding the tools and techniques that may be used for in-situ repair of aero-engine components.

# References

- [1] Rolls-Royce Plc, "Surface Standards for Laser Machining CME5033/5/E1," 2011.
- [2] R. Thamburaj *et al.*, "Life Cycle Management Strategies for Aging Engines," 2001.
- [3] U.S. Department of Transportation and FAA, "Chapter 8 - Inspection Fundamentals," 2008.
- [4] Rolls-Royce Plc, "Engine IP and HP Compressor Repair the Damaged Compressor Aerofoils by Boroblending - FRSB5511," 2011.
- [5] O. Yilmaz, N. Gindy, and J. Gao, "A Repair and Overhaul Methodology for Aeroengine Components," *Robot. Comput. Manuf.*, vol. 26, no. 2, pp. 190–201, Apr. 2010.
- [6] G. P. Sabol and R. Stickler, "Microstructure of Nickel-Based Superalloys," *Phys. status solidi*, vol. 35, no. 1, pp. 11–52, 1969.
- [7] J. F. Radavich, "The Physical Metallurgy of Cast and Wrought Alloy 718," *Superalloys 718 Metall. Appl.*, pp. 229–240, 2004.
- [8] M. Doi, D. Miki, T. Moritani, and T. Kozakai, "Gamma/Gamma-Prime Microstructure Formed by Phased Separation of Gamma-Prime Precipitates in a Ni-Al-Ti Alloy," *Superalloys 2004 (Tenth Int. Symp.)*, pp. 109–114, 2004.
- [9] K. H. Leitz, B. Redlingshöer, Y. Reg, A. Otto, and M. Schmidt, "Metal ablation with short and ultrashort laser pulses," *Phys. Procedia*, vol. 12, no. PART 2, pp. 230–238, 2011.
- [10] ASM International, *Elements of Metallurgy and Engineering Alloys - Google Books*. 2008.
- [11] W.-S. Lee, C.-F. Lin, T.-H. Chen, and H.-W. Chen, "Dynamic Impact Response of Inconel 718 Alloy under Low and High Temperatures," *Mater. Trans.*, vol. 52, no. 9, pp. 1734–1740, 2011.
- [12] A. Fatemi, "Residual stresses and their effects on fatigue resistance," *Univ. Toledo*, pp. 1–48.

- [13] P. S. Prevéy, "X-ray diffraction residual stress techniques," *Met. Handbook. 10. Met. Park*, no. 513, pp. 380–392, 1986.
- [14] S. Biswas, M. D. Ganeshachar, J. Kumar, and V. N. S. Kumar, "Failure analysis of a compressor blade of gas turbine engine," *Procedia Eng.*, vol. 86, pp. 933–939, 2014.
- [15] ATSB Transport Safety Report, "Power plant failures in turbofan-powered aircraft," no. June, 2008.
- [16] W. T. Silfvast, *Laser Fundamentals*, 2nd ed. Cambridge University Press, 2004.
- [17] R. Paschotta, *Encyclopedia of Laser Physics and Technology*. Wiley-VCH, Berlin, 2008.
- [18] University of Rochester, *Progress in Optics*, 46th ed. 2004.
- [19] A. E. Siegman, "Defining, measuring, and optimizing laser beam quality," *Proc. SPIE*, vol. 1868. pp. 2–12, 1993.
- [20] H. Li, S. Costil, V. Barnier, R. Oltra, O. Heintz, and C. Coddet, "Surface modifications induced by nanosecond pulsed Nd:YAG laser irradiation of metallic substrates," *Surf. Coatings Technol.*, vol. 201, no. 3–4, pp. 1383–1392, Oct. 2006.
- [21] O. Svelto, *Principles of Lasers (5th Edition)*. 2010.
- [22] Laser 2000, "System Components for Integrators," 2010.
- [23] Scanlabs, "Installation and Operation The RTC ® 5 PC Interface Board and RTC ® 5 PC / 104- Plus Board," pp. 1–467, 2010.
- [24] R. V. Steele, "LASER MARKETPLACE 2008: Diode lasers track long-term trend - Laser Focus World," *The Laser Focus World 2008 Annual Review*, 2008. .
- [25] R. A. Haight, P. Longo, H. Junction, and P. Morris, "Method for minimizing sample damage during the ablation of material using a focused ultrashort pulsed beam," 2001.
- [26] M. C. Kong, C. B. Miron, D. a. Axinte, S. Davies, and J. Kell, "On the relationship between the dynamics of the power density and workpiece surface texture in pulsed laser ablation," *CIRP Ann. - Manuf. Technol.*, vol. 61, no. 1, pp. 203–206, Jan. 2012.

- [27] A. K. Dubey and V. Yadava, "Laser beam machining—A review," *Int. J. Mach. Tools Manuf.*, vol. 48, no. 6, pp. 609–628, May 2008.
- [28] I. Bozsóki, B. Balogh, and P. Gordon, "355nm nanosecond pulsed Nd:YAG laser profile measurement, metal thin film ablation and thermal simulation," *Opt. Laser Technol.*, vol. 43, no. 7, pp. 1212–1218, Oct. 2011.
- [29] N. A. Vasantgadkar, U. V. Bhandarkar, and S. S. Joshi, "A finite element model to predict the ablation depth in pulsed laser ablation," *Thin Solid Films*, vol. 519, no. 4, pp. 1421–1430, 2010.
- [30] J. Cheng *et al.*, "Ablation mechanism study on metallic materials with a 10ps laser under high fluence," *Appl. Surf. Sci.*, vol. 255, no. 18, pp. 8171–8175, Jun. 2009.
- [31] C. Momma, S. Nolte, and B. Chichkov, "Precise laser ablation with ultrashort pulses," *Appl. Surf.*, pp. 15–19, 1997.
- [32] G. Dumitru, V. Romano, H. P. Weber, M. Sentis, and W. Marine, "Femtosecond ablation of ultrahard materials," vol. 739, pp. 729–739, 2002.
- [33] B. Wu and Y. C. Shin, "A simplified predictive model for high-fluence ultrashort pulsed laser ablation of semiconductors and dielectrics," *Appl. Surf. Sci.*, vol. 255, no. 9, pp. 4996–5002, Feb. 2009.
- [34] I. Vladoui, M. Stafe, C. Negutu, and I. M. Popescu, "The dependence of the ablation rate of metals on nanosecond laser fluence and wavelength," *J. Optoelectron. adavnced Mater.*, vol. 10, no. 12, pp. 3177–3181.
- [35] S. Bandyopadhyay, J. . Sarin Sundar, G. Sundararajan, and S. . Joshi, "Geometrical features and metallurgical characteristics of Nd:YAG laser drilled holes in thick IN718 and Ti–6Al–4V sheets," *J. Mater. Process. Technol.*, vol. 127, no. 1, pp. 83–95, Sep. 2002.
- [36] Office of Aviation Research, "Engineering Studies of Cleaning and Drying Processes in Preparation for Fluorescent Penetrant Inspection," Washington D.C., 2004.
- [37] H. K. Sezer, L. Li, M. Schmidt, a. J. Pinkerton, B. Anderson, and P. Williams, "Effect of beam angle on HAZ, recast and oxide layer characteristics in laser drilling of TBC nickel superalloys," *Int. J. Mach. Tools Manuf.*, vol. 46, no. 15, pp. 1972–1982, Dec. 2006.

- [38] D. Novovic, R. C. Dewes, D. K. Aspinwall, W. Voice, and P. Bowen, "The effect of machined topography and integrity on fatigue life," *Int. J. Mach. Tools Manuf.*, vol. 44, no. 2–3, pp. 125–134, 2004.
- [39] V. Garat, J. Deleume, J. Cloué, and E. Andrieu, "High Temperature Intergranular Oxidation of Alloy 718," *Superalloys 718, 625, 706 Deriv. 2005*, pp. 559–569, 2005.
- [40] D. T. Pham, S. S. Dimov, P. V Petkov, and S. P. Petkov, "Laser milling," *Proc. Inst. Mech. Eng. Part B J. Eng. Manuf.*, vol. 216, no. 5, pp. 657–667, 2002.
- [41] J. Byskov-Nielsen, "Short-pulse laser ablation of metals : Fundamentals and applications for micro-mechanical interlocking." Department of Physics and Astronomy, University of Aarhus, Denmark, 2010.
- [42] J. Billingham, C. B. Miron, D. A. Axinte, and M. C. Kong, "Mathematical modelling of abrasive waterjet footprints for arbitrarily moving jets: Part II—Overlapped single and multiple straight paths," *Int. J. Mach. Tools Manuf.*, vol. 68, pp. 30–39, 2013.
- [43] B. S. Yilbas, "Parametric study to improve laser hole drilling process," *J. Mater. Process. Technol.*, vol. 70, no. 1–3, pp. 264–273, Oct. 1997.
- [44] M. J. Kim, Z. H. Chen, and P. Majumdar, "Finite element modelling of the laser cutting process," *Comput. Struct.*, vol. 49, no. 2, pp. 231–241, Oct. 1993.
- [45] B. F. Yousef, G. K. Knopf, E. V. Bordatchev, and S. K. Nikumb, "Neural network modeling and analysis of the material removal process during laser machining," *Int. J. Adv. Manuf. Technol.*, vol. 22, no. 1–2, pp. 41–53, Sep. 2003.
- [46] S. Davis, J. Kell, M. C. Kong, D. Axinte, and K. Perkins, "Laser Ablation: Optimising Material Removal Rate with limited Oxidation of TI6A14V," in *30th International Congress on Applications of Lasers and Electro-Optics, ICALEO 2011*, pp. 906–913.
- [47] C. Y. Jiang, W. S. Lau, T. M. Yue, and L. Chiang, "On the Maximum Depth and Profile of Cut in Pulsed Nd: YAG Laser Machining," *CIRP Ann. - Manuf. Technol.*, vol. 42, pp. 223–226, Jan. 1993.
- [48] X. Wang, R. Kang, X. Wenji, and D. Guo, "Direct Laser Fabrication of Aluminum-Alloy Slot Antenna Array," in *2006 1st International Symposium*

- on Systems and Control in Aerospace and Astronautics*, 2006, pp. 1088–1092.
- [49] I. Etsion, "State of the Art in Laser Surface Texturing," *Journal of Tribology*, 2005. .
- [50] H. Kaebernick, D. Bicleanu, and M. Brandt, "Theoretical and Experimental Investigation of Pulsed Laser Cutting," *CIRP Ann. - Manuf. Technol.*, vol. 48, no. 1, pp. 163–166, Jan. 1999.
- [51] W. T. Chien and S. C. Hou, "Investigating the recast layer formed during the laser trepan drilling of Inconel 718 using the Taguchi method," *Int. J. Adv. Manuf. Technol.*, vol. 33, no. 3–4, pp. 308–316, Apr. 2006.
- [52] A. Kar and J. Mazumder, "Two-dimensional model for material damage due to melting and vaporization during laser irradiation," *J. Appl. Phys.*, vol. 68, no. 8, p. 3884, 1990.
- [53] K. Geels, *Metallographic and materialographic specimen preparation, light microscopy, image analysis, and hardness testing*. 2007.
- [54] A. Kumar and N. Singh, "Tribology effect of worn out surface of Aluminium alloy using detonation gun spray coating process," *Int. J. Appl. Sci. Eng. Res.*, vol. 4, no. 1, 2015.
- [55] P. S. To, "Chapter 7 : Basics of X-ray Diffraction," *Solutions*, pp. 1–25, 1999.
- [56] W. H. Bragg and W. L. Bragg, "The Reflection of X-rays by Crystals," *Proc. R. Soc. London. Ser. A*, vol. 88, no. 605, p. 428 LP-438, Jul. 1913.
- [57] Proto Manufacturing, "X-ray Diffraction Residual Stress Measurement: An Introduction." 2011.
- [58] J. Krawczyk, T. Łukaszek-Sołek, A. Śleboda, P. Bała, S. Bednarek, and M. Wojtaszek, "Strain induced recrystallization in hot forged inconel 718 alloy," *Arch. Metall. Mater.*, vol. 57, no. 2, pp. 593–603, 2012.
- [59] A. Hagberg and P. Malm, "Material Deformation Mechanisms during Machining of Superalloys Supervisor :," pp. 1–99, 2010.
- [60] A. C. Vermeulen, "An elastic constant database and XEC calculator for use in XRD residual stress analysis," *Advances in X-ray Analysis*, vol. 44. International Centre for Diffraction Data, pp. 128–133, 2001.

- [61] Y. Ren, C. W. Cheng, J. K. Chen, Y. Zhang, and D. Y. Tzou, "Thermal ablation of metal films by femtosecond laser bursts," *Int. J. Therm. Sci.*, vol. 70, pp. 32–40, 2013.
- [62] B. Wu and Y. C. Shin, "A simple model for high fluence ultra-short pulsed laser metal ablation," *Appl. Surf. Sci.*, vol. 253, no. 8, pp. 4079–4084, Feb. 2007.
- [63] N. Arnold and N. Bityurin, "A fast quantitative modelling of ns laser ablation based on non-stationary averaging technique," *Appl. Surf. Sci.*, vol. 127–129, pp. 184–192, 1998.
- [64] H. Kogelnik and T. Li, "Laser beams and resonators," *Proc. IEEE*, vol. 54, no. 10, pp. 1312–1329, 1966.
- [65] A. E. Siegman, "Lecture: How to ( Maybe ) Measure Laser Beam Quality," no. October. 1997.
- [66] S. W. Lee, H. S. Shin, and C. N. Chu, "Fabrication of micro-pin array with high aspect ratio on stainless steel using nanosecond laser beam machining," *Appl. Surf. Sci.*, vol. 264, pp. 653–663, Jan. 2013.
- [67] N. Krstulović and S. Milošević, "Drilling enhancement by nanosecond–nanosecond collinear dual-pulse laser ablation of titanium in vacuum," *Appl. Surf. Sci.*, vol. 256, no. 13, pp. 4142–4148, Apr. 2010.
- [68] S. Bruneau, J. Hermann, G. Dumitru, M. Sentis, and E. Axente, "Ultra-fast laser ablation applied to deep-drilling of metals," vol. 248, pp. 299–303, 2005.
- [69] D. Gilbert, M. Stoesslein, D. Axinte, P. Butler-Smith, and J. Kell, "A time based method for predicting the workpiece surface micro-topography under pulsed laser ablation," *J. Mater. Process. Technol.*, vol. 214, no. 12, pp. 3077–3088, 2014.
- [70] M. Stoesslein, D. Axinte, and D. Gilbert, "On-The-Fly Laser Machining: A Case Study for In Situ Balancing of Rotative Parts," *J. Manuf. Sci. Eng.*, vol. 139, no. 3, p. 31002, Oct. 2016.
- [71] J. Melorose, R. Perroy, and S. Careas, "Trent XWB 84k HP Compressor Stage Laser Ablation HCF Test Requirements," vol. 1. 2013.
- [72] Q.-T. Li, X.-D. Tong, X.-W. Gao, W. Chen, and L. Cheng, "Estimation method

- of blade high cycle fatigue life based on ultra-high cycle fatigue test of specimen," *Hangkong Dongli Xuebao/Journal Aerosp. Power*, vol. 29, pp. 2471–2475, 2014.
- [73] K. Heinze, S. Schrape, M. Voigt, and K. Vogeler, "Probabilistic endurance level analyses of compressor blades," *CEAS Aeronaut. J.*, vol. 3, no. 1, pp. 55–65, 2012.
- [74] J. O. Peters and R. O. Ritchie, "Foreign-object damage and high-cycle fatigue of Ti-6Al-4V," *Mater. Sci. Eng. A*, vol. 319–321, pp. 597–601, 2001.
- [75] J. J. Ruschau, T. Nicholas, and S. R. Thompson, "Influence of foreign object damage (FOD) on the fatigue life of simulated Ti-6Al-4V airfoils," *Int. J. Impact Eng.*, vol. 25, no. 3, pp. 233–250, 2001.
- [76] M. Nadaf and S. Shegedar, "Idealization of a Foreign Object Damaged Compressor Blade of an Aero Engine to Rectangular Plate to determine the Stress Concentration Factor using FEM," *Int. J. Eng. Sci. Invent.*, vol. 2, no. 5, pp. 61–68, 2013.
- [77] F. R. Caliari, N. M. Guimarães, D. A. P. Reis, A. A. Couto, C. Moura Neto, and K. C. G. Candioto, "Study of the Secondary Phases in Inconel 718 Aged Superalloy Using Thermodynamics Modeling," *Key Eng. Mater.*, vol. 553, pp. 23–28, 2013.
- [78] P. M. Mignanelli *et al.*, "Gamma-gamma prime-gamma double prime dual-superlattice superalloys," *Scr. Mater.*, vol. 136, pp. 136–140, 2017.
- [79] Y. Zhang, Z. Li, P. Nie, and Y. Wu, "Effect of cooling rate on the microstructure of laser-remelted INCONEL 718 coating," *Metall. Mater. Trans. A Phys. Metall. Mater. Sci.*, vol. 44, no. 12, pp. 5513–5521, 2013.
- [80] Special Metals, "INCONEL ® Alloy 718." 2007.
- [81] R. López and R. Villagómez, "Beam profile analyzer for CO2 lasers," *J. Appl. Res. Technol.*, vol. 13, no. 6, pp. 586–590, 2015.
- [82] Industrial Photonics, "Shorter Wavelengths, Pulses Power Laser Manufacturing," vol. 1, no. 4, pp. 1–32, 2014.